学位論文

Vortex-Split Stratospheric Sudden Warmings: An Understanding Based on Equilibrium Statistical Mechanics

(スプリット型成層圏突然昇温：平衡統計力学に基づく理解)

平成 28 年 12 月博士 (理学) 申請

東京大学大学院理学系研究科
地球惑星科学専攻

安　田　勇　輝

Contents

要旨

北半球冬季の成層圏 (高度 10 – 50 km) には、極渦と呼ばれる世界最大の孤立渦の 1 つが存在する (e.g., Waugh and Polvani 2013)。極渦は対流圏起源の Rossby 波により乱されており、この乱れが大きくなると温度上昇と共に崩壊する。この現象は成層圏突然昇温 (SSW) と呼ばれ、対流圏の気象システムにも影響を及ぼすことが知られている (e.g., Kidston et al. 2015)。SSW は、極渦が南にずれて崩壊するディスプレイスメント型 (D-SSW) と、極渦が 2 つに分離して崩壊するスプリット型 (S-SSW) に分類される (Charlton and Polvan 2007)。

SSW のメカニズムは、Matsuno (1971) を始めとし、ダイナミクスの観点から弱非線形理論を用いて研究されてきた。S-SSW に限って言えば、東西波数 2 の等価順圧 Rossby 波が共鳴により増幅し、その後、Love 型の力学的不安定 (Love 1893) により極渦が 2 つに分離すると考えられている (Esler and Scott 2005; Mitchell and Rossi 2008; Matthewman and Esler 2011)。これらの弱非線形理論は微小振幅擾乱の仮定に基づいているが、SSW のような強非線形現象に対して、この仮定は必ずしもよくは満たされていない可能性がある。

強非線形理論の 1 つとして平衡統計力学が挙げられる。地球流体系における統計力学はここ 20 年で大きく発展し (e.g., Bouchet and Venaille 2012)、特に、ミクロカノニカル分布と呼ばれる確率モデルから最大エントロピー問題が数学的に導出された (Michel and Robert 1994; Boucher et al. 2000; Ellis et al. 2000)。統計力学は微小振幅擾乱の仮定に基づかないため、強非線形系に適用可能である。その反面、スタティックな理論であり、系の

時間発展に関する情報を全く与えないという欠点もある。すなわち、上記の弱非線形理論と正反対の長所と短所を持つ。本研究では、気象庁 55 年長期再解析 (JRA-55)、球面準地衡 (QG) 順圧モデル、および統計力学を用いて、エントロピーの観点から S-SSW の理解を試みた。

本研究では、S-SSW を QG 順圧モデルに基づいて調べる。最初にこのことの合理性を示すために、Seviour et al. (2013) に従い、JRA-55 から S-SSW の平均像をコンポジット解析により求めた。そして、Matthewman et al. (2009) と同様の解析により、極渦の分離前後の高度 20 – 40 km において、極渦が等価順圧構造を持つことを確認した。そこで、以下では、極渦の時間変化を一層の球面 QG 順圧モデルで記述することにした。

まず、順圧モデルの有効性を確認するために、コンポジット解析で得られた S-SSW の渦位 (PV) の時間発展が順圧モデルにより再現可能であるか調べた。この比較実験を行うために、順圧モデルの下部強制 h は、JRA-55 のコンポジット 550 K 温位面 (高度約 20 km に存在) の高度偏差とした。そして、初期条件は、ある基準時刻の JRA-55 のコンポジット PV とし、その後の PV の時間発展を数値積分により求めた。比較対象であるコンポジット PV は、JRA-55 の絶対渦度の鉛直平均から求めた。積分開始から約 15 日目までは、順圧モデルは JRA-55 の PV 場をよく再現することが分かった。15 日目以降は、コンポジット場の傾圧性が強くなり、順圧モデルによる PV 場の再現性が悪くなる。

次に、初期条件は変化させず、強制 h の東西波数 0, 1, 2 成分のいずれかのみを抽出し、それを強制とした実験を行った。その結果、h の波数 2 成分を使用した場合のみ、極渦の分離が再現された。これは、強制 h の波数 2 成分が S-SSW にとって最も本質的であることを示唆している。従って、以下では、波数 2 の強制のみを考慮した。

コンポジット PV 場との比較実験では、強制 h の時間変化が速いため、極渦の状態遷移はあまり明瞭ではなかった。そこで h の振幅をゆっくり増大させる準静的 (quasi-static) 実験を行い、状態遷移を調べることにした。初期条件は JRA-55 の絶対渦度の時間・鉛直

平均場とした。強制 h の波数 2 の構造は固定し、その振幅 a を 2.8 万日かけて $a = 0$ から 1 に線形に増大させた。その結果、a の増大と共に、3 つの状態 A, B, C がこの順に現れた。各状態は定常と見なせ、状態の遷移時にのみ、PV 場は非定常となった。A と B は低気圧性、C は高気圧性の流れ場である。B から C の遷移時には、細長く伸びた極渦から PV フィラメントが剥離し、極渦は 2 つに分離することなく崩壊した。

この準静的実験の結果を、統計力学理論の一つである二次の Casimir 変分問題 [Quadratic Casimir Variational Problem, QCVP (e.g., Venaille and Bouchet 2009, 2011b)] で解釈する。QCVP において、エントロピー S はポテンシャルエンストロフィーのマイナス倍で与えられる。そして、エネルギー E と PV の総量 Γ を一定とする拘束条件の下で、エントロピー S は最大化される。この S 最大の状態は平衡状態と呼ばれ、微小擾乱に対し安定な定常場である (e.g., Ellis et al. 2002)。この解は E と Γ だけでなく、PV の定義式を通して強制 h の振幅 a に依存する。準静的実験のパラメータ (E, Γ, a) の全範囲において、平衡状態は高気圧性の流れ場であった。そのため、状態 C は平衡状態と解釈できる。

次に、A と B に対応する低気圧性の状態を議論するために、エントロピーの鞍点である準定常状態 (QSS) を調べた。QSS は定常場であるが、微小擾乱に対し安定とは限らない。QSS は無数に存在するが、最も大規模な構造を持つ QSS 1 に着目する。この状態は回転対称性を持たない領域内 (e.g., 正方形領域) で、エントロピーの極大点 (すなわち、微小擾乱に対し安定な状態) となり得る唯一の状態である。一方、回転対称な円盤領域内では、東西波数 1 の基底モードに対してのみ QSS 1 は不安定になり得る。この QSS 1 は低気圧性で、その PV 場は状態 A と同様の空間構造を持つ。よって、状態 A は QSS 1 と解釈できる。次に、3 番目に大きな構造を持つ QSS 3 に着目した。QSS 3 の PV 場は、QSS 1 (また QSS 2) の PV 場と直交する方向に伸びており、状態 B の空間構造に類似している。よって、状態 B は QSS 3 と解釈できる。

より定量的な比較を行うため、遷移の瞬間が理論予測と整合的であるかも調べた。こ

こでは極渦の崩壊を伴う B から C の遷移に着目する。準静的実験の各時刻において、Γ と a を与えて、状態 B に対応する QSS 3 の存在に必要な最小エネルギー E を理論的に求めた。そして、その最小 E と準静的実験の E の時系列を比較した。結果、1.8 万日目付近で、理論による最小 E よりも実験の E が小さくなった。これは、QSS 3 が存在できないパラメータ領域へ状態が移行することを意味し、その周辺の時刻において遷移が起こる可能性を示唆する。実際に、ほぼ同じ時刻において、エントロピーの急増と共に極渦は崩壊し、B から C への遷移が起こる。すなわち、PV 場の構造という定性的な点だけでなく、遷移のタイミングという定量的な点からも、状態 B を QSS 3 と解釈する妥当性が示された。同様の結果は、A から B の遷移に対しても得られ、初期状態 A を QSS 1 と解釈する妥当性が確認された。

次に、実験設定をより現実的にするため、強制 h の振幅 a を 1 週間で増加させた。その結果、状態は A から C へ遷移し、その過程で極渦の分離が起こった。これは、S-SSW を低気圧性の QSS 1 から高気圧性の平衡状態へ向かおうとする遷移と理解できる可能性を示唆する。

平衡状態は任意の微小擾乱に対して力学的に安定であるが、QSS 1 は東西波数 1 の微小擾乱に対してのみ不安定となる可能性がある。そこで QSS 1 の安定性を調べるため、QSS 1 と見なされる準静的実験の流れ場に波数 1 の微小擾乱を加えて、その後の時間発展を球面 QG 順圧モデルの数値積分により調べた。結果、波数 1 の擾乱は急激に減衰後、小振幅を保ったまま振動した。この結果は、波数 1 の擾乱が成長しないこと、すなわち QSS 1 が Lyapnov 安定 (中立安定または漸近安定) であることを示唆する。

冬季成層圏において、放射冷却は約 10 日の緩和時間をもち (Newman and Rosenfield 1997)、S-SSW 後の極渦の再形成に寄与する (e.g., Scott and Polvani 2006)。そこで、さらに現実的な実験を行うため、Newton 冷却を模した線形緩和を順圧モデルに組み込んだ。その結果、極渦の分離は見られたが、高気圧性の平衡状態は確認できなかった。これは、

平衡状態への遷移時間が約 200 日と十分長く、線形緩和による極渦の回復が先に起こるためと考えられる。

一方、東西平均東西風は、S-SSW の期間内に、西風から東風へ一時的に変化することがある。この軸対称成分の低気圧から高気圧性への一時的な変化は、コンポジット S-SSW と線形緩和を入れた数値実験の両方で確認できた。これらの結果は、成層圏の状態が高気圧性の平衡状態へ一時的に近づくことを示唆する。

以上の結果から「S-SSW がエントロピーの鞍点 (QSS 1) から最大点 (平衡状態) へ向かおうとする遷移」と理解できることが分かった。QSS 1 は低気圧性の流れ場で、極渦の崩壊前に対応する。また QSS 1 はエントロピーの極大点になり得る唯一の特別な鞍点である。平衡状態は高気圧性の流れ場で、極渦の崩壊後に対応する。遷移を起こす主要因は Rossby 波の増幅であり、遷移途中で極渦は分離する。放射冷却による極渦の回復のため、平衡状態は実現されないと考えられるが、成層圏の状態は一時的に平衡状態へ向かおうとする。東西平均東西風の逆転は、平衡状態に向かおうとする途中状態を反映していると考えられる。

Abstract

Vortex-split stratospheric sudden warming (S-SSW) is an extreme event in the stratosphere, in which the polar vortex breaks down while splitting into the two daughter vortices. The dynamical mechanism for S-SSWs has been understood by employing weakly nonlinear theories that are based on the assumption of small-amplitude perturbations (e.g., Matsuno 1971; Chao 1985; Matthewman and Esler 2011). This assumption may be not necessarily satisfied well for strongly nonlinear phenomena such as S-SSWs. Equilibrium statistical mechanics is a strongly nonlinear theory and has made great progress over the last two decades (e.g., Bouchet and Venaille 2012). It is possible to obtain a large-scale coherent structure realized after strong PV (potential vorticity) mixing, by solving a variational problem (e.g., maximum entropy problem) without solving the governing equations of a system. The present study investigates S-SSWs by using a reanalysis dataset, a quasi-geostrophic (QG) barotropic model, and a statistical-mechanics theory.

Composite analyses of S-SSWs are made by using the Japanese 55-year Reanalysis (JRA-55). The equivalent-barotropic nature of the S-SSW is confirmed in the altitude range of about 20 to 40 km, as found by Matthewman et al. (2009). On the basis of these composite analyses, a spherical QG barotropic model is constructed to describe the equivalent-barotropic motions associated with S-SSWs. The effective bottom forcing in the QG model is given by the composite height field of the 550-K isentropic surface ($\sim$ 20 km). The QG model well reproduces the evolution of the composite PV made from JRA-55 during the period before a baroclinic structure

develops in the composite S-SSW. The zonal-wavenumber-2 component of the bottom forcing is essential to reproduce the vortex splitting in the QG model.

To reveal a transition of the polar vortex in the QG model, a quasi-static experiment is conducted, where the amplitude of the wavenumber-2 bottom forcing is increased linearly and sufficiently slowly with time. The flow field over the North Pole is nearly steady, which facilitates pursuing the state changes of the polar vortex. Two transitions are observed: in the first transition, the shape of the polar vortex changes; in the second transition, the polar vortex breaks down without splitting, while the flow over the North Pole changes from cyclonic to anti-cyclonic.

The theory of statistical mechanics named the quadratic Casimir variational problem (QCVP, e.g., Venaille and Bouchet 2009, 2011b) is applied to the polar cap over 45 to 90°N. In the QCVP, the entropy, which is the negative of potential enstrophy, is maximized with the constraints of constant total PV and energy. The equilibrium state is anti-cyclonic, whereas the quasi-stationary states are cyclonic, in the parameter range relevant to the winter stratosphere. A quasi-stationary state is defined as a saddle point of the entropy, and an equilibrium state as the entropy maximum. The quasi-stationary state having the largest structure (QSS 1) can be a local maximum of the entropy (i.e., metastable) in a general domain not having the rotational symmetry. This unique property of QSS 1 comes from the fact that QSS 1 becomes an equilibrium state, as the total PV is increased. By contrast, in the disk domain, QSS 1 may be destabilized by a perturbation with zonal wavenumber 1, but it is dynamically stable against any small-amplitude perturbations with the other wavenumbers.

The results of the quasi-static experiment are interpreted with the QCVP. The theory well explains the structures of the PV fields observed in the quasi-static experiment. Moreover, the timings of the two transitions in the quasi-static experiment are consistent with those given by

the QCVP. The initial state in the quasi-static experiment is regarded as QSS 1, and the final state as the equilibrium state. To examine the dynamical stability of QSS 1, the evolution of the wavenumber-1 perturbations are examined by adding these perturbations to the flow field regarded as QSS 1 and performing the numerical integrations. In all cases, the small- but finite-amplitude perturbations do not grow with time, which implies that QSS 1 is Lyapunov stable. By contrast with the quasi-static experiment, when the forcing amplitude is increased over one week (not sufficient slow), the polar vortex splits during the transition from the cyclonic QSS 1 to the anti-cyclonic equilibrium state.

Effects of radiative cooling are discussed by performing QG experiments including a linear relaxation, where the relaxation time is O(10 days). The polar vortex is re-formed by the linear relaxation before the anti-cyclonic equilibrium state is organized, which is likely due to that the transition time (about 200 days) is one-order larger than the relaxation time.

The above results suggest a new understanding of S-SSWs based on the equilibrium statistical mechanics: The S-SSW can be qualitatively understood as the transition from the cyclonic QSS 1 in the direction of the anti-cyclonic equilibrium state. The transient state with the splitted two vortices is a non-equilibrium state that appears during the transition in the direction of the equilibrium. Without radiative cooling, the anti-cyclonic equilibrium state would be realized at a later time ($\sim$ 200 days) after an S-SSW. In the stratosphere, however, the radiative cooling [relaxation time = O(10 days)] will re-establish a cyclonic polar vortex, before the anti-cyclonic equilibrium state is organized. During an S-SSW, zonal-mean zonal winds often change from westerly to easterly, which suggests that the state of the stratosphere temporarily approaches the anti-cyclonic equilibrium state.

Chapter 1

General Introduction

1.1 Stratospheric sudden warmings (SSWs)

The polar vortices in the winter stratosphere are the largest coherent vortices in the atmosphere (e.g., Andrews et al. 1987; Haynes 2005; Waugh and Polvani 2013). The polar vortices are cyclonic flows maintained, through the thermal wind relation, by the radiative cooling over the winter poles. The Arctic polar vortex (hereafter, simply referred to as the polar vortex) is perturbed by planetary-scale Rossby waves generated by topography and land-sea contrast in the troposphere. Sufficiently strong wave forcings sometimes break down the polar vortex. Such an extreme event has a time scale of a few days and is accompanied by a reversal of zonal winds (from westerly to easterly) and a strong warming (sometimes over 50 K) in the polar stratosphere, called a major stratospheric sudden warming (SSW, see Fig. 1.1). SSWs occur on average about once every two winters in the Northern Hemisphere.

The SSW is not only an interesting phenomenon confined to the stratosphere, but is also practically important for our daily lives because it affects tropospheric eddies, i.e., weather systems (e.g., Baldwin and Dunkerton 2001; Nakagawa and Yamazaki 2006; Mitchell et al. 2013; Kidston et al. 2015). For instance, the storm tracks tend to be displaced southward after an SSW (Baldwin and Dunkerton 2001). Because of the downward influence from the stratosphere, several studies have indicated that the weather predictions are improved by the

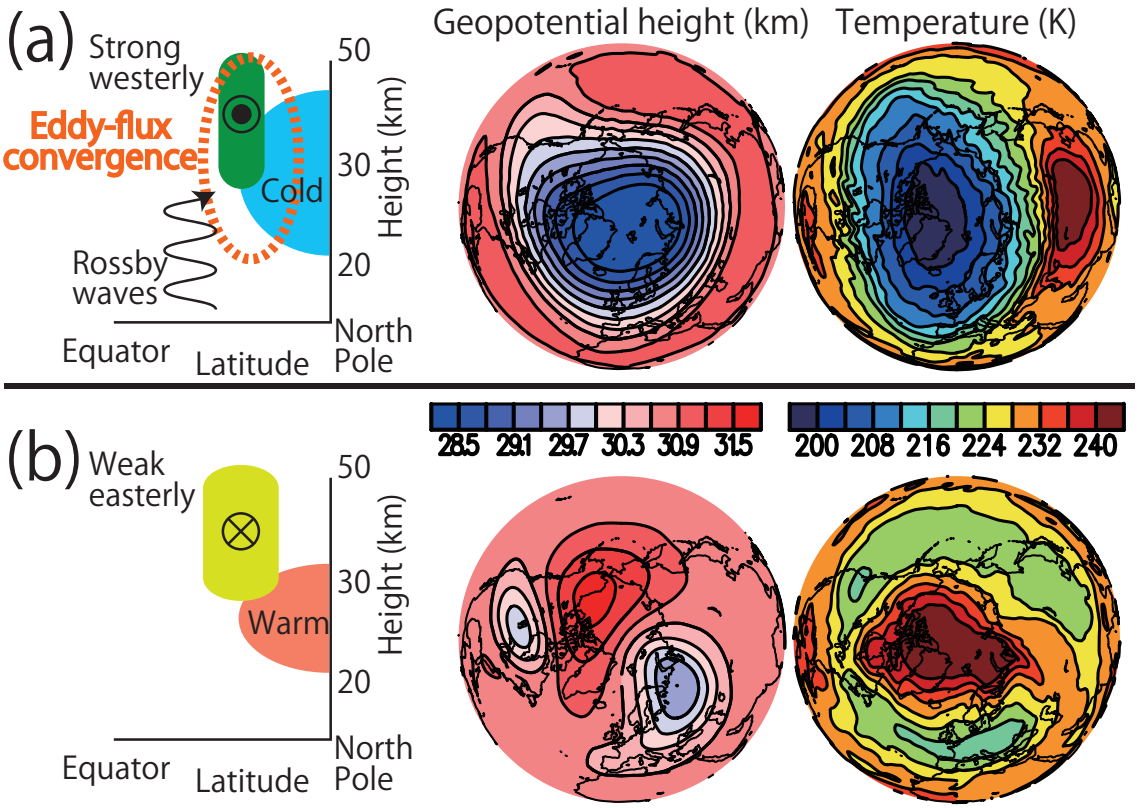

Figure 1.1: Left panels show schematic illustrations in the latitude-height sections for the states (a) before and (b) just after an SSW. Middle and right panels show examples of snapshots on the 10-hPa isobaric surface (about 30-km height) during the February 1979 S-SSW in JRA-55 [(a) on Dec. 31, 1978 and (b) on Feb. 28, 1979], corresponding to the left panels: (middle) geopotential height and (right) temperature.

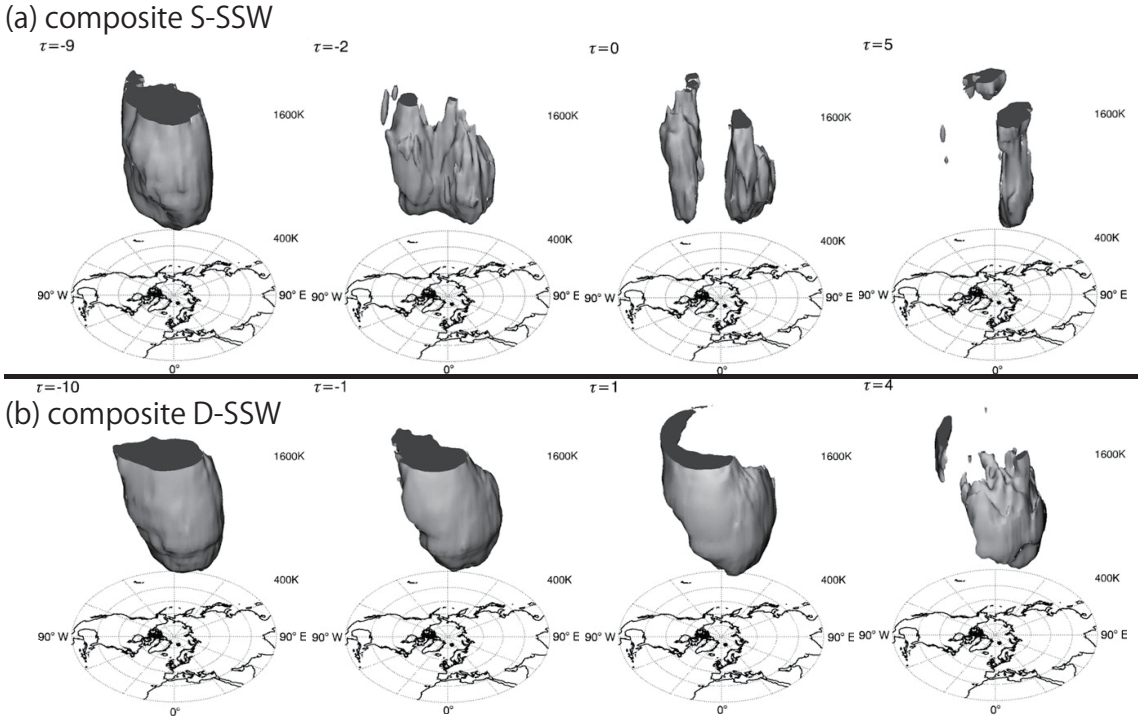

Figure 1.2: Three-dimensional isosurfaces of the composite vertically weighted Ertel's potential vorticity (PV) for (a) S-SSW and (b) D-SSW between the isentropic surfaces of 400 and 1600 K (about the 14- and 44-km heights), made from the ERA-40 dataset. τ denotes time in days. These isosurfaces accord well with the polar-vortex boundary defined by the maximum of PV gradient. Adapted from Matthewman et al. (2009) with permission of ©American Meteorological Society.

proper representation of stratospheric processes, including SSWs (e.g., Mukougawa and Hirooka 2004; Tripathi et al. 2015).

SSWs are classified into vortex-displacement type (D-SSWs) and vortex-split type (S-SSWs) on the basis of the horizontal structure of the polar vortex (Charlton and Polvani 2007). During a D-SSW event, the polar vortex is displaced equatorward and broken down, whereas during an S-SSW, the polar vortex collapses while splitting into the two daughter vortices. By contrast with the D-SSW, the S-SSW has a nearly equivalent-barotropic structure (Fig. 1.2); in particular, the vortex splitting occurs almost simultaneously over the altitude range of about 20 to 40 km (Matthewman et al. 2009). Note that the term SSWs is hereafter used to denote SSWs without distinguishing between S-SSWs and D-SSWs.

1.2 Mechanism for SSWs

1.2.1 Matsuno's model

A pioneering work on the mechanism for SSWs was made by Matsuno (1971). He proposed that SSWs result from the amplification of wave forcing (i.e., the convergence of eddy fluxes) to the mean flows (Fig. 1.1). He devised a theoretical model from a continuously stratified quasi-geostrophic (QG) system. His model describes the interactions between the zonal mean flow and one wave mode generated by an effective bottom forcing at the tropopause height (= 10 km) that mimics some large-scale disturbance propagating from the troposphere. The numerical integrations of his model successfully reproduced events similar to SSWs in the atmosphere.

Following Matsuno (1971), SSWs have often been theoretically studied in the framework of wave-mean flow interaction. These studies may be roughly categorized into two groups: The first group employs a severely truncated dynamical system called the Holton-Mass model (Holton and Mass 1976); The second group focuses on the resonance of Rossby waves and is here referred to as the resonance theory (e.g., Tung and Lindzen 1979a,b). Both groups of studies rely on weakly nonlinear theories using perturbation expansions in terms of a small parameter representing a normalized wave amplitude.

1.2.2 Holton-Mass model

The Holton-Mass model is obtained by simplifying Matsuno's model (Holton and Mass 1976). The crucial procedure to derive the model is that the meridional structure of all the fields is approximated by a single sine function. This simplification reduces the degrees of freedom of the model and makes it possible to investigate the solutions of the model by using the bifurcation theory. Another important difference from Matsuno's model is that the Holton-

Mass model includes Newtonian cooling. As the bottom forcing is increased, the model shows an abrupt transition from a quasi-steady state with a strong westerly wind (close to the radiative equilibrium) to a time-dependent state where the zonal wind vacillates between weak westerly and easterly (Holton and Mass 1976).

Chao (1985) investigated the Holton-Mass model in terms of the catastrophe theory (a branch of bifurcation theory), and argued that an SSW in the atmosphere corresponds to a catastrophe, which is characterized by the abrupt transition in the model. Similar transitions have been observed in a one-layer version of the Holton-Mass model (Ruzmaikin et al. 2003; Birner and Williams 2008) and also in an improved Holton-Mass model where the bottom forcing is specified through the Eliassen-Palm flux (Sjoberg and Birner 2014).

1.2.3 Resonance theories

It may be naturally understood that an amplification of a Rossby-wave source (i.e., a bottom forcing) leads to an SSW through the increase in eddy-flux convergence. There is another mechanism for a wave amplification, which is resonance. The theories that attempt to interpret SSWs in terms of resonance may be classified into linear and nonlinear theories.

Tung and Lindzen (1979a,b) derived a linear theory based on a continuously stratified QG model, and revealed that stationary Rossby waves can be resonant with a bottom topography in a realistic zonal-mean velocity field. Using a linear response theory, Esler and Scott (2005) analyzed the results of fully nonlinear, three-dimensional QG simulations imitating an S-SSW. They argued that the resonance of an equivalent-barotropic Rossby-wave mode is essential to the onset of S-SSWs. Thus, not only an increase in an effective bottom forcing but also a resonance can lead to the Rossby-wave amplification that results in an SSW.

When a resonance occurs, the wave amplitude becomes large and nonlinear effects can no longer be ignored. Plumb (1981a,b) obtained a weakly nonlinear system from a continuously

stratified QG model, and demonstrated that the nonlinear effect makes a positive feedback, that is, the nonlinear adjustment to the mean velocity occurs in a way to amplify the wave. Matthewman and Esler (2011) extended Plumb's idea and investigated the onset of S-SSWs by using a weakly nonlinear model. This model describes the evolution of a barotropic vortex-Rossby wave generated by a wavenumber-2 bottom forcing. They showed that an abrupt transition to the larger amplitude solution occurs in the model when the forcing is stronger than a threshold, which corresponds to the evolution of a Rossby wave in the onset period of S-SSWs. Esler and Matthewman (2011) also investigated D-SSWs by applying similar techniques to a stratified fluid model, and argued that the nonlinear resonance of the first baroclinic Rossby-wave mode is important to the onset of D-SSWs.

1.3 Equilibrium statistical mechanics for geophysical flows

An inviscid, freely-evolving, two-dimensional flow tends to develop into finer and finer structures, while at a later time it tends to reach a quasi-steady, large-scale coherent structure. Such a complex system generally shows a high sensitivity to the initial conditions and ends in a chaotic state. It may not be easy to obtain such a large-scale structure that appears after a long-time evolution by solving governing equations. Equilibrium statistical mechanics gives a general method to obtain a large-scale coherent structure realized after strong PV (potential vorticity) mixing, without solving the governing equations (e.g., Salmon 1998; Majda and Wang 2006; Bouchet and Venaille 2012). More precisely, the statistical mechanics gives a variational problem (e.g., a problem of maximum entropy) with some constraints on parameters such as total energy and bottom forcing. A large-scale steady flow is obtained as a solution of the variational problem, which is called an equilibrium state. By studying the equilibrium states over some parameter range, it is possible to understand the effects of varying parameters

such as total energy and bottom forcing.

One of the most important mathematical results in the statistical mechanics is that an overwhelming number of possible states are associated with the equilibrium state (Michel and Robert 1994; Boucher et al. 2000; Ellis et al. 2000). This means that if one state were picked up at random among all the possible states, including unsteady turbulent states, and if a spatial coarse-graining were performed, the equilibrium state would be recovered. In other words, the equilibrium state is overwhelmingly common and occupies a quite large portion of the phase space.

The statistical mechanics usually does not rely on perturbation expansions (or the assumption of small-amplitude perturbations); hence, it can be used for a strongly nonlinear system. On the other hand, the statistical mechanics is applicable only to a freely evolving flow without diabatic heating nor dissipation, and does not give any information on the time evolution of a system (e.g., even the equilibrium states are not necessarily attractive fixed points). Thus, the statistical mechanics has the opposite weakness and strength to those of the weakly nonlinear theories described above.

1.3.1 Casimir variational problems

The general theory of equilibrium statistical mechanics for geophysical flows is known as the Miller-Robert-Sommeria (MRS) theory (Miller 1990; Robert 1991; Robert and Sommeria 1991). The MRS theory gives the most general variational problem that takes into account all conserved quantities: total energy and any moment of PV. Due to this generality, however, the entropy maximization of the MRS theory is quite complicated and is not easy to solve. This complexity originates from the constrains reflecting all conserved quantities.

Several variational problems have been proposed, where the complicated constraints are relaxed (e.g., Bouchet 2008; Bouchet and Venaille 2012). One important subclass of the MRS

theory is the Casimir variational problem (CVP):

$$\max_{q} \left\{ C \equiv \int s(q)\, \mathrm{d}A \;\middle|\; E, \Gamma \right\}, \tag{1.1}$$

where

$$E = \frac{1}{2} \int (\boldsymbol{\nabla}\psi)^2 \, \mathrm{d}A, \quad \text{and} \quad \Gamma = \int q \, \mathrm{d}A. \tag{1.2}$$

The formula (1.1) means that C is maximized by varying q subject to the two constraints of constant E and Γ. Here, q is a PV in a two-dimensional system, ψ is the stream function given by the PV inversion, $\mathrm{d}A$ is an area element, Γ is the total PV, E is the total energy, and s is an arbitrary concave function of q. Solving the CVP (1.1) is not quite difficult because only the two constraints are imposed. More importantly, any solution of the CVP is a solution of the MRS theory, but the converse is not necessarily true (Bouchet 2008). In other words, any equilibrium state in the CVP belongs to the MRS equilibria (Fig. 1.3).

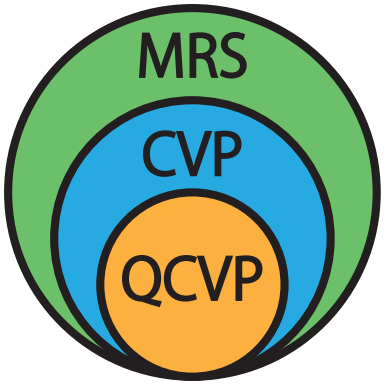

Figure 1.3: Relation between the MRS, CVP, and QCVP equilibria.

In the CVP (1.1), $s(q)$ is an arbitrary concave function. One of the simplest concave functions is a quadratic one: $s \equiv -1/2 \times q^2$. The CVP using this function is referred to as the quadratic Casimir variational problem (QCVP, Chavanis and Sommeria 1996; Venaille and Bouchet 2009, 2011b; Naso et al. 2010):

$$\max_{q} \left\{ S \equiv -\frac{1}{2} \int q^2 \, \mathrm{d}A \;\middle|\; E, \Gamma \right\}. \tag{1.3}$$

Although S is the negative of potential enstrophy, it is called the entropy because the state maximizing S is always that of maximum mixing (or Shannon) entropy (Bouchet 2008). The exponential of mixing entropy gives the number of possible (micro) states. This implies that the state maximizing S, i.e., the equilibrium state of the QCVP, is overwhelmingly common, as stated above.

The QCVP has been studied independently in geophysical fluid dynamics, and it is called the selective decay (or minimum enstrophy) principal (Bretherton and Haidvogel 1976; Carnevale and Frederiksen 1987). In the context of the selective decay principal, the constraint of the total PV (Γ) is often excluded. This principal was first proposed from a phenomenological viewpoint, associated with the inverse cascade in two-dimensional fluids. Later, its validity has been rigorously proven for some viscous fluid systems (Foias and Saut 1984; Majda et al. 2000; Majda and Wang 2006): A two-dimensional fluid evolves asymptotically into the equilibrium state, under the presence of Newtonian or hyper viscosity.

1.3.2 Applications to geophysical fluid systems

The equilibrium statistical mechanics has already been applied to several geophysical fluid problems: Jupiter's great red spots (Bouchet and Sommeria 2002), bottom trapped flows over oceanic bottom topographies (e.g., Merryfield 1998; Venaille 2012), mesoscale eddies and jets in the ocean (Venaille and Bouchet 2011a), an idealized jet in a two-layer QG model (Esler 2008), and hurricanes (Prieto et al. 2001).

Prieto and Schubert (2001) examined the evolution of the polar vortex that was dynamically unstable at the initial time (i.e., the meridional PV gradient was negative somewhere) by using a spherical, unforced, barotropic model without bottom forcing. They applied the MRS theory and QCVP, and demonstrated that both successfully predicted the final states simulated by the numerical model.

1.4 Overview of this thesis

The present study proposes a new understanding of S-SSWs based on the equilibrium statistical mechanics (Fig. 1.4): The S-SSW can be qualitatively understood as a transition from an entropy saddle point in the direction of the entropy maximum (i.e., the equilibrium state).

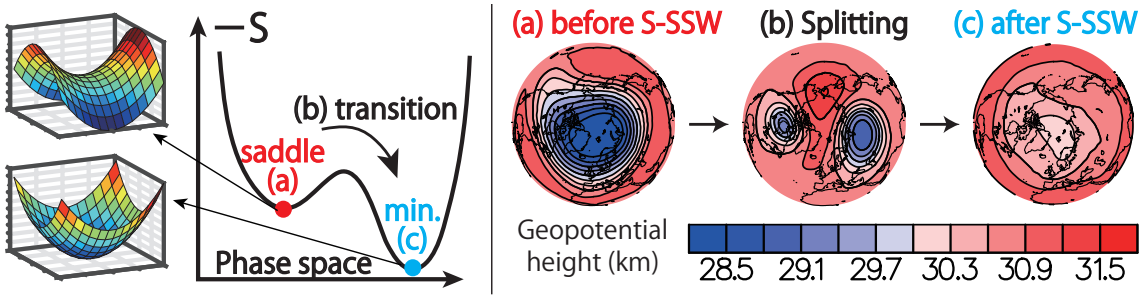

Figure 1.4: (left) Schematic illustration of the new understanding on S-SSWs. Note that the entropy (S) maximum is the minimum of $-S$. (right) Snapshots of geopotential height at the 10-hPa isobaric surface during the February 1979 S-SSW in JRA-55, corresponding to the states in the left figure: (a) on Dec. 31,1978; (b) on Feb. 22, 1979; and (c) on Mar. 31, 1979.

The polar vortex splits during this transition.

The thesis is organized as follows. In Chapter 2, a composite S-SSW is made from the Japanese 55-year Reanalysis (JRA-55), and we demonstrate a nearly equivalent-barotropic structure of the composite S-SSW. In Chapter 3, a spherical QG barotropic model is constructed on the basis of the composite analysis. The validity of the QG model is verified through the direct comparison with the evolution of the composite PV. In addition, to examine a transition of the polar vortex, a quasi-static experiment is performed, in which the amplitude of a wavenumber-2 bottom forcing is increased linearly and sufficiently slowly with time. In Chapter 4, the statistical-mechanics theory, namely the QCVP, is applied to a two-dimensional disk domain with the wavenumber-2 bottom forcing. In Chapter 5, the results of the quasi-static experiment are interpreted with the QCVP, and the new understanding of S-SSWs is proposed. In Chapter 6, effects of radiative cooling are discussed, and a view of potential is proposed. Associated with this view, we discuss the preconditioning of the polar vortex and the SSWs in the Southern Hemisphere. Finally, the conclusions are given in Chapter 7.

Chapter 2

Composite Analysis of Vortex-Split SSWs (S-SSWs)

The S-SSW is known to have a nearly equivalent-barotropic structure between the altitudes of about 20 and 40 km around the vortex splitting (Matthewman et al. 2009). Due to this equivalent-barotropic structure, the S-SSW is considered to be caused mainly by the amplification of an equivalent-barotropic Rossby wave (Esler and Scott 2005; Matthewman and Esler 2011). In this chapter, we confirm these results by analyzing a reanalysis dataset (JRA-55). In Section 2.1, a composite S-SSW is constructed from JRA-55. In Section 2.2, we analyze the three-dimensional PV structure and confirm that the composite S-SSW has the nearly equivalent-barotropic structure. Finally, in Section 2.3, we show that disturbances with a vertical scale of about 85 km are predominant when the polar vortex splits.

2.1 Construction of composite fields

We analyze the Japanese 55-year Reanalysis (JRA-55, Kobayashi et al. 2015) and construct a composite S-SSW from 10 S-SSW events showing distinct splittings of the polar vortex. Following Seviour et al. (2013), all S-SSWs are identified by applying the vortex-moment diagnostics to geopotential height at 10 hPa (about 30-km height) over the winters (December to March) of 1958/1959 to 2013/2014. In the vortex-moment diagnostics, the polar vortex

is approximated to be an ellipse of uniform geopotential height that is defined from the first and second moments of the geopotential-height field (see Appendix A for details). An S-SSW requires the aspect ratio of the ellipse to remain larger than 2.3 for 7 consecutive days or more. The onset time is defined as the time when the threshold of 2.3 is first exceeded, and is designated by $t = 0$ (i.e., the reference of time).

To prevent from counting the same S-SSW twice, once an S-SSW is identified, no event is defined within 30 days of the onset time. This interval is approximately equal to three radiative time scales at 10 hPa (Newman and Rosenfield 1997).

Moreover, to extract S-SSWs associated with vortex splittings near the North Pole, we exclude events in which the ellipse centroid moves to the south of 66°N once or more between $t = 0$ and 7 days. This procedure corresponds to excluding mixed S-SSWs, which have features common to S-SSWs and D-SSWs (Mitchell et al. 2013), because a D-SSW is defined as an event where the ellipse centroid remains equatorward of 66°N for 7 consecutive days or more (Seviour et al. 2013). After this procedure, 18 S-SSWs are identified. About a half of these S-SSWs do not show distinct vortex splittings and are excluded accordingly.

To make a meaningful composite, an average needs to be taken over S-SSWs having similar characteristics. To this end, we further extract 10 S-SSWs in which the distance between the two ellipse centroids of the daughter vortices, after the vortex splitting, is at least 2000 km larger than the sum of the lengths of their major axes for more than 4 consecutive days. The following results are insensitive to the choice of the criterion values of 2000 km and 4 days. In fact, the same results were obtained when 1500 km and 3 days were used instead. Table 2.1 shows the onset dates of the 10 S-SSWs obtained in the present study and those in Seviour et al. (2013). For the 10 S-SSWs identified here, the zonal-mean zonal wind at 10 hPa returns to westerly for 10 consecutive days or more before April 30, which indicates that these events

Table 2.1: Onset dates of the S-SSWs showing the distinct splittings of the polar vortex. For comparison, the corresponding onset dates in Seviour et al. (2013) are listed. The symbol × denotes that the 2012/13 winter is outside their analysis period.

This study	Seviour et al. (2013)
Jan. 03, 1968	Dec. 29, 1967
Jan. 16, 1971	Jan. 15, 1971
Feb. 04, 1973	Feb. 04, 1973
Feb. 17, 1979	Feb. 18, 1979
Dec. 25, 1984	Dec. 25, 1984
Feb. 24, 1999	Feb. 24, 1999
Mar. 15, 2001	Mar. 15, 2001
Mar. 21, 2002	Mar. 21, 2002
Jan. 18, 2009	Jan. 18, 2009
Jan. 05, 2013	×

are not final warmings (Charlton and Polvani 2007).

Finally, as in Seviour et al. (2013), each composite field is constructed by simply averaging over the 10 S-SSWs at each time t. The direction of the vortex splitting is slightly different among the 10 S-SSWs, which suggests that a composite field may be distorted due to the cancellation among the 10 S-SSW events. We confirmed that such a cancellation is not critical here. In fact, similar composite fields were obtained when each field was rotated, before averaging, so that the major axis of the equivalent ellipse at $t = 0$ (i.e., the direction of the vortex splitting) was arranged to the same direction (not shown).

2.2 Three-dimensional PV structure

Using a composite analysis, Matthewman et al. (2009) demonstrated that the S-SSW has a nearly equivalent-barotropic structure. In examining the vertical structure of our composite S-SSW, the modified PV (MPV, Lait 1994) is calculated on each isentropic surface. The MPV

is defined as the vertically weighted Ertel's PV (EPV):

$$\mathrm{MPV} \equiv \mathrm{EPV} \times \left(\frac{\theta}{\theta_0}\right)^{-9/2} = \frac{\zeta + f}{\sigma} \times \left(\frac{\theta}{\theta_0}\right)^{-9/2}, \tag{2.1}$$

where θ is the potential temperature, θ_0 is its reference, ζ is the vertical component of the relative vorticity, f is the Coriolis parameter, and σ is the density in the isentropic coordinate system. Following Matthewman et al. (2009), θ_0 is set to 475 K. The MPV is a conserved quantity along an air-parcel trajectory like EPV in the absence of friction and diabatic heating. Unlike EPV, however, the MPV exhibits small vertical dependence, so that it is suitable to examine a vertical structure of the polar vortex.

Figure 2.1 shows the snapshots of MPV at various times and heights. The polar vortex is nearly equivalent-barotropic around $t = 0$; in particular, it splits almost simultaneously over the altitude rage of $\theta = 440$ to 1150 K (about 16.8 to 37.0 km). The vortex splitting is not obvious at 400 and 1500 K. After the polar vortex splits at about $t = 2$ days, the two daughter vortices are advected westward more rapidly at high altitudes (1150 and 1500 K). These results are consistent with those of Matthewman et al. (2009).

To further clarify a vertical variation of the structure, we examine the phases of the dominant MPV components with zonal wavenumber 1 and 2. The phase with wavenumber 1 or 2 is defined as the longitude of the MPV maximum for each component. Figure 2.2 shows the time series of the MPV phases with wavenumber 1 and 2 at the various isentropic surfaces. Around $t = 0$, the phases take similar values. More precisely, the wavenumber-2 phases are concentrated around 90° between about $t = -1$ and 3 days, which corresponds to the period of the vortex splitting. On the other hand, the wavenumber-1 phases are concentrated around 0° between about $t = -3$ and 0 days before the splitting. At a later time, the phases for wavenumber 2 start to spread, and those at the higher altitudes (1150 or 1300 K) decrease more rapidly, which corresponds to a westward advection of the daughter vortices as seen in Fig. 2.1.

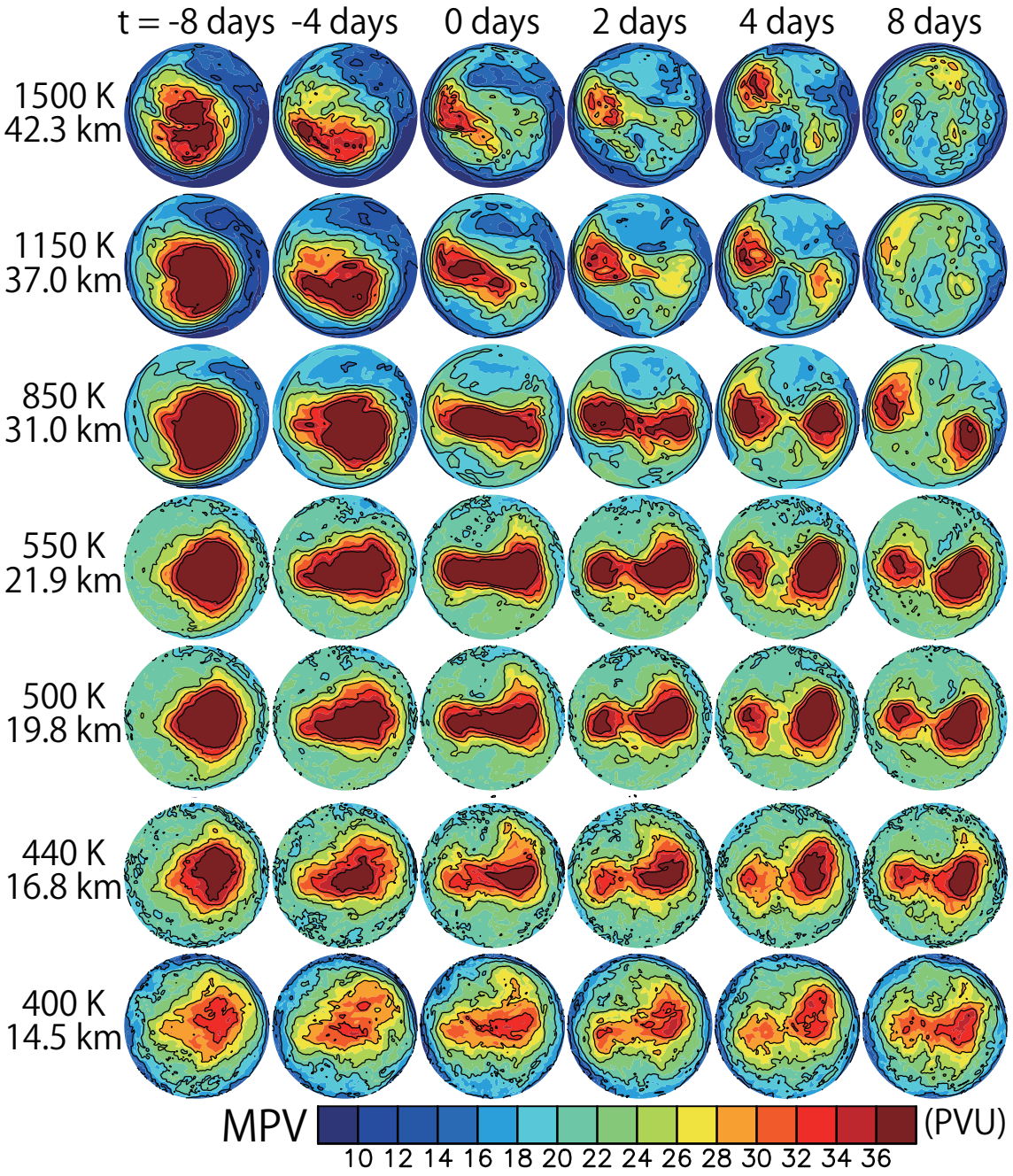

Figure 2.1: Evolution of the composite modified PV [MPV, Lait (1994)] over 30 to 90°N at the respective isentropic surfaces between 400 and 1500 K. The MPV is given by (2.1). The unit of PVU is defined as 1 PVU = 10^{-6} K m^2 s^{-1} kg^{-1}. Each lateral label represents the time-mean height of the isentropic surface at 60°N over the period of the composite SSW.

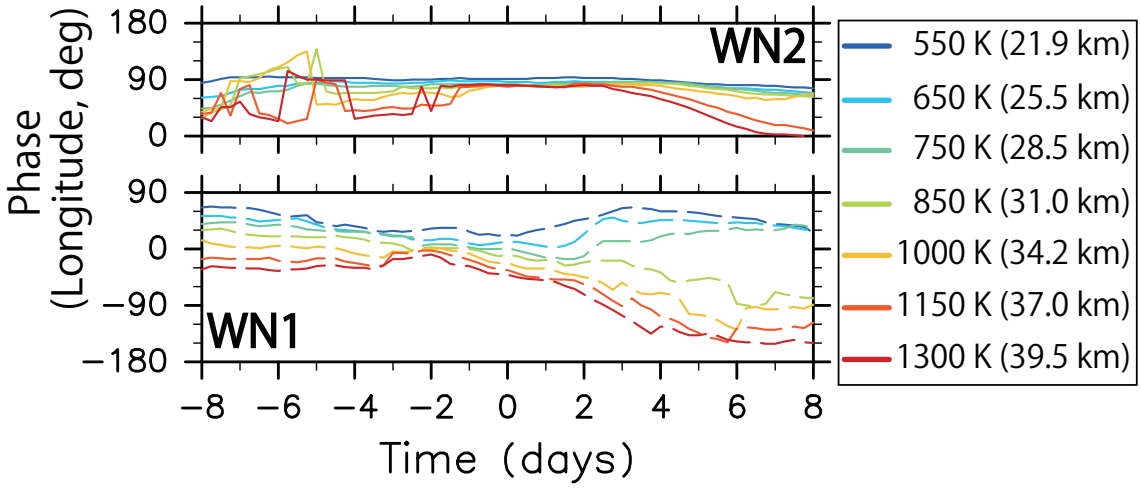

Figure 2.2: Time series of the MPV phases with wavenumber 1 and 2 at the various isentropic surfaces between 550 and 1300 K. The phase of MPV with zonal wavenumber 1 or 2 is defined as the longitude of the MPV maximum for each component. Before calculating the phase, a moving average with window size of 11.25° was applied along the latitudinal direction. The results are insensitive to the window size.

The wavenumber-1 phases after $t = 0$ also spread rapidly, but this is not important because the wavenumber-1 components at the later time are not dominant in the MPV field.

2.3 Disturbances to zonal-mean flows

The dynamics of S-SSWs is known to be captured by a framework of wave-mean flow interactions (Matsuno 1971). Esler and Scott (2005) analyzed the results of fully nonlinear three-dimensional QG simulations of a prototype S-SSW in which the initial polar vortex is equivalent-barotropic, by employing the wave activity conservation and a linear response theory. They demonstrated that the amplification of an equivalent-barotropic Rossby wave generated by a wavenumber-2 bottom forcing is essential to cause the S-SSW. In this section, we first confirm that wavenumber-2 disturbances are dominant during the composite SSW by analyzing the Eliassen-Palm (EP) flux. Subsequently, the vertical scale of the wavenumber-2 disturbances is roughly estimated.

The diagnostic of the EP flux and transformed Eulerian-mean equations is quite useful to

understand the middle-atmosphere dynamics (Andrews and McIntyre 1976, 1978; Andrews et al. 1987). In the spherical log-pressure coordinate system, the EP flux $\boldsymbol{F} = (0, F^{(\varphi)}, F^{(z)})$ and its divergence are given as

$$F^{(\varphi)} \equiv \rho_0 R \cos\varphi \left(\overline{u}_z \frac{\overline{v'\theta'}}{\overline{\theta}_z} - \overline{u'v'} \right), \tag{2.2}$$

$$F^{(z)} \equiv \rho_0 R \cos\varphi \left\{ \left[f - \frac{1}{R\cos\varphi} \left(\overline{u} \cos\varphi \right)_\varphi \right] \frac{\overline{v'\theta'}}{\overline{\theta}_z} - \overline{u'w'} \right\}, \tag{2.3}$$

and

$$\boldsymbol{\nabla} \cdot \boldsymbol{F} \equiv \frac{1}{R\cos\varphi} \left(F^{(\varphi)} \cos\varphi \right)_\varphi + \left(F^{(z)} \right)_z, \tag{2.4}$$

where z is the log-pressure height, φ is latitude, ρ_0 is the reference density, R is the earth radius, (u, v, w) is the zonal, meridional, and vertical components of the velocity, respectively, $\overline{()}$ and $()'$ denote the zonal mean and local deviation from it, respectively, and the subscripts φ and z denote the partial derivatives with respect to the meridional and vertical coordinates, respectively. Since the EP flux and its divergence consist of only the quadratic terms of the disturbances, the contributions from different zonal-wavenumber components can be exactly separated. The EP flux divergence/convergence drives the zonal-mean flows. If $\boldsymbol{\nabla} \cdot \boldsymbol{F}$ is positive (negative) somewhere, the zonal-mean zonal wind $\overline{u}$ is accelerated (decelerated) around there. If $\boldsymbol{\nabla} \cdot \boldsymbol{F} = 0$ everywhere, the mean flows are not changed with time (i.e., the non-acceleration theorem). Moreover, if the Wentzel-Kramers-Brillouin (WKB) approximation is assumed to be valid, the EP flux vector $\boldsymbol{F}$ is parallel to the group velocity of a disturbance in the latitude-height section (Edmon et al. 1980).

Figure 2.3 shows the EP flux and its divergence in the latitude-height sections for (a) wavenumber-2, (b) wavenumber-1, and (c) total components, together with the zonal-mean zonal wind $\overline{u}$. The wavenumber-2 components mainly contribute to the deceleration of $\overline{u}$, and the region with negative $\overline{u}$ is observed at $t = 4$ and 8 days. Under the assumption of the WKB

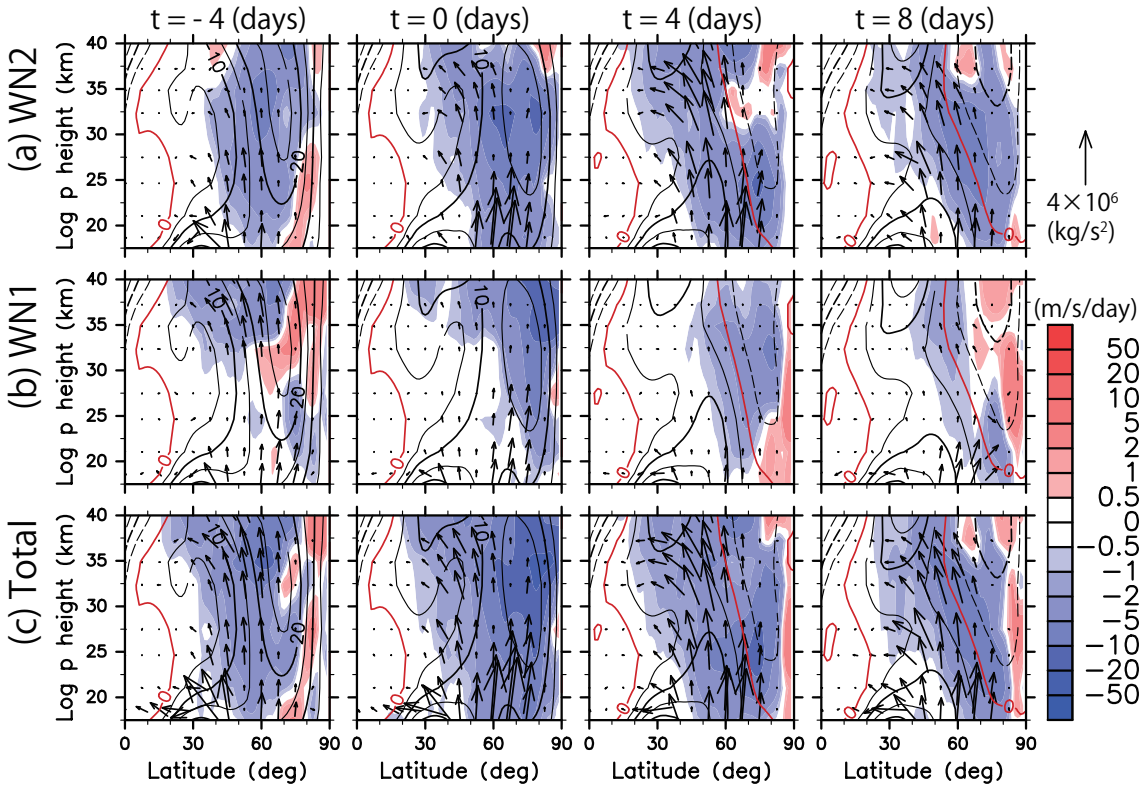

Figure 2.3: Latitude-height sections of EP flux vectors (arrows), its divergence (colors), and zonal-mean zonal wind ($\overline{u}$, contours) at $t = -4$, 0, 4, and 8 days. (a) Zonal wavenumber-2, (b) wavenumber-1, and (c) total components. Contour interval for $\overline{u}$ is 5 m s^{-1}. The red contours represent $\overline{u} = 0$. The EP flux divergence $\boldsymbol{\nabla} \cdot \boldsymbol{F}$ is multiplied by $(\rho_0 R \cos\varphi)^{-1}$ to change its unit to m s^{-1} day^{-1}.

approximation, the EP flux vectors indicate that the wavenumber-2 disturbances propagate upward along the $\overline{u} = 0$ line (the critical line for stationary waves) and then toward the equator. This upward and subsequent equatorward path can be understood by the concept of wave-guide associated with a high refractive index (Matsuno 1970).

We give a rough estimate of the vertical scale of the wavenumber-2 disturbances. If the monochromaticity is assumed, a vertical wavelength may be roughly estimated in the following four steps: (i) Two isentropic surfaces are chosen; (ii) The difference in the average height (ΔH) between the two isentropic surfaces is calculated, where an average height is given by the time mean of the geometric height of an isentropic surface at 60°N over the period of the composite SSW; (iii) The difference in the phase of wavenumber 2 ($\Delta\phi$) between the two isentropic

surfaces is calculated, where a phase (degree) is given by the longitude with the maximum of height deviation for the wavenumber-2 component of an isentropic-surface undulation; (iv) The vertical wavelength is defined by $\Delta H \times 180^\circ/\Delta\phi$. As shown in Fig. 2.3a, the negative $\overline{u}$ region appears at about $t = 4$ days, and the wavenumber-2 disturbances are dissipated along the $\overline{u} = 0$ line, which is located near the 30-km height at 60°N between $t = 4$ and 8 days. To avoid the negative $\overline{u}$ region, two isentropic surfaces are chosen among ten levels[1] between 400 and 650 K (about 14.5 and 25.5 km). The vertical wavelengths are estimated at each time for all possible pairs of isentropic surfaces (45 pairs), and the average wavelength is regarded as a vertical scale of the wavenumber-2 disturbances. Figure 2.4 shows the time series of the estimated vertical scale. The vertical scale tends to decrease from $t = -4$ to 1 days, but it slightly increases around $t = 4$ days. The vortex splitting occurs between $t = 0$ and 4 days (Fig. 2.1). During this period, the vertical scale of the wavenumber-2 disturbances is between about 70 and 100 km (on average about 85 km). This result may be consistent with that of Esler and Scott (2005). Using a linear theory with an equivalent-barotropic mean state, they estimated a vertical wavelength of Rossby waves having the maximum vertical group velocity at between 54 and 84 km.

2.4 Summary

We have constructed the composite S-SSW from JRA-55 and confirmed its equivalent-barotropic nature. The analysis of the three-dimensional MPV structure has indicated that the polar vortex is nearly equivalent-barotropic over the altitudes of about 20 to 40 km between about $t = -3$ and 3 days. To examine which wavenumber component is dominant in the disturbances during the composite S-SSW, the EP flux and its divergence have been calculated. The

[1]The ten levels are 400, 420, 440, 460, 480, 500, 520, 540, 550, and 650 K.

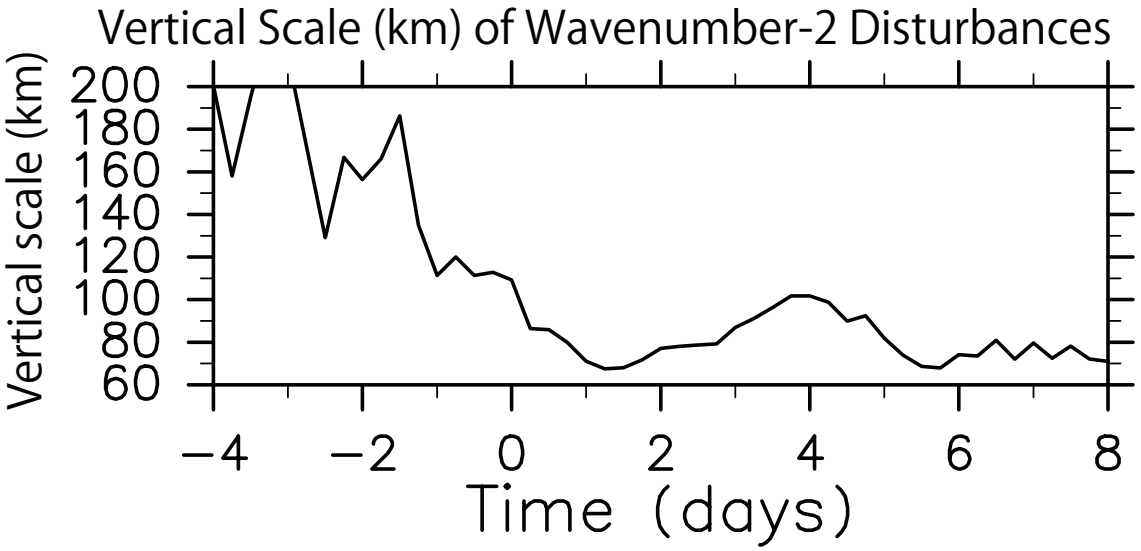

Figure 2.4: Time series of the vertical scale of the wavenumber-2 disturbances roughly estimated between 400 and 650 K (about 14.5 and 25.5 km). See text for details.

results suggest that the wavenumber-2 disturbances mainly decelerate the zonal-mean zonal flow. The vertical scale of these wavenumber-2 disturbances is roughly estimated at about 85 km, which is about four times longer than the thickness of 20 km between the heights of 20 and 40 km, over which the polar vortex is nearly equivalent-barotropic. These results suggest that the PV evolution associated with the S-SSW may be simulated by a barotropic model.

Chapter 3

Numerical Experiments Using a Quasi-Geostrophic (QG) Barotropic Model on the Sphere

Atmospheric phenomena are generally not easy to understand because they consist of motions with multiple temporal and spatial scales and also of different kinds of physical, chemical, and biological processes. A simple or theoretical model would be useful for understanding such phenomena; however, its connection to the real phenomena may be somewhat obscure. By contrast, a complex model such as a general circulation model (GCM) well reproduces real phenomena, but a complicated data analysis is necessary to understand the phenomena. Thus, there exists the model hierarchy from simple models to GCMs, and there is in general a tradeoff between the level of understandability and the level of realism (e.g., Dijkstra 2013).

In the present study, results from the equilibrium statistical mechanics are easy to understand without a data analysis because an equilibrium state has the meaning of the most probable state and a phase diagram directly shows an influence of changing a parameter on these equilibrium states. However, the statistical mechanics cannot be directly used to interpret any result from JRA-55 because it is applicable only to an isolated system without diabatic heating nor dissipation and does not give any information on the time evolution such as the relaxation toward the equilibrium state. Thus, employing a barotropic model, we will bridge the gap be-

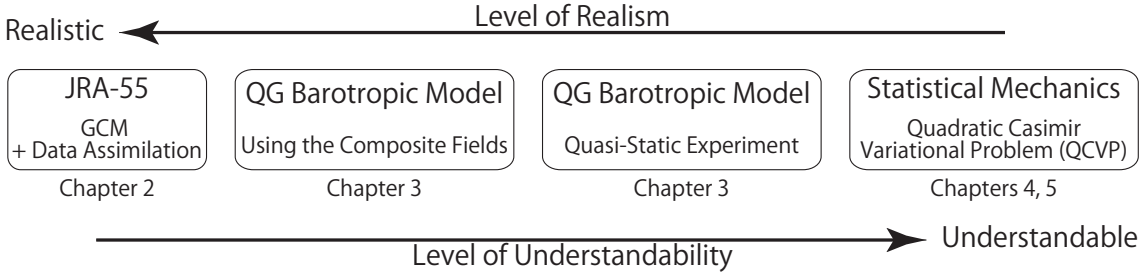

Figure 3.1: Hierarchy for the reanalysis, model, and theory used in the present study.

tween real atmospheric data (JRA-55) and the statistical mechanics. Figure 3.1 represents the hierarchy for the reanalysis, model, and theory used in the present study.

In the previous chapter, the equivalent-barotropic nature of the composite S-SSW has been confirmed. These results suggest that the essence of S-SSWs is the equivalent-barotropic motions and these motions can be described by a barotropic model. In this chapter, we construct a quasi-geostrophic (QG) barotropic model in a spherical coordinate system (Section 3.1), and demonstrate that the model well reproduces the evolution of the composite PV obtained from JRA-55 (Section 3.2). Similar one-layer models have been used in the previous studies on SSWs (e.g., Polvani and Waugh 2004; MirRokni et al. 2011; Matthewman and Esler 2011; Liu and Scott 2015; Scott 2016). However, to the best of our knowledge, it is the first time to confirm the validity of the QG barotropic model through the direct comparison with the reanalysis dataset.

In Section 3.3, a quasi-static experiment is performed to examine transitions among states of the polar vortex. In this experiment, a bottom forcing in the QG model is increased linearly and sufficiently slowly with time, while the flow field keeping nearly steady; hence, it is possible to reveal the states before and after a transition such as the polar-vortex collapse. In Chapter 5, the results of the quasi-static experiment will be interpreted by comparing with the theoretical calculations in Chapter 4.

3.1 Model description

We describe the dynamics over the altitude range of about 20 to 40 km (θ = 550 to 1300 K) by using a spherical QG barotropic model with a bottom forcing. The governing equations (e.g., Vallis 2006) are

$$\frac{\partial q}{\partial t} + \boldsymbol{v} \cdot \boldsymbol{\nabla} q = -\nu \Delta^{10} q, \tag{3.1}$$

and

$$q(\boldsymbol{x}, t) \equiv \Delta\psi(\boldsymbol{x}, t) + \underbrace{2\Omega \sin\varphi}_{f(\boldsymbol{x})} + 2\Omega \sin\varphi \; h(\boldsymbol{x}, t)/H - \underbrace{2\Omega \sin\varphi_{\mathrm{off}}}_{f_{\mathrm{off}}}, \tag{3.2}$$

where q is the PV, ψ is the stream function, $\boldsymbol{v}$ is the horizontal velocity given by $\boldsymbol{k} \times \boldsymbol{\nabla}\psi$ ($\boldsymbol{k}$ is a vertical unit vector), ν is a coefficient of hyper viscosity, Ω is the angular velocity of the earth's rotation, h is an effective bottom forcing, and H is an effective mean depth. Note that h represents the effects of large-scale disturbances propagating from the troposphere, like in other theoretical models describing SSWs (e.g., Matsuno 1971; Holton and Mass 1976; Plumb 1981a,b). A position $\boldsymbol{x}$ on the sphere is specified by a longitude λ and a latitude φ. Without loss of generality, the offset of the PV, f_{off} ($\equiv 2\Omega \sin\varphi_{\mathrm{off}}$), is introduced in (3.2), where φ_{off} = 45°N. In what follows, quantities except for time t are basically nondimensionalized using the characteristic scales such as one day, earth radius, and mean depth.

We numerically solve the governing equations (3.1) and (3.2) with the fourth-order Runge-Kutta method and the spectral method with the spherical harmonic expansion. The numerical model was constructed with the ISPACK (Ishioka 2013). All experiments below were conducted with the truncation wavenumber (in a triangular manner) T106 with the time step of 12 min. When calculating the nonlinear terms, the standard transform method is used with an alias-free grid of 320 (zonal) × 160 (meridional). Some experiments were also performed with T63, T85, and T126 to confirm the insensitivity to the truncation wavenumber. The value of ν was chosen such that the e-folding time for the modes with the highest total wavenumber was

either 80 h, 8 h, or 2.4 h. All the results are not highly sensitive to ν. Furthermore, we verified that the results are insensitive to the form of hyper viscosity: Similar results were obtained when the viscosity term in (3.1) is given by $-\nu\Delta^6 q$ or $-\nu\Delta^8 q$. Unless otherwise stated, the mean depth H is set to 6.14 km. This value is equal to a scale height defined by $R_{\mathrm{dry}}T_0/g$, where R_{dry} is the gas constant for dry air (= 287 J K^{-1} kg^{-1}), g is the gravity acceleration ($\approx$ 9.81 m^2 s^{-2}), and T_0 (= 210 K) is the climatological temperature for the midwinter over the polar cap north of 60°N in JRA-55.

3.2 Reproduction of PV evolution associated with the composite S-SSW

To compare with the QG simulations, the composite PV (3.2) is first constructed from JRA-55 in the following three steps: (i) The bottom forcing h is given at each time (every 6 h) by an undulation of the 550-K isentropic surface (at about 22 km) and is denoted by h_{cmp}; This undulation is defined at each position as the geometric height deviation of the 550-K surface from its mean height (= 21.7 km), which is the zonal average at 60°N over the period of the composite S-SSW; (ii) The barotropic relative vorticity $\Delta\psi$ in (3.2) is given at each time by vertically averaging the composite relative vorticity with a weight of density over θ = 550 to 1300 K (about 22 to 39 km); (iii) The composite PV q_{cmp} is made by substituting the obtained $\Delta\psi$ and h_{cmp} into (3.2).

For the numerical experiments, h_{cmp} is linearly interpolated in time and then it is set to the QG model. The initial PV is given by the composite PV q_{cmp} at $t = -10$ days. Numerical integration is performed from $t = -10$ to 10 days. All the following results are insensitive to the choice of the bottom isentropic surface: Similar results were obtained when the 440-K surface (at about 17 km) was used instead of the 550-K surface.

Figure 3.2 shows the evolution of (a) the bottom forcing h_{cmp}, (b) the composite PV q_{cmp},

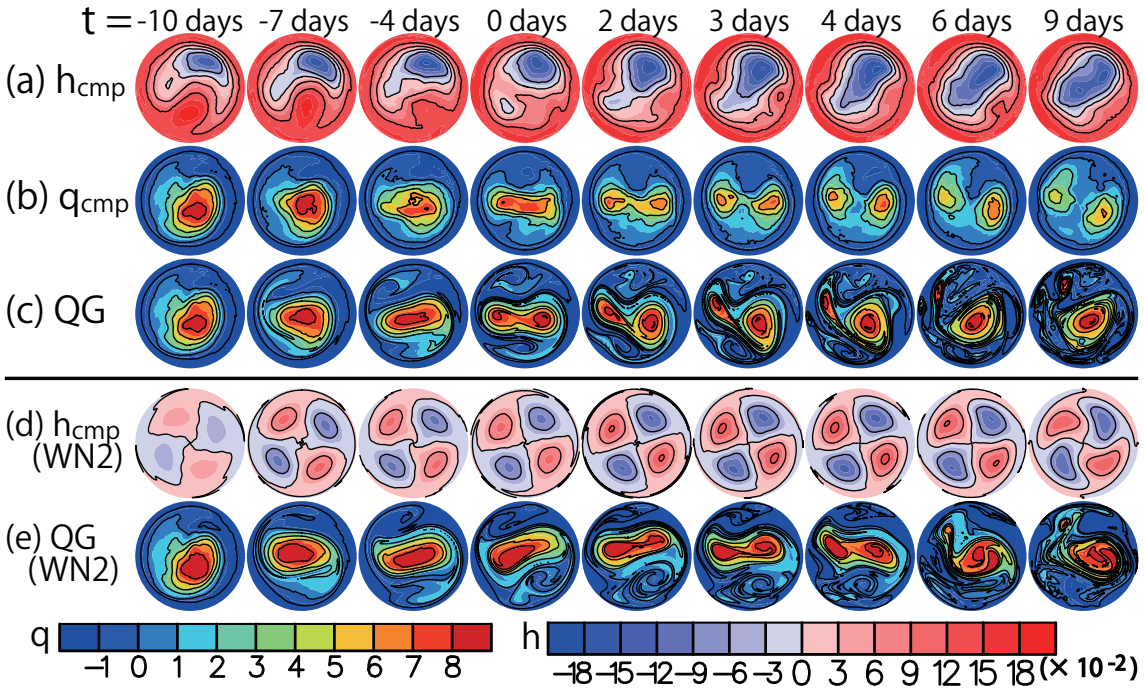

Figure 3.2: Evolution of (a) the effective bottom forcing h_{cmp}, (b) the composite PV q_{cmp}, and (c) the simulated PV q by the QG model, over 0 to 90°N. Note that h_{cmp} and q_{cmp} are made from the composite fields of JRA-55. Evolution of (d) the zonal-wavenumber-2 component of h_{cmp} and (e) the simulated PV q by the QG model with only the wavenumber-2 h_{cmp} shown in (d). The magnitude of h_{cmp} is non-dimensionalized by $H = 6.14$ km in (a) and 0.7×6.14 km in (d).

and (c) the simulated PV. The zonal-wavenumber-1 structure is observed in h_{cmp} at first, but gradually the wavenumber-2 structure becomes dominant. The PV evolution is well reproduced by the QG model until $t = 4$ days, especially before and after the vortex splitting at about $t = 2$ days. At a later time (t = 6 or 9 days), the two daughter vortices remain in the composite PV field, but only the one daughter vortex remains in the simulated field and the other becomes quite small. This is likely due to that the baroclinic structure develops after the vortex splitting, as seen in Figs. 2.1 and 2.2.

Similar experiments were also conducted for the S-SSW in February 1979 (e.g., Palmer 1981) instead of the composite S-SSW. This S-SSW event has been widely studied because it occurred during a period of intensive observation of the atmosphere [the First GARP Global Experiment, e.g., Andrews et al. (1987)]. The PV evolution was also reproduced well by the

QG model. Moreover, we found little influence of changing the initial time: A similar vortex splitting was simulated when the initial time was changed to $t = -20$ days (not shown).

Finally, we examine which zonal-wavenumber component of h_{cmp} is the most essential to the vortex splitting. Since the wavenumber 0, 1, and 2 components are predominant in h_{cmp}, only a single wavenumber component of h_{cmp} is given to the QG model and the numerical integrations are conducted. The polar vortex was elongated only in the case of the wavenumber-2 component of h_{cmp}, but its vortex splitting was not distinct. In the other cases of the wavenumber-1 and -2 components of h_{cmp}, the polar vortex remained nearly circular. These results suggest that the amplitude of each wavenumber component of h_{cmp} is too small for a vortex splitting to occur. Since a use of a smaller mean depth H results in a relatively larger amplitude of h_{cmp} in (3.2), all numerical simulations are performed again with $H = \tilde{c} \times 6.14$ km, where $\tilde{c}$ is changed between 0.7 and 0.9 with an interval of 0.1. The vortex split occurs only in the cases of the wavenumber-2 h_{cmp} with $\tilde{c} = 0.7$, 0.8, and 0.9. Figures 3.2d and 3.2e show the evolution of the wavenumber-2 h_{cmp} and simulated q with $\tilde{c} = 0.7$, respectively. These results indicate that the wavenumber-2 component of h_{cmp} is the most essential to the vortex splitting.

3.3 Quasi-static experiments

In the numerical experiments of the previous section, the details of transitions (or bifurcations) among states of the polar vortex were not clear because the time scale of the bottom forcing h_{cmp} was too short and the polar vortex evolved too rapidly. It may be useful for understanding S-SSWs to conduct an experiment with a slowly varying forcing and to pursue changes in the structure of a flow field. In fact, several studies (e.g., Matthewman and Esler 2011; Liu and Scott 2015) have argued that some transition is essential to understand S-SSWs. To examine such a transition, we conduct a quasi-static experiment where the time scale of the

forcing h is $O(10^4$ days). Due to this quite slow variation of h, the flow field is nearly steady and it is possible to reveal the states before and after a transition. This kind of method is known as continuation methods in the bifurcation theory (e.g., Seydel 2009). The set-up of the quasi-static experiment is also suitable to apply equilibrium statistical mechanics and the results will be interpreted in Chapter 5.

A link of the real S-SSW to the quasi-static experiment, in which the forcing time scale is unrealistically long, may not be clear. Before conducting such a highly idealized simulation, we perform an experiment with the forcing time scale of one week, which is a reasonable time scale of Rossby waves causing SSWs (Sjoberg and Birner 2012).

3.3.1 Preliminaries

We first describe the model configuration common to the experiments with the short and quite long time scales of h. In Section 3.2, the bottom forcing is given at each time by h_{cmp} made from JRA-55 and its zonal-wavenumber-2 component is the most essential to the vortex splitting. Moreover, Fig. 3.2d suggests that the phase of the wavenumber-2 h_{cmp} does not vary much after $t = -4$ days. Thus, a new h is defined as follows, whose spatial structure is fixed, but amplitude $a(t)$ is varied with time:

$$h_{\mathrm{QSE}} \equiv a(t) \times h_0 \ \cos[2(\lambda - \lambda_0)] \ \exp\left[-\frac{1}{2}\left(\frac{\varphi - \varphi_0}{\Delta\varphi}\right)^2\right], \tag{3.3}$$

where

$$a(t) \equiv \begin{cases} 0 & (t < 0), \\ a_{\mathrm{max}} \times \frac{t}{\Delta t} & (0 \le t \le \Delta t), \\ a_{\mathrm{max}} & (\Delta t < t). \end{cases} \tag{3.4}$$

Note that the subscript QSE stands for quasi-static experiment. Figure 3.3 compares h_{QSE} [$a(t)$ = 1] with the wavenumber-2 h_{cmp} (at the onset time). The value of h_0 is set to 420 m, which is nearly equal to the amplitude of the wavenumber-2 h_{cmp}. In the following, the magnitude of

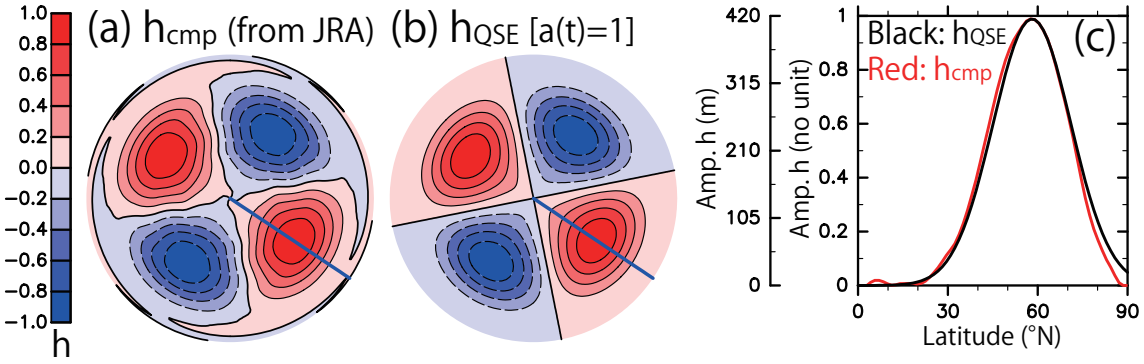

Figure 3.3: Effective bottom forcings over 0 to 90°N: (a) the zonal-wavenumber-2 component of h_{cmp} at the onset time made from JRA-55 and (b) h_{QSE} with $a(t) = 1$ defined in (3.3). The parameters h_0, λ_0, φ_0, and $\Delta\varphi$ are determined to fit h_{QSE} into the wavenumber-2 h_{cmp}: $h_0 = 420$ m, $\lambda_0 = 56.3°$, $\varphi_0 = 58.1°$N, and $\Delta\varphi = 13.0°$. (c) Cross sections of (a) and (b) on the blue lines.

h_{QSE} is normalized by h_0 and is denoted by a in (3.3). The parameters of λ_0, φ_0, and $\Delta\varphi$ are also determined to fit h_{QSE} to the wavenumber-2 h_{cmp}, as in the caption of Fig. 3.3. The parameters $a_{\max}$ and Δt will be given in the following each section.

The initial PV is given by the axisymmetric component of the barotropic, climatological, absolute vorticity $\Delta\psi + f$, which is made in the following two steps: (i) The three-dimensional, climatological, absolute vorticity is obtained by simply averaging the absolute vorticity over the 55 midwinters (December to February) in JRA-55, except for the periods of SSWs; (ii) Its barotropic component is defined by vertically averaging the obtained absolute vorticity with a weight of density over $\theta = 550$ to 1300 K (about 22 to 39 km).

3.3.2 Experiment with the forcing time scale of one week

In this subsection, we perform an experiment with the forcing time scale $\Delta t = 7$ days, where $a_{\max}$ in (3.4) is set to 2. Figure 3.4a compares the time series of $a(t)$ in (3.4) with those of the amplitude of the wavenumber-2 h_{cmp}. The time scale and amplitude of h_{QSE} are similar to those of h_{cmp}. Sjoberg and Birner (2012) analyzed reanalysis datasets (ERA-Interim and ERA-40) and showed that Rossby waves with a time scale of one week or longer tend to cause SSWs.

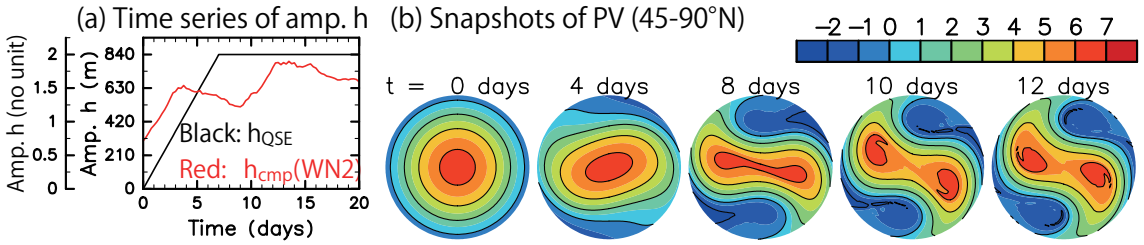

Figure 3.4: (a) Time series of the forcing amplitudes given by the wavenumber-2 component of h_{cmp} made from JRA-55 (red) and by h_{QSE} in (3.3) and (3.4) (black), where $\Delta t = 7$ days and $a_{\max} = 2$. The same wavenumber-2 h_{cmp} as that in Fig. 3.2d is used for the red time series. For comparison, the onset time is shifted to $t = 10$ days. (b) Evolution of PV over 45 to 90°N simulated by the QG model using h_{QSE}.

The choice of $\Delta t = 7$ days is consistent with their results.

Figure 3.4b shows the simulated PV evolution. Compared with Figs. 3.2c and 3.2e, a similar vortex splitting is reproduced even by using the simpler bottom forcing h_{QSE} in (3.3). This result motivates us to further investigate the transitions in the QG model by performing an experiment with a large Δt (i.e., the amplitude of h_{QSE} is slowly increased).

The vortex splitting is likely to be understood with the Love-type instability from a dynamics point of view (Matthewman and Esler 2011). The polar vortex is elongated by the increase in the bottom forcing h_{QSE}, which leads to a strong shear near the vortex center. Eventually, a kind of barotropic instability, named the Love-type instability, occurs (Love 1893). The Love-type instability has often been investigated for the Kirchhoff elliptic vortex, which consists of an elliptic high vorticity surrounded by a low vorticity. Many studies have analyzed the linear and nonlinear dynamics of the Kirchhoff vortices by using theoretical and numerical methods (e.g., Wan 1986; Tang 1987; Dritschel 1985, 1986; Guo et al. 2004). Mitchell and Rossi (2008) numerically investigated the nonlinear evolution of the Kirchhoff vortices in the two-dimensional plane. They demonstrated that the wave-wave interaction between wavenumber-2 perturbations makes a wavenumber-4 perturbation and this perturbation develops the Kirchhoff vortex into a vortex splitting or a filamentation structure, depending on the phase of the wavenumber-4

perturbation. The latter filamentation structure likely corresponds to a state developed during the breakdown of the polar vortex in the next subsection (Fig. 3.6b).

The evolution over a long period is examined next. Figure 3.5 shows the evolution of stream function and PV, together with the structure of the bottom forcing h_{QSE} [$a(t) = 2$] and the time series of the following quantities: total PV Γ, total energy E, and potential enstrophy S, where

$$\Gamma = \int q \, \mathrm{d}A, \tag{3.5}$$

$$E = \frac{1}{2} \int (\boldsymbol{\nabla}\psi)^2 \, \mathrm{d}A, \tag{3.6}$$

$$S = -\frac{1}{2} \int q^2 \, \mathrm{d}A, \tag{3.7}$$

dA is an area element, and S is also called the entropy as explained in Section 1.3.1. Significant changes in the PV field occur over the North Pole, and we focus on the polar cap over 45 to 90°N. All surface integrals in (3.5) – (3.7) are taken over this polar cap.

The polar vortex gradually breaks down after the vortex splitting shown in Fig. 3.4b. The entropy S is rapidly increased by the vortex splitting and then it is gradually increased, associated with the PV mixing shown in the right column of Fig. 3.5b. The total PV Γ and energy E evolve in similar ways. The flow field reaches a nearly steady state at about $t = 1000$ days. This final state is anti-cyclonic, as seen in the stream function, and the flow field is elongated along the direction of the h_{QSE} maxima.

3.3.3 Experiment with the forcing time scale of $O(10^4$ days)

We perform a quasi-static experiment with the forcing time scale of $O(10^4$ days) to investigate the transitions inherent in the QG barotropic system. The parameters Δt and $a_{\max}$ in (3.4) are set to 2.8×10^4 days and 1, respectively. The following results are insensitive to Δt. In fact, similar results were obtained when $\Delta t = 1.4 \times 10^4$ days, which indicates that the variation in the forcing amplitude $a(t)$ is sufficiently slow. Without loss of generality, λ_0 in (3.3) is set to zero.

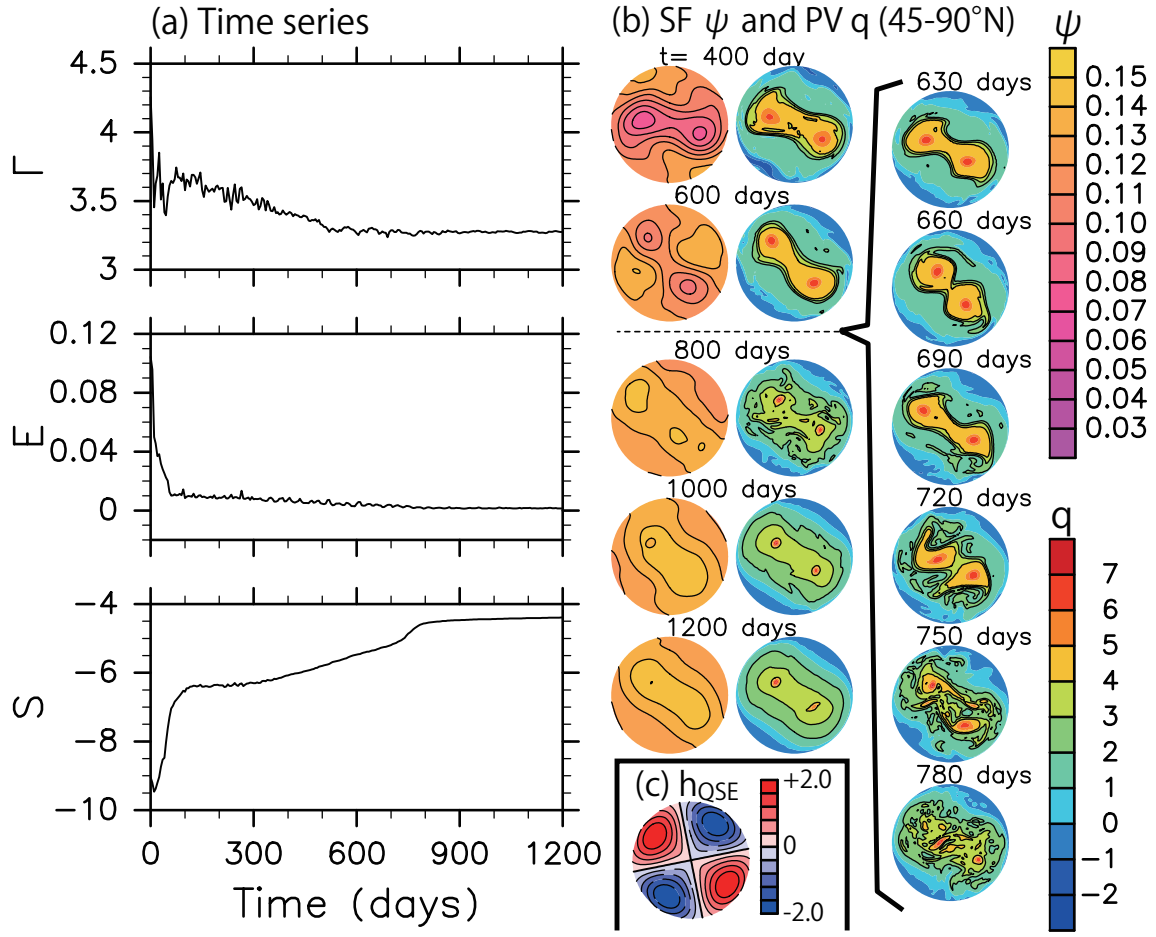

Figure 3.5: Results of the QG experiment using h_{QSE} in (3.3) and (3.4) with $\Delta t = 7$ days and $a_{\max} = 2$. (a) Time series of the total PV Γ, the total energy E, and the entropy S (i.e., the negative of potential enstrophy). Those quantities are defined in (3.5), (3.6), and (3.7). (b) Evolution of stream function (SF) ψ and PV q over 45 to 90°N. (c) Effective bottom forcing h_{QSE} with $a(t) = 2$ over 45 to 90°N. The parameters of h_{QSE} are the same as those in Fig. 3.3.

Note that the initial PV is axisymmetric (Section 3.3.1). We also perform a quasi-static experiment using a non-axisymmetric initial PV, including the zonal-wavenumber-1 component. Similar results to the following are obtained and shown in Appendix B.

Evolution of PV field

Figure 3.6 shows (a) the time series of Γ, E, S and the major-axis angle of the equivalent ellipse for PV, (b) the evolution of stream function and PV, and (c) the structure of the forcing h_{QSE} with $a(t) = 1$. The PV field is nearly steady, except around the two transitions. The changes in the PV field are correlated with the abrupt changes in Γ, E, and S. The first transition occurs at about $t = 7000$ days. The state before the transition is referred to as State A, in which the polar vortex is vertically elongated (i.e., the major-axis angle $\sim 0°$), as shown in the 4000th-day snapshots. The state after the transition is referred to as State B, in which the polar vortex is laterally elongated (i.e., the major-axis angle $\sim 90°$), as shown in the 11000th-day snapshots. Associated with the transition from A to B, the values of Γ, E, and S rapidly decrease. Note that the temporary increase in the major-axis angle around $t = 5000$ days (Fig. 3.6a) was not observed in some experiments using different viscosity coefficient, truncation wavenumber, or initial condition (see Fig. B.1a) and it is not discussed here.

The major-axis angle of the equivalent ellipse increases before about $t = 2000$ days and then reduces to about 0° (Fig. 3.6a). This variation is sensitive to slight changes in the initial PV (not shown). This is likely because the aspect ratio of the equivalent ellipse is close to unity (i.e., the ellipse is almost a circle) and there is a high uncertainty in the direction of its major axis, which will lead to the sensitivity of the major-axis angle. During this period, the initial axisymmetric state changes into A, which is not axisymmetric (Fig. 3.6b). For simplicity, we regard the initial axisymmetric state as A. When the forcing time scale Δt is 7 days and the initial PV is given by that of State A (i.e., the 4000th-day PV in Fig. 3.6b), a similar vortex

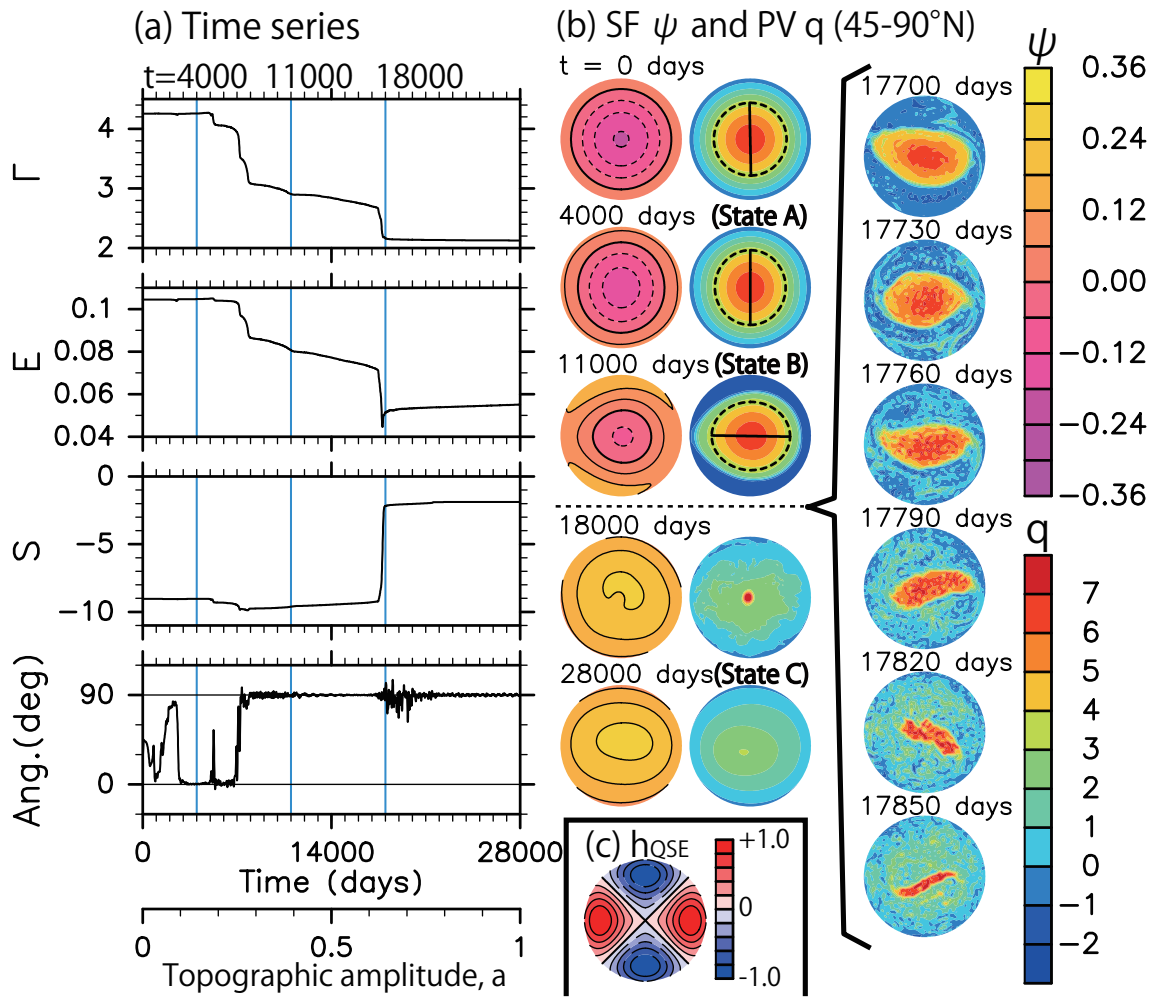

Figure 3.6: Results of the quasi-static experiment with the QG model using h_{QSE} in (3.3) and (3.4) where $\Delta t = 2.8 \times 10^4$ days and $a_{\max} = 1$. (a) Time series of the total PV Γ, the total energy E, the entropy S (i.e., the negative of potential enstrophy), and the major-axis angle of the equivalent ellipse for PV. The quantities of Γ, E, and S are defined in (3.5), (3.6), and (3.7), respectively. The equivalent ellipse for PV is obtained by following Matthewman and Esler (2011), where its major-axis angle is measured from the vertical axis in the clockwise direction. A low-pass filter with a 100-day cutoff period was applied to all time series (the results are insensitive to the cutoff period). (b) Evolution of stream function (SF) ψ and PV q over 45 to 90°N. In some PV snapshots, the equivalent ellipses are drawn by the dashed curves and their major axes by the solid lines. (c) Effective bottom forcing h_{QSE} with $a(t) = 1$ over 45 to 90°N. The parameters of h_{QSE} are the same as those in Fig. 3.3, except for $\lambda_0 = 0°$.

splitting to that in Fig. 3.4b is reproduced. Furthermore, when Δt is 2.8×10^4 days (quasi-static) and the initial PV includes all zonal-wavenumber components (not axisymmetric), a state similar to A appears (Fig. B.1). These results imply that the emergence and persistence of State A is not highly sensitive to the initial PV, and give the validity that the initial state is regarded as A.

The second transition occurs at about $t = 18000$ days, accompanied by the polar-vortex collapse (the right column in Fig. 3.6b). The PV filaments are peeled off the polar vortex, and eventually the polar vortex breaks down without splitting. Before this transition, the flow field is at State B (e.g., the 11000th-day snapshots). The state sufficiently after the transition is referred to as State C, in which the weak PV patch is laterally elongated, as shown in the 28000th-day snapshots. Associated with the transition from B to C, the values of Γ and E rapidly decrease, but that of S rapidly increases due to the strong PV mixing. Just after the transition, the small PV patch remains (e.g., the 18000th-day snapshots), but it is dissipated at about $t = 21500$ days and the flow field reaches State C.

More importantly, State B as well as A is cyclonic, whereas C is anti-cyclonic, as seen in the stream functions (the left column in Fig. 3.6b). In the experiment of the previous subsection with $\Delta t = 7$ days, a similar final state to C was obtained (Fig. 3.5b), in which the flow field is elongated along the direction of the h_{QSE} maxima, like that of C. These results indicate that the final state C is not sensitive to the forcing time scale Δt, but the vortex splitting and the emergence of State B, namely the transition paths to the final state C, depend on Δt.

Liu and Scott (2015) conducted the parameter sweep experiments where the forcing amplitude was increased linearly and slowly with time, like in our quasi-static experiment, by using spherical one-layer models (QG and shallow-water) with a wavenumber-2 bottom forcing. Their parameter space is spanned by the angular frequency of the forcing as well as the

forcing amplitude. They obtained a similar regime diagram to that in the f-plane barotropic model (Matthewman and Esler 2011), even using the spherical systems with/without a radiative relaxation. They also observed similar two transitions to those in our experiment. The difference from our results is that the flow field corresponding to State B oscillates much more strongly (they called it the oscillating regime). This difference is likely attributable to the forcing frequency, which is zero in our experiment.

Variations in the integrated quantities

Finally, we investigate causes for the variations in Γ, E, and S. Their budgets are governed by the following equations:

$$\frac{\mathrm{d}\Gamma}{\mathrm{d}t} = -\nu \int \Delta^{10} q \, \mathrm{d}A - \int \boldsymbol{\nabla} \cdot (\boldsymbol{v} q) \, \mathrm{d}A, \tag{3.8}$$

$$\frac{\mathrm{d}E}{\mathrm{d}t} = \nu \int \psi \Delta^{10} q \, \mathrm{d}A + \int \boldsymbol{\nabla} \cdot \left(\boldsymbol{v} q \psi + \psi \frac{\partial}{\partial t} \boldsymbol{\nabla} \psi \right) \mathrm{d}A + \int \frac{\psi f}{H} \frac{\partial h_{\mathrm{QSE}}}{\partial t} \, \mathrm{d}A, \tag{3.9}$$

and

$$\frac{\mathrm{d}S}{\mathrm{d}t} = \nu \int q \Delta^{10} q \, \mathrm{d}A + \int \boldsymbol{\nabla} \cdot \left(\boldsymbol{v} \frac{q^2}{2} \right) \mathrm{d}A, \tag{3.10}$$

where all integrations are taken over the polar cap of 45 to 90°N. Note that if the viscosity coefficient ν is zero and if all integrations are taken over the whole sphere, Γ and S are conserved, but E can be changed by variations in h_{QSE} [i.e., the last term in (3.9)].

Figure 3.7a shows the time series of each term in the energy budget (3.9). Obviously, E is varied at the two transitions ($t \sim 7000$ and 18000 days) primarily by the energy fluxes across 45°N. Similarly, Γ is varied primarily by the PV fluxes (not shown). Figure 3.7b shows the time series of each term in the entropy budget (3.10). The abrupt change in S at the first transition ($t \sim 7000$ days) is mainly due to the flux term, like Γ and E, but its change at the second transition ($t \sim 18000$ days) is due not only to the flux term but also to the viscosity term. At the second transition, the small-scale structures develop (Fig. 3.6b), the entropy S is transferred

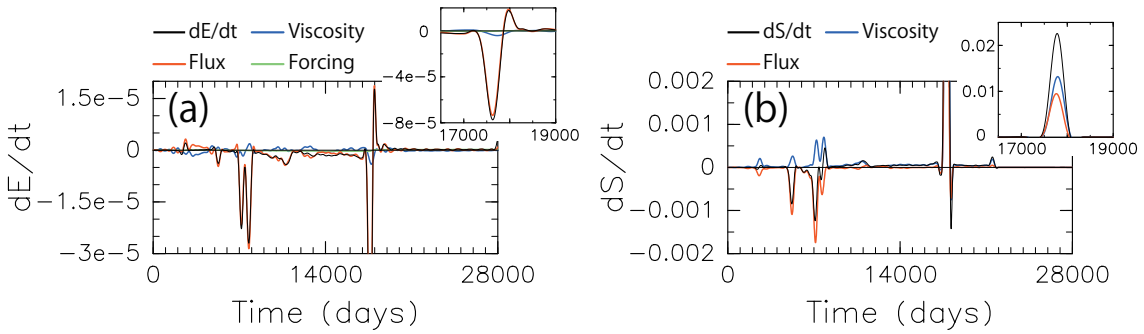

Figure 3.7: Time series of each term in (a) the energy budget (3.9) and (b) the entropy budget (3.10) in the quasi-static experiment. The label Viscosity denotes the first terms on the right hand sides of (3.9) and (3.10), Flux the second ones of (3.9) and (3.10), and Forcing the third one of (3.9). Each inset shows the time series around the polar-vortex collapse. A low-pass filter with a 500-day cutoff period was applied to all time series (the results are insensitive to the cutoff period).

into smaller scales, and it is finally dissipated by the numerical viscosity. These results are not highly sensitive to the viscosity coefficient ν: Similar time series to those in Figs. 3.6a and 3.7 were obtained even when ν was ten times as large as the present value.

3.4 Summary

The spherical QG barotropic model with the effective bottom forcing h has been constructed on the basis of the equivalent-barotropic nature of S-SSWs. To estimate the model validity, the simulated PV evolution has been compared with the composite PV evolution made from JRA-55. The QG barotropic model well reproduces the composite PV evolution during the period before the baroclinic structure develops in the composite S-SSW. This result indicates that the QG barotropic model well describes the equivalent-barotropic processes associated with the vortex splitting.

We have also conducted the QG simulations including only a single zonal-wavenumber component of h to reveal which component is the most essential to the vortex splitting. The vortex splitting occurs only in the experiments with the zonal-wavenumber-2 h.

In these experiments, the polar vortex evolves too rapidly due to the short time scale of the

forcing h. To investigate state transitions of the polar vortex, the quasi-static experiment has been performed, where the forcing amplitude is increased linearly and sufficiently slowly with time, while its spatial distribution is fixed to the wavenumber-2 structure. The flow field is nearly steady except around the two transitions, and the three quasi-steady states are observed, which are named A, B, and C. In the first transition from A to B, the flow remains cyclonic, but the shape of the polar vortex changes. In the second transition from B to C, the polar vortex breaks down without splitting, and the flow changes from cyclonic to anti-cyclonic. We have also conducted the same experiment as the quasi-static one except for the forcing time scale of one week (not sufficient slow). In this case, the polar vortex splits during the transition from A to C, and State B does not appear. These results indicate the final state C is not sensitive to the forcing time scale, but the transition path such as the vortex splitting and the emergence of State B depends on the forcing time scale.

Chapter 4

Theoretical Calculations Based on Equilibrium Statistical Mechanics

In the previous chapter, we have observed the drastic changes in the large-scale flow structure and the self-organization of the anti-cyclonic flow pattern after the polar-vortex breakdown in the QG barotropic model. Such a drastic change is reminiscent of a phase transition in statistical mechanics. Phase transition is a typical example of cooperative phenomena. Let us first consider a system consisting of quite many (the order of Avogadro's number) particles. Each particle is governed by the equation of motion including the two-body interactions (e.g., Coulomb interactions) with the other particles, but apparently there exists no law governing the entire system. When the temperature is slowly varied, for instance, the entire system suddenly changes from liquid to gas at some boiling point, even though the form of the equations of motion and the parameters (e.g., mass and charge of each particle) are not changed at all. Such a phenomenon does not occur in a system composed of a few particles, but it occurs as a results of the interactions among quite many particles. This kinds of cooperative phenomena are observed in many systems, often accompanied by self-organizations or pattern formations. The related concepts and methods are now applied in many fields: physics, chemistry, biology, computer science, economics, and social science.

It is well known that there exists the analogy between point-vortex systems and many-

particle systems. In fact, the motion of point vortices is governed by the Hamiltonian equations and the interaction between two point vortices is described by a similar function to the Coulomb potential. On the basis of this analogy, it may be possible to understand the behaviors of fluid systems consisting of quite many point vortices, by applying equilibrium statistical mechanics. This attempt was first carried out by Onsager (1949), and later by some researchers (e.g., Salmon et al. 1976; Kraichnan and Montgomery 1980). Recently, the equilibrium statistical mechanics for geophysical flows has made great progress (e.g., Salmon 1998; Majda and Wang 2006; Bouchet and Venaille 2012), as the Miller-Robert-Sommeria (MRS) theory has been developed (Miller 1990; Robert 1991; Robert and Sommeria 1991), which is the most general statistical-mechanics theory so far including the previous theories as the particular limits.

In this chapter, we apply a statistical-mechanics theory to a QG barotropic system on a disk domain. This theory is a subclass of the MRS theory (Bouchet 2008), and called the quadratic Casimir variational problem (QCVP). A brief review on the QCVP is given in Section 4.1. The equilibrium and quasi-stationary states are examined in Sections 4.2, and 4.3, respectively, where a quasi-stationary state is a saddle point of the entropy. The main result is that the mean state of the winter stratosphere accompanied by the polar vortex may be regarded not as the equilibrium state but as a quasi-stationary state. In Section 4.4, we show the possibility of transition with changing some parameters such as total energy and forcing amplitude. Although the configuration considered here is aimed at understanding S-SSWs, this chapter is somewhat independent and refers to few results in the previous chapters. In the next chapter, the theoretical calculations performed here will be compared with the results of the quasi-static experiment.

4.1 Quadratic Casimir variational problem (QCVP)

The quadratic Casimir variational problem (QCVP) is given as follows (Chavanis and Sommeria 1996; Venaille and Bouchet 2009, 2011b; Naso et al. 2010):

$$\max_{q} \left\{ S \equiv -\frac{1}{2} \int q^2 \, \mathrm{d}A \;\middle|\; E, \Gamma \right\}. \tag{4.1}$$

where

$$E \equiv \frac{1}{2} \int (\boldsymbol{\nabla}\psi)^2 \, \mathrm{d}A, \tag{4.2}$$

$$\Gamma \equiv \int q \, \mathrm{d}A, \tag{4.3}$$

and

$$q(\boldsymbol{x}) \equiv \Delta\psi(\boldsymbol{x}) + \left[f(\boldsymbol{x}) - f_{\mathrm{off}} \right] + f(\boldsymbol{x}) \, h(\boldsymbol{x})/H. \tag{4.4}$$

The formula (4.1) means that S is maximized by varying q subject to the two constraints of constant E and Γ. The above definitions of the entropy S, total energy E, total PV Γ, and PV q are the same as those in Chapter 3 [i.e., (3.7), (3.6), (3.5), and (3.2), respectively]. The entropy maximizer q is referred to as the equilibrium state. As stated in Section 1.3.1, an overwhelming number of possible states specified by the constant E and Γ are associated with the equilibrium state. In other words, if one state were picked up at random among all the possible ones and if a spatial coarse-graining were performed, the equilibrium state would be recovered.

Any stationary point, i.e., a state with the first variation of S being zero under the two constraints of E and Γ, satisfies the following linear q-ψ relation

$$q = b\psi - c, \tag{4.5}$$

where b and c are Lagrange multipliers, depending implicitly on the two constraints of E and Γ. This relation means that a streamline is identical to the corresponding PV contour; hence, any stationary point for the QCVP is an exact steady solution of the QG barotropic system [(3.1)

and (3.2), where $\nu = 0$]. In addition to the equilibrium state, we focus on a local maximum and a saddle point of the entropy in the QCVP, which are referred to as metastable state and quasi-stationary state, respectively.

An important difference between these three states is dynamical stability. In general, a state corresponding to a local maximum/minimum of a conserved quantity is dynamically and nonlinearly stable against any small-amplitude perturbation, but a state corresponding to a saddle point is not necessarily stable and may be destabilized by some perturbation (e.g., Arnold 1965; Holm et al. 1985; Swaters 1999; Majda and Wang 2006). Figure 4.1 explains why a local maximum of a conserved quantity is dynamically stable. Since the entropy S is conserved in an inviscid flow, the equilibrium and metastable states are dynamically stable, but the quasi-stationary states are not necessarily stable (Ellis et al. 2002; Venaille and Bouchet 2011b; Naso et al. 2010). This is the reason for referring to the latters as "quasi"-stationary states. The stability of saddle points is unclear, unless a linear stability analysis is performed or the time evolution of perturbations are obtained by solving the (nonlinear) QG equations. However, recent studies suggest that the state of a system may approach the nearest saddle point in the phase space and remain there for a long time (e.g., Majda and Wang 2006; Naso et al. 2010).

Bouchet (2008) revealed that the QCVP belongs to a subclass of the MRS theory. More precisely, if an appropriate global PV distribution is considered, any maximum and local maximum of the entropy S in the QCVP are always a maximum and a local maximum of the mixing (or Shannon) entropy in the MRS theory, respectively, but the converse is not necessarily true. According to the large deviation theory (e.g., Touchette 2009; Campa et al. 2014), this result means that the equilibrium entropy of the QCVP is asymptotically equal to the Boltzmann entropy. In other words, the equilibrium state given by the QCVP is overwhelmingly common. Even if an appropriate global PV distribution is not considered, the entropy S has a one-to-one

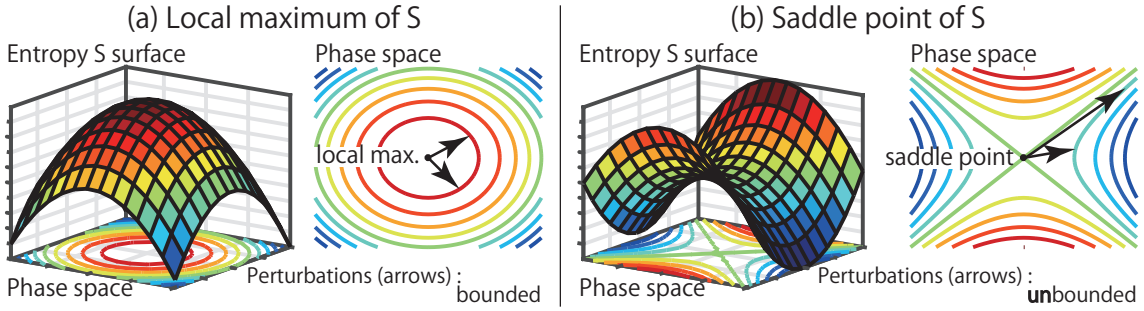

Figure 4.1: Schematic illustrations of the entropy S surface near (a) a local maximum and (b) a saddle point in the phase space. The local maximum and saddle point correspond to steady states. Arrows represent perturbations added to the steady states. The motion of each perturbation is governed by the nonlinear QG equations. In (a), the contours of S are closed around the local maximum, which means that small-amplitude perturbations are bounded and cannot grow because perturbations evolve along a single contour of S (i.e., S is conserved). A similar discussion can be made for a local minimum of S, if it exists. On the other hand, in (b), the contours of S are not closed around the saddle point, which means that small-amplitude perturbations are unbounded and may grow. The evolution of a perturbation is unknown, unless the nonlinear QG equations are solved. In this sense, nonlinear stability theorems give a sufficient condition for the stability (i.e., a necessary condition for the instability).

correspondence to the mixing (or Shannon) entropy, when a probability density function of PV is Gaussian (Naso et al. 2010).

Finally, we give a few remarks on the application of statistical-mechanics theories, including the QCVP. Equilibrium statistical mechanics is applicable only to an isolated fluid system without dissipation nor forcing, where forcing means an external forcing that varies conserved quantities such as total energy. For instance, when the bottom forcing h is not varied with time, it is not an external forcing because the total PV Γ and energy E are conserved [(3.8) and (3.9)] and the constraints of the QCVP (4.1) are invariant in time. By contrast, when h is time-dependent, Γ is conserved, but E is not; hence, h is an external forcing.

Practically, a fluid system is changed by an external forcing or dissipation. In this case, statistical mechanics is applicable if the inertial time scale (for instance, given by the eddy turnover time) is much smaller than the forcing and dissipation time scales. The system needs to move around a large region in the phase space, before the constraints given by the conserved

quantities are varied much by the external forcing or dissipation. It may then be natural to consider that the system relaxes toward the equilibrium state because the equilibrium state is overwhelmingly common and occupies a large portion of the phase space. This discussion is not a proof that a fluid system always relaxes toward the equilibrium state. Equilibrium statistical mechanics does not give any information on the time evolution. The relaxation toward the equilibrium state is still an open question, even for isolated systems without any forcing nor dissipation. In fact, recent studies of non-equilibrium statistical mechanics suggest that the relaxation in long-range interacting systems (including two-dimensional fluid systems) may be quite slow compared with short-range interacting systems, and in some systems the relaxation time diverges as taking the thermodynamic limit (e.g., Campa et al. 2014). In other words, the equilibrium states are not necessarily attractive fixed points.

4.2 Equilibrium states

The aim of this section is to show that the equilibrium state is anti-cyclonic at a realistic parameter set, which implies that the typical state of the winter stratosphere associated with the cyclonic polar vortex cannot be regarded as an equilibrium state.

If the polar cap (45 – 90°N) is assumed to be a closed domain, the equilibrium state is computed by solving the QCVP. The equilibrium states are easily expressed in terms of Laplacian eigenmodes (Chavanis and Sommeria 1996; Venaille and Bouchet 2009, 2011b; Naso et al. 2010). However, computing those eigenmodes over a polar cap (a part of the sphere) leads to technical difficulties because the eigenmodes do not have a simple analytic expression such as the spherical harmonics. For this reason, we consider a simpler geometry, namely a disk domain, which is obtained by projecting the polar cap over 45 to 90°N into the plane (x, y) with

Lambert's azimuthal equal-area projection:

$$\begin{cases} x &= \sqrt{2(1-\sin\varphi)}\cos\lambda, \\ y &= \sqrt{2(1-\sin\varphi)}\sin\lambda. \end{cases} \tag{4.6}$$

The values of Γ, E, and S are invariant under Lambert's projection because they are the surface integrals of scalars and Lambert's projection preserves the area element. This point facilitates the comparisons of theoretical calculations with the numerical-simulation results (Chapter 5).

The Coriolis parameter $f(\boldsymbol{x})$ and the effective bottom forcing $h(\boldsymbol{x})$ are also projected with Lambert's map. The projected f is a monotonic function having the maximum at the origin $[(x, y) = (0, 0)]$, which corresponds to the North Pole. The effect of the earth curvature is partially taken into account, even though the disk on the plane is considered. We use the same bottom forcing as h_{QSE} used so far [(3.3) and (3.4)]. The spatial structure of h_{QSE} is fixed, while its amplitude is controlled by a. The projected h_{QSE} with $a = 1$ is shown in Fig. 4.2a.

A stationary point of the QCVP is determined by the three parameters[1] : the forcing amplitude a, the total PV Γ, and the total energy E. The calculation method to obtain the equilibrium states is described in Appendix C and the expressions of Laplacian eigenmodes in Appendix D.

The three parameters are fixed to $(a, \Gamma, E) = (0.15, 4.2, 0.10)$ for the moment, which are close to the values taken on the 4000th day in the quasi-static experiment (see Fig. 3.6a). This suggests that these values are in a parameter range relevant to the winter stratosphere. Figure 4.2b shows the equilibrium PV and stream function (SF). The PV is minimum at the origin (corresponding to the North Pole), but the stream function is maximum there, which means that the equilibrium state is anti-cyclonic. Similar results are obtained in all the parameters covered

[1] Because time does not matter for the QCVP, it is always possible to choose time unit such that $E = 1$. Thus, we are left only with two parameters, namely, the forcing amplitude a and the total PV Γ. However, the transformation of time unit makes it a little difficult to compare the theoretical calculations with the numerical-simulation results. Thus, we consider here the three parameters of a, Γ, and E.

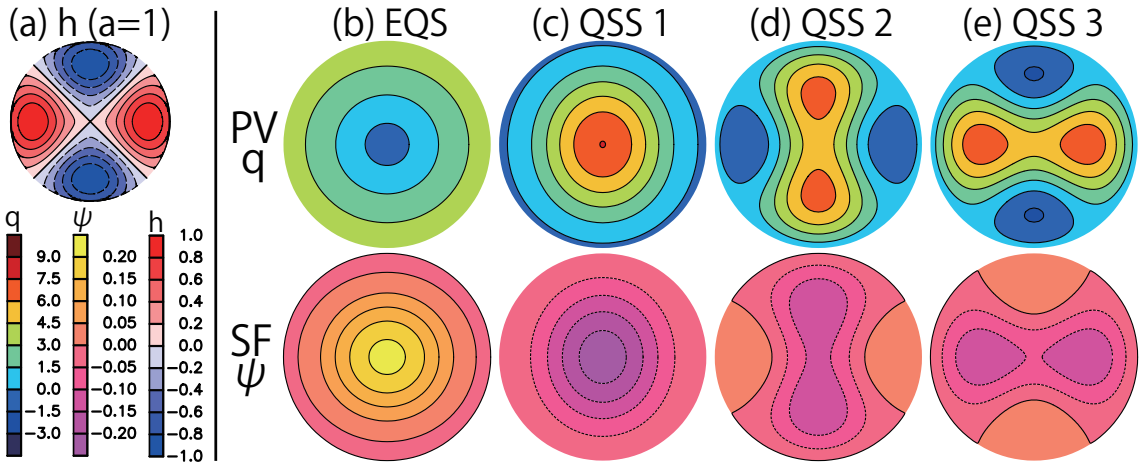

Figure 4.2: (a) Effective bottom forcing h_{QSE} over 45 to 90°N projected onto the plane with Lambert's azimuthal equal-area projection (4.6). (b) – (e) Theoretically calculated PV q and stream function (SF) ψ of (b) the equilibrium state (EQS), (c) QSS 1, (d) QSS 2, and (e) QSS 3, where QSS n stands for the quasi-stationary state having the n-th largest b in (4.5). The parameters are fixed to $(a, \Gamma, E) = (0.15, 4.2, 0.10)$.

by the quasi-static experiment. Thus, the mean state of the winter stratosphere, in which the cyclonic polar vortex exists over the North Pole, may not be considered as an equilibrium state.

4.3 Quasi-stationary states

Naso et al. (2010) pointed out that a cyclonic state may exist as a quasi-stationary state even when an equilibrium state is anti-cyclonic. In the QCVP, there are infinitely many quasi-stationary states, where small-scale structures become dominant, as the inclination b in (4.5) is decreased (Chavanis and Sommeria 1996). In this section, we investigate a few quasi-stationary states having large b. Note that any metastable state does not exist in a disk domain according to Naso et al. (2010) (see also Appendix E). The calculation method to obtain the quasi-stationary states is described in Appendix C.

Figures 4.2c to 4.2e show the three quasi-stationary states at $(a, \Gamma, E) = (0.15, 4.2, 0.10)$, where QSS n stands for the quasi-stationary state having the n-th largest b. The three quasi-stationary states are cyclonic flows, as seen in their stream functions. The PV patches of QSS 1

and 2 are vertically long, but that of QSS 3 is laterally long. QSS 1 has the largest structure due to the largest b, and its PV is maximum at the origin (corresponding to the North Pole). The mean state of the winter stratosphere where the North Pole is covered with the cyclonic polar vortex appears to be similar to QSS 1.

4.3.1 Interpretations of flow structures in terms of linear QG system

The structures of the quasi-stationary and equilibrium states in Fig. 4.2 may be understood using the linear QG equations. In this subsection, for simplicity, we consider a β-channel domain (x, y), where the meridional component of velocity is zero along the sidewalls at $y = 0$ and L and the periodic boundary condition is imposed in the x direction (the period is 2π). The mean state is assumed to be a uniform zonal flow $\boldsymbol{U} = (U, 0)$. The linear QG equations are derived from (3.1) and (3.2):

$$\frac{\partial q'}{\partial t} + U\frac{\partial q'}{\partial x} + \beta v' = 0, \tag{4.7}$$

and

$$q'(\boldsymbol{x}, t) \equiv \Delta\psi'(\boldsymbol{x}, t) + \frac{f_0}{H}h(\boldsymbol{x}) \tag{4.8}$$

where $()'$ denotes a perturbation from the zonal flow and the Coriolis parameter is given by $f = f_0 + \beta y$ ($f_0 = \text{const}$). Since the quasi-stationary and equilibrium states are steady, a steady perturbation is considered here. Integrating (4.7) with respect to x, we obtain the following equation:

$$\Delta\psi' + \frac{\beta}{U}\psi' = -\frac{f_0}{H}h \tag{4.9}$$

Furthermore, the forcing h is assumed to be proportional to $e^{i\,2x}\sin(\pi y/L)$, which is the gravest wavenumber-2 mode. The expression of the perturbation is finally obtained:

$$\psi'(\boldsymbol{x}) = \frac{f_0}{H}\,\frac{h(\boldsymbol{x})}{\left(4 + \frac{\pi^2}{L^2}\right) - \frac{\beta}{U}} = \frac{f_0}{H}\,\frac{h(\boldsymbol{x})}{\mu_2{}' - \frac{\beta}{U}}, \tag{4.10}$$

where $4 + (\pi/L)^2$ is denoted by ${\mu_2}'$ in the most right hand side. Note that $-{\mu_2}'$ is the Laplacian eigenvalue of the gravest wavenumber-2 mode. This perturbation can be interpreted as a stationary Rossby wave forced by h.

When a quasi-stationary (or equilibrium) state is regarded as a flow in which a wavenumber-2 perturbation is superposed on an axisymmetric flow, its structure may be understood using (4.10). Note that the perturbation (4.10) is an exact steady solution for the nonlinear QG equations, like the equilibrium and quasi-stationary states, because the nonlinear term vanishes due to the assumption of monochromatic wave. We first consider the case where U is sufficiently large such that ${\mu_2}' - \frac{\beta}{U}$ is positive. According to (4.10), the stream function ψ' is in phase with the forcing h. This structure of ψ' corresponds to those of QSS 1 and 2 (Figs. 4.2c and 4.2d).

The zonal-flow speed U in (4.10) is decreased, as the amplitude of the perturbation is increased, under the condition of the constant total energy. This procedure corresponds to decreasing the inclination b in (4.5). When U is positive but sufficiently small such that ${\mu_2}' - \frac{\beta}{U}$ is negative, the stream function ψ' becomes out of phase with the forcing h, as seen in (4.10). This opposite-phase structure is observed in the stream function of QSS 3 (Fig. 4.2e). In more detail, any state whose b is smaller than $-{\mu_2}'$ has an opposite-phase structure with the forcing h, as seen in (C.5), where QSS n (≥ 3) satisfies $b < -{\mu_2}'$. This inequality corresponds to $-\beta/U < -{\mu_2}'$ [i.e., the denominator of (4.10)]. In other words, the inclination b in (4.5) can be interpreted as $-\beta/U$. Since U is positive (i.e., cyclonic flow), b is negative for QSS 1 to 3 (Figs. 4.2c to 4.2e).

The flow structure of the equilibrium state (Fig. 4.2b) is understood in a similar way. Its positive b implies a negative U, which is consistent with the anti-cyclonic-flow pattern in Fig. 4.2b. When U is negative, the denominator in (4.10) is always positive and the stream function ψ' is in phase with the forcing h. Although not clear, the stream function of the equilibrium

state is in phase with the forcing h (Fig. 4.2b).

4.3.2 Dynamical stability of quasi-stationary states

The structure of the entropy surface in the phase space is important to consider the dynamical stability (Section 4.1). For instance, if some state is a local maximum of the entropy S, it is dynamically and nonlinearly stable. Since S in (4.1) is a quadratic functional, S is expressed in terms of a quadratic form; then, the structure of the entropy surface can be analyzed with the definiteness of the quadratic form. The details of the calculations are described in Appendix E.

QSS 1, 2, and 3 are saddle points of the entropy S, but the QSS 1 has the unique property. Roughly speaking, QSS 1 is virtually a local maximum of S, and it is dynamically and nonlinearly stable against almost all small-amplitude perturbations. More precisely, in the phase space, the entropy S around QSS 1 is increased only along the two directions given by the gravest wavenumber-1 Laplacian eigenmodes. In other words, only when a perturbation having a gravest wavenumber-1 component is added to the flow field of QSS 1, the entropy S is increased and QSS 1 might be destabilized. The term gravest means that these eigenmodes have the largest structure along the radial (i.e., latitudinal) direction. The two different wavenumber-1 eigenmodes exist because of the degeneracy in a disk domain (Appendix D): one is proportional to $\sin\lambda$ and the other $\cos\lambda$. Moreover, in a general domain not having the rotational symmetry, QSS 1 can be exactly a local maximum of the entropy (i.e., metastable). In this case, QSS 1 is dynamically and nonlinearly stable against *any* small-amplitude perturbation. This result is shown in Appendix F by the theoretical calculations in a square domain.

The dynamical stability of QSS 1 (and another QSS n) is unknown, unless a linear stability analysis is performed or the time evolution of perturbations are obtained by solving the (nonlinear) QG equations. Since QSS 1 is an exact steady solution for the QG system on the disk, the QG equation can be linearized with respect to a perturbation and its growth rate is obtained

by solving the eigenvalue equation. Instead of this linear stability analysis, in Section 5.4, we will add perturbations with wavenumber 1 to the flow field regarded as QSS 1 and examine the evolution of these perturbations by using the spherical (nonlinear) QG barotropic model. These small-amplitude perturbations do not grow with time, which implies that QSS 1 is stable in the sense of Lyapunov. The linear stability analysis on the disk will make the stability of QSS 1 clearer in the future.

Here, we give a physical interpretation on why only QSS 1 is virtually a local maximum of the entropy. The details are discussed in Appendix F. The reason is that QSS 1 becomes an equilibrium state, depending on the total PV Γ. The equilibrium state is defined as the entropy maximum, which is usually unique. This uniqueness is reflected in the fact that only QSS 1 can be a local maximum of the entropy.

To explain it in more detail, let us consider the case where the total energy E is fixed and the PV q is identical to the vorticity $\Delta\psi$ ($\equiv \zeta$) [i.e., $f(\boldsymbol{x}) = 0$ for all $\boldsymbol{x}$ in (4.4)]. A similar discussion can be made in a more general situation. Figure 4.3 is a schematic illustration for the following discussion. A flow field is assumed to be composed of a positive and a negative vorticity ζ. The statistical mechanics predicts the final state after the strong vorticity mixing or after the inverse-cascade processes finish. Thus, the flow field is considered to have the largest structure consisting of a single patch of ζ. There are two cases (Fig. 4.3): in one case, the positive-vorticity patch is surrounded by the negative one; in the other case, the negative-vorticity patch is surrounded by the positive one. The former is cyclonic and called the cyclonic branch; the latter is anti-cyclonic and called the anti-cyclonic branch. The equilibrium state is the most probable state among all possible ones. This fact implies that the equilibrium state will be cyclonic when the total amount of vorticity (Γ) is sufficiently large (more precisely, $\Gamma^* < \Gamma$. see Appendix F), that is, the cyclonic branch is equilibrium (the right panel in Fig.

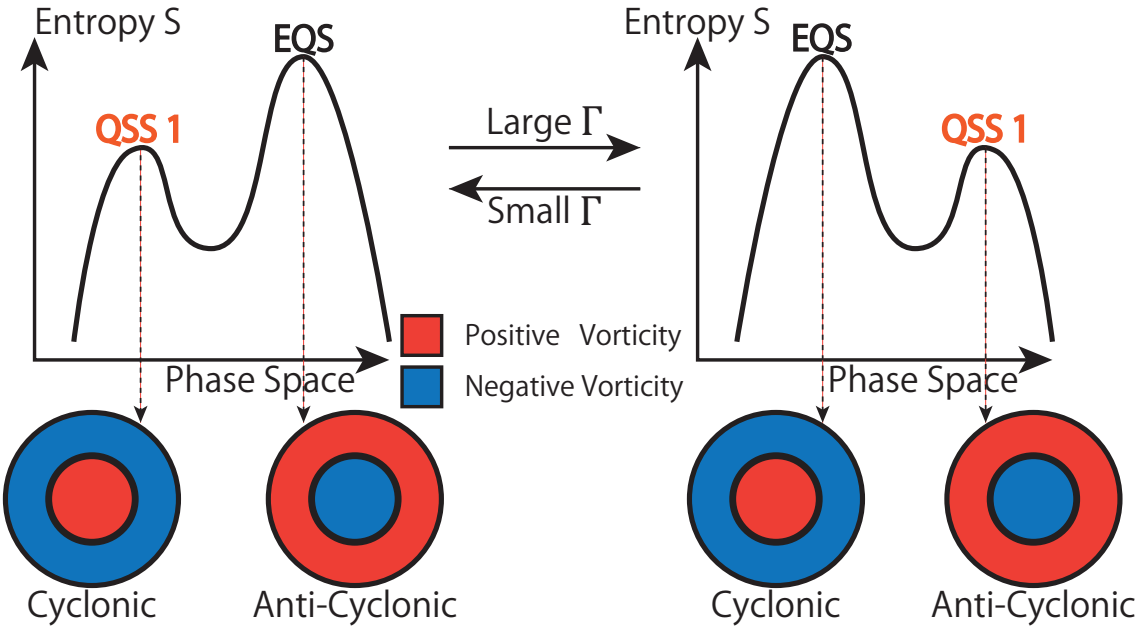

Figure 4.3: Schematic illustration for the relation between the equilibrium state (EQS) and the quasi-stationary state 1 (QSS 1). The total amount of vorticity is denoted by Γ. See text for details.

4.3). Even in this case, the anti-cyclonic flow configuration is possible and the anti-cyclonic branch exists. When Γ is decreased (from the right to the left panel in Fig. 4.3), the entropy of the cyclonic branch decreases, but that of the anti-cyclonic one increases. Eventually, the anti-cyclonic branch becomes the entropy maximum, and the cyclonic branch becomes a local maximum of the entropy or a saddle point having only a few directions along which the entropy is increased (the left panel in Fig. 4.3). This cyclonic branch is QSS 1 discussed above. Note that the equilibrium states are anti-cyclonic over all Γ covered by all experiments in Chapter 3, which implies the entropy surface considered in the present study has a similar structure to that of the left panel in Fig. 4.3.

4.4 Domains of existence of quasi-stationary states

The results in Sections 4.2 and 4.3 are at one parameter point [$(a, \Gamma, E) = (0.15, 4.2, 0.10)$]. Similar results are obtained over the parameter range of the quasi-static experiment. However,

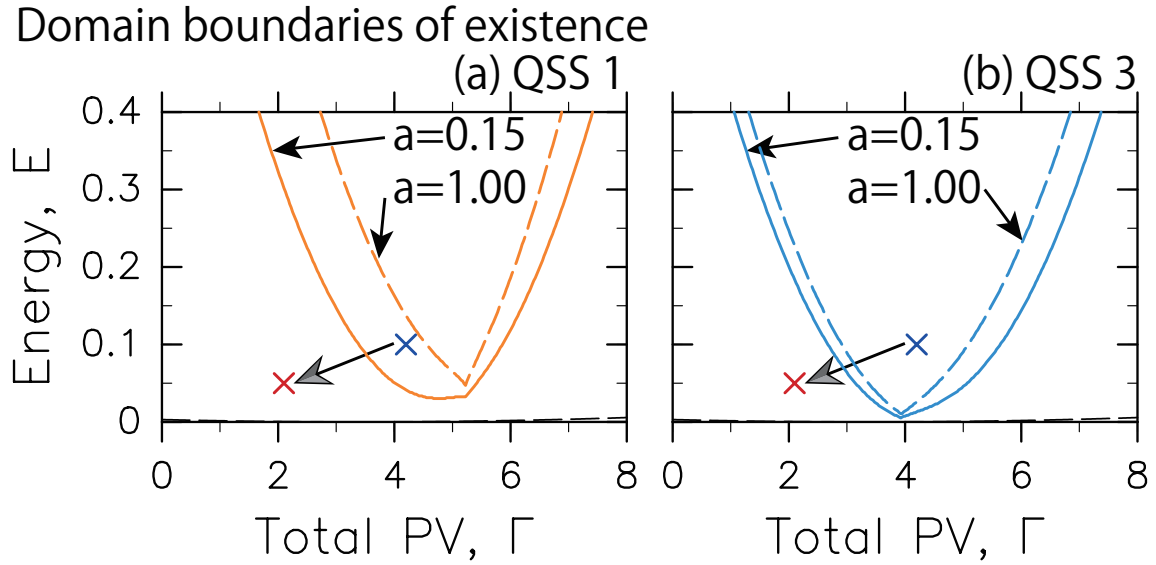

Figure 4.4: Domain boundaries of of existence of (a) QSS 1 (orange) and (b) QSS 3 (blue) in the Γ-E space with the forcing amplitude $a = 0.15$ (solid) and $a = 1.00$ (dashed). The domain boundary for the equilibrium state is also shown by the dashed black curve, where $a = 1.00$. Each state exists at higher energies than those on the domain boundary. These boundaries are theoretically obtained by using the method of Appendix C. In each figure, the blue cross is at $(\Gamma, E) = (4.2, 0.10)$, and the red one is at $(\Gamma, E) = (2.1, 0.05)$.

some quasi-stationary state does not exist in some parameter domain. In this section, we examine the parameter domains of existence of QSS 1, 2, and 3, and discuss the possibility of transition.

Figure 4.4 shows the domain boundaries of existence of QSS 1 and 3 with $a = 0.15$ and 1.00 in the Γ-E space. Each state exists at higher energies than those on the colored curve (solid for $a = 0.15$ and dashed for $a = 1.00$). The calculation method to obtain these boundaries is described in Appendix C. The domains of existence of QSS 1 and 3 become narrower and shift to regions with higher energies, as the forcing amplitude a is increased. The domain boundary for the equilibrium state is also shown by the dashed black curve, which nearly overlaps with the Γ axis in each figure. This black curve is almost independent of a, and the curve with $a = 1.00$ is shown.

The domain of existence of QSS 2 is the same as that of QSS 1 because both states annihilate

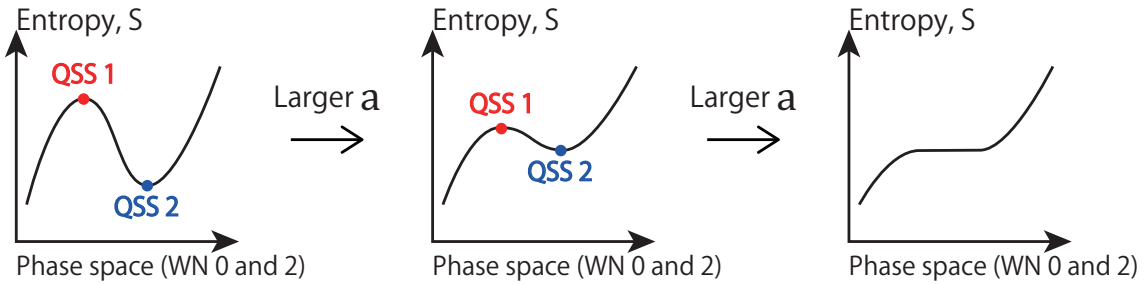

Figure 4.5: Schematic illustration for a change of the entropy surface in the phase space around QSS 1 and 2 with increasing the forcing amplitude a. In each panel, the lateral axis represents the subspace of the phase space spanned by the Laplacian eigenmodes with azimuthal wavenumber 0 and 2. A similar description is obtained when the total PV Γ or energy E is decreased.

at the same parameters. This is because the energies of QSS 1 and 2 are given by the adjacent branches of the energy curve (see Fig. C.1). Figure 4.5 is a schematic picture for a change of the entropy surface in the phase space around QSS 1 and 2. In the subspace spanned by the wavenumber-0 and -2 Laplacian eigenmodes, QSS 1 is a local maximum of the entropy S, but QSS 2 is a local minimum. When the forcing amplitude a is increased, QSS 1 and 2 annihilate at some a (Fig. 4.5).

The variations of the domain boundaries suggest the occurrence of transition. The blue cross in Fig. 4.4 is at $(\Gamma, E) = (4.2, 0.10)$, which are close to the values on the 4000th day in the quasi-static experiment (Fig. 3.6a). Let us first consider the case where Γ and E are fixed at the blue cross and the initial state is QSS 1. In Fig.4.4a, the blue cross is shifted to a parameter domain without QSS 1, as the forcing amplitude is increased to $a = 1.00$. This implies that some transition occurs because QSS 1 can no longer exist at $a = 1.00$. In addition to a, the values of Γ and E can be varied. For instance, Γ and E in the quasi-static experiment vary to around $(\Gamma, E) = (2.1, 0.05)$, i.e., the red cross in Fig. 4.4. Along this variation, both boundaries of existence of QSS 1 and 3 are crossed, which suggests again that some transition occurs. It is worth noting that equilibrium statistical mechanics, including the QCVP, does not

give any information on the time evolution such as the relaxation toward the equilibrium or a quasi-stationary state. Moreover, the statistical mechanics does not predict the variations of the total PV Γ and energy E, while these variations are obtained by solving the QG equations and then externally given to the statistical-mechanics theory. A careful analysis of numerical experiments is necessary to discuss a transition between two states. We perform this kind of analysis in the next chapter.

4.5 Summary

We have applied the QCVP to the disk domain obtained by projecting the polar cap (45 – 90°N) onto the plane with Lambert's map, and examined the equilibrium and a few quasi-stationary states. The equilibrium state is anti-cyclonic, but the quasi-stationary states are cyclonic, in the parameter range of the quasi-static experiment. Thus, the mean state of the winter stratosphere, in which the cyclonic polar vortex exists, may be considered not as the equilibrium state but as a quasi-stationary state.

We have focused on the quasi-stationary state having the largest spatial structure, which is referred to as QSS 1. This state has the unique property that QSS 1 is virtually a local maximum of the entropy. In other words, in the phase space, the entropy curve on almost every cross-section around QSS 1 is a concave parabola. The directions along which the entropy of QSS 1 is increased are given by the gravest Laplacian eigenmodes with azimuthal wavenumber 1. This unique property of QSS 1 comes from the fact that QSS 1 becomes an equilibrium state, as the total PV (Γ) is increased.

Finally, we have examined the domain boundaries of existence of quasi-stationary states in Γ-E space. The domains of existence become narrower, as the forcing amplitude a tends to be larger. This result suggests that a transition may occur when the initial state is an appropriate

quasi-stationary state and a is gradually increased.

Chapter 5

Interpretations of the Quasi-Static Experiment in terms of Equilibrium Statistical Mechanics

In this chapter, the results of the quasi-static experiment are compared with the theoretical calculations performed in the previous chapter. In Section 5.1, we first confirm that the statistical-mechanics theory, i.e., the QCVP, can be applied to the polar cap of 45 to 90°N. In Section 5.2, the snapshots of PV field in the quasi-static experiment (State A, B, and C) are qualitatively compared with those of the equilibrium and quasi-stationary states. The initial state A is interpreted as QSS 1, State B as QSS 3, and the final state C as the equilibrium state. In Section 5.3, quantitative comparisons are carried out by using the time series of the total PV Γ and energy E in the quasi-static experiment. We demonstrate that a transition occurs in the quasi-static experiment at about when the parameters of (a, Γ, E) enter the domain without existence of an appropriate quasi-stationary state. In Section 5.4, we examine the dynamical stability of QSS 1 (State A). As discussed in Section 4.3.2, a zonal-wavenumber-1 perturbation may destabilize QSS 1. We perform numerical experiments in which a wavenumber-1 perturbation is added to QSS 1 and demonstrate that these perturbations do not grow with time. Finally, in Summary (Section 5.5), we propose a new interpretation of S-SSWs, that is, the S-SSW can be qualitatively understood as the transition from QSS 1 in the direction of the

equilibrium state.

5.1 Preliminaries

Equilibrium statistical mechanics, including the QCVP, predicts a steady state realized after strong PV mixing, and applies only to an isolated system without dissipation nor forcing. More precisely, an inertial time scale (for instance, given by the eddy turnover time) needs to be much smaller than dissipation and forcing time scales. Before applying the QCVP to the quasi-static experiment, it is necessary to check the following three things. The PV field over the North Pole is not sensitive to (i) the viscosity coefficient ν, which controls the dissipation time scale, nor to (ii) the rate of change in the forcing amplitude $\mathrm{d}a/\mathrm{d}t$ [or Δt in (3.4)], which determines the forcing time scale. In addition, (iii) the PV field over the North Pole needs to be regarded as steady. We have already stated that the above three points are well satisfied in the quasi-static experiment, but here we examine them again.

Three more quasi-static experiments were conducted, where ten times ν and/or a half times Δt were used. According to (3.4), a smaller Δt means a faster increase in the forcing amplitude $a(t)$. Figure 5.1a shows the plots of the PV difference from the original quasi-static experiment. The PV difference normalized by the mean PV of the original experiment is almost always less than 15%, except around the two transitions discussed in Section 3.3.3 (at $a \sim 0.25$ and 0.65). Thus, the PV field before and after the transitions is not sensitive to the forcing nor dissipation time scales, which implies that both time scales are sufficiently longer than the turnover time of the flow over the North Pole.

We also confirm the steadiness of PV field in the original quasi-static experiment. Figure 5.1b shows the time series of the difference between the filtered and unfiltered (raw) PV fields, where the cutoff period is 100 days (top) or 300 days (bottom). The low frequency components

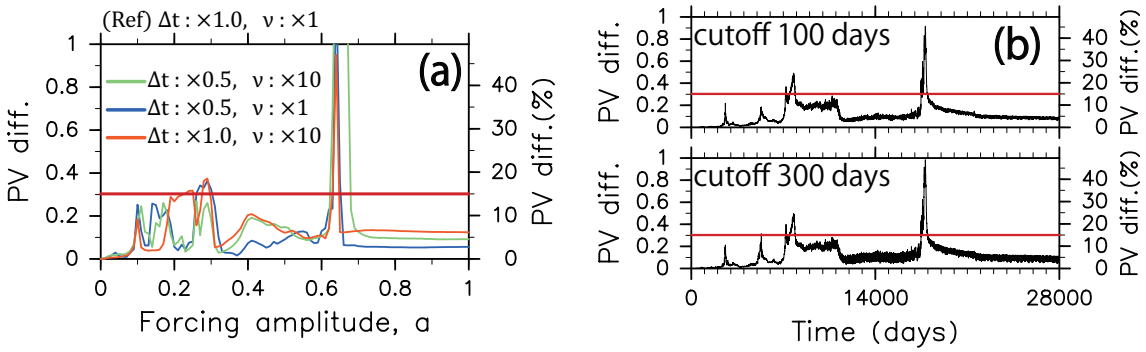

Figure 5.1: (a) Plots of the PV difference between q and q_{ref} against the forcing amplitude a in the quasi-static experiments. The PV in the original quasi-static experiment is regarded as the reference q_{ref}, where $\Delta t = 2.8 \times 10^4$ days and ν is chosen such that the e-folding time for the modes with the highest total wavenumber is 80 h. The reference q_{ref} is compared with the PV q from another experiment where ten times ν and/or a half times Δt are used. The PV difference is obtained in the following two steps: (i) At each grid point, q and q_{ref} are averaged over the time period such that $a - \Delta a/2 \le a(t) \le a + \Delta a/2$ for a given a, where $\Delta a = 10^{-2}$. (ii) The PV difference at each a is given by the area-weighted mean of $|q - q_{\mathrm{ref}}|$ over 45 to 90°N. All plots are insensitive to Δa. (b) Time series of the PV difference between q_{ref} and $q_{\mathrm{ref,LF}}$ in the original quasi-static experiment. The data step of q_{ref} is 5 days, and $q_{\mathrm{ref,LF}}$ is made by applying a low-pass filter to q_{ref} at each grid point with a cutoff period of (top) 100 days or (bottom) 300 days. The PV difference is given at each time by the area-weighted mean of $|q_{\mathrm{ref}} - q_{\mathrm{ref,LF}}|$ over 45 to 90°N. In (a) and (b), the lateral red lines represent 15%, where each right vertical axis (%) represents the PV difference divided by the time and area-weighted mean of $|q_{\mathrm{ref}}|$ (= 2.02).

are dominant, except around the two transitions ($t \sim 7000$ and 18000 days). Thus, the PV field before and after the transitions is regarded as steady at a time scale of 100 days or shorter.

A completely isolated system is practically meaningless because we cannot examine it with a measuring instrument. A system is generally considered to be isolated (or closed) when the state quickly becomes quasi-steady or the time scale of the evolution is sufficiently shorter than those of variations in external parameters such as total energy. In the quasi-static experiment, the time scales of the variations in the total PV Γ and energy E are controlled by that of the forcing amplitude a (i.e., Δt). The PV field is not sensitive to Δt and is regarded as steady at a time scale of 100 days or shorter. Thus, the polar cap of 45 to 90°N is considered as a closed domain at these time scales. In conclusion, the QCVP is applicable to this polar cap.

We make a few remarks on an influence of flows in the Southern Hemisphere and the application of equilibrium statistical mechanics. Polvani et al. (1995) investigated the surf zone (i.e., strong PV mixing region at middle latitudes) by using a spherical shallow-water model. They pointed out that a flow in the Southern Hemisphere may have a significant influence on a flow over the North Pole, especially when a (linear) relaxation is not included in the model. Furthermore, in barotropic fluid systems, an interaction between two vortices does not decay with distance, which supports the above result of Polvani et al. (1995). We conducted an experiment similar to the quasi-static experiment, but a large and strong vortex was set over the South Pole. We obtained similar results to those in Section 3.3.3 and the following sections, which implies that flows in the Southern Hemisphere are not critical to our quasi-static experiments.

We have shown above the validity of applying the QCVP to the north polar cap. The QCVP predicts a steady flow satisfying the linear q-ψ relation (4.5), whereas the more general Miller-Robert-Sommeria (MRS) theory predicts one satisfying a monotonic (not necessarily linear)

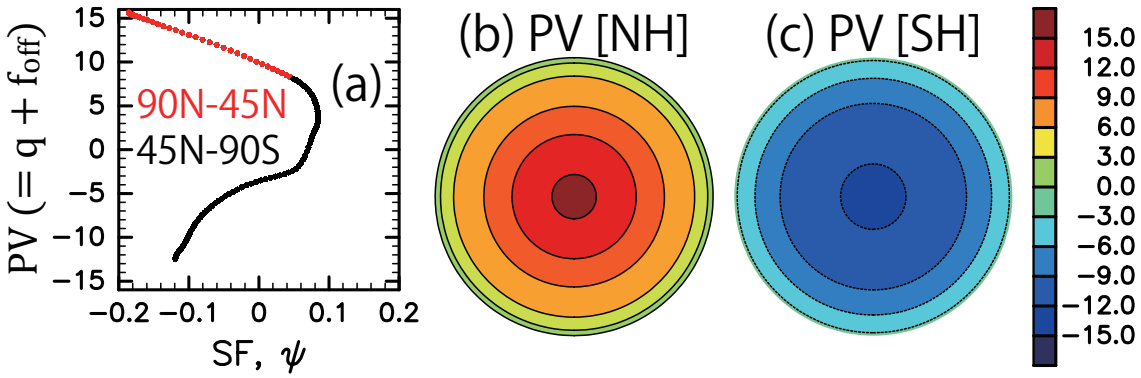

Figure 5.2: The initial state over the both hemispheres in the quasi-static experiment: (a) q-ψ scatter plot and PV fields over the (b) Northern and (c) Southern Hemispheres. The PV offset f_{off} in (3.2) is added to q, i.e., PV in (a) – (c) is equal to $q(\boldsymbol{x}) + f_{\text{off}}$.

q-ψ relation (Miller 1990; Robert 1991; Robert and Sommeria 1991). This means that the statistical mechanics is not applicable to flows not having monotonic q-ψ relations, even if the system satisfies the above three points (i) – (iii).

In the quasi-static experiment, the flow over 45 to 90°N always satisfies the q-ψ monotonicity well, which is approximated to be linear, as will be discussed in the next section. By contrast, the flow over the whole sphere does not always show monotonic q-ψ relations. Figure 5.2 shows the q-ψ scatter plot and PV fields of the initial state over the both hemispheres. Obviously, the q-ψ relation over the sphere is not monotonic, which means that not only the QCVP but also the MRS theory cannot be used to interpret this flow structure. It would be possible to make an initial state satisfying the q-ψ monotonicity, but we do not change the initial state because the initial state has been constructed from the real atmospheric data (JRA-55, see Section 3.3.1). After the polar-vortex breakdown, the q-ψ relation over the sphere becomes monotonic (but not linear). We focus here on only the north polar cap to make a consistent analysis from the initial to the final state in the quasi-static experiment.

5.2 Comparisons of instantaneous PV fields

In this section, we qualitatively compare the snapshots of PV field and demonstrate that State A is interpreted as QSS 1, State B as QSS 3, and State C as the equilibrium state. Figure 5.3 shows (a) the stream functions and (b) the PV fields in the quasi-static experiment. As typical snapshots, the 4000th-, 11000th-, and 28000th-day fields are shown as State A, B, and C, respectively.

State A is cyclonic and has a large-scale structure, which suggests that A is regarded as QSS 1 because QSS 1 has the largest structure among all quasi-stationary states (Section 4.3). Figure 5.3c shows the PV fields obtained by the theoretical calculations where the parameters of (a, Γ, E) from the quasi-static experiment are used. As expected, the PV magnitude and distribution of QSS 1 are quite similar to those of State A.

State B is cyclonic and its PV field is slightly elongated along the lateral direction, which implies that B can be interpreted as QSS 3 because QSS 3 has the largest structure among all the quasi-stationary states having laterally long PV fields. The PV magnitude of QSS 3 is comparable to that of State B. Both PV fields have qualitatively similar shapes, but the PV patch of QSS 3 is smaller than that of State B.

Only State C is anti-cyclonic, which indicates that C is considered as the equilibrium state because the equilibrium states are anti-cyclonic in the parameter range of the quasi-static experiment (Section 4.2). In fact, the magnitude and distribution of the equilibrium PV field are quite similar to those of State C.

There is also a good agreement on the q-ψ relation. Figure 5.3d shows the q-ψ scatter plots obtained from the quasi-static experiment. In each plot, the green line is given by the least squares fitting to the red dots, which represent the values from the grid points north of 45°N (the black dots show the values from the other points). There are well-defined q-ψ relations

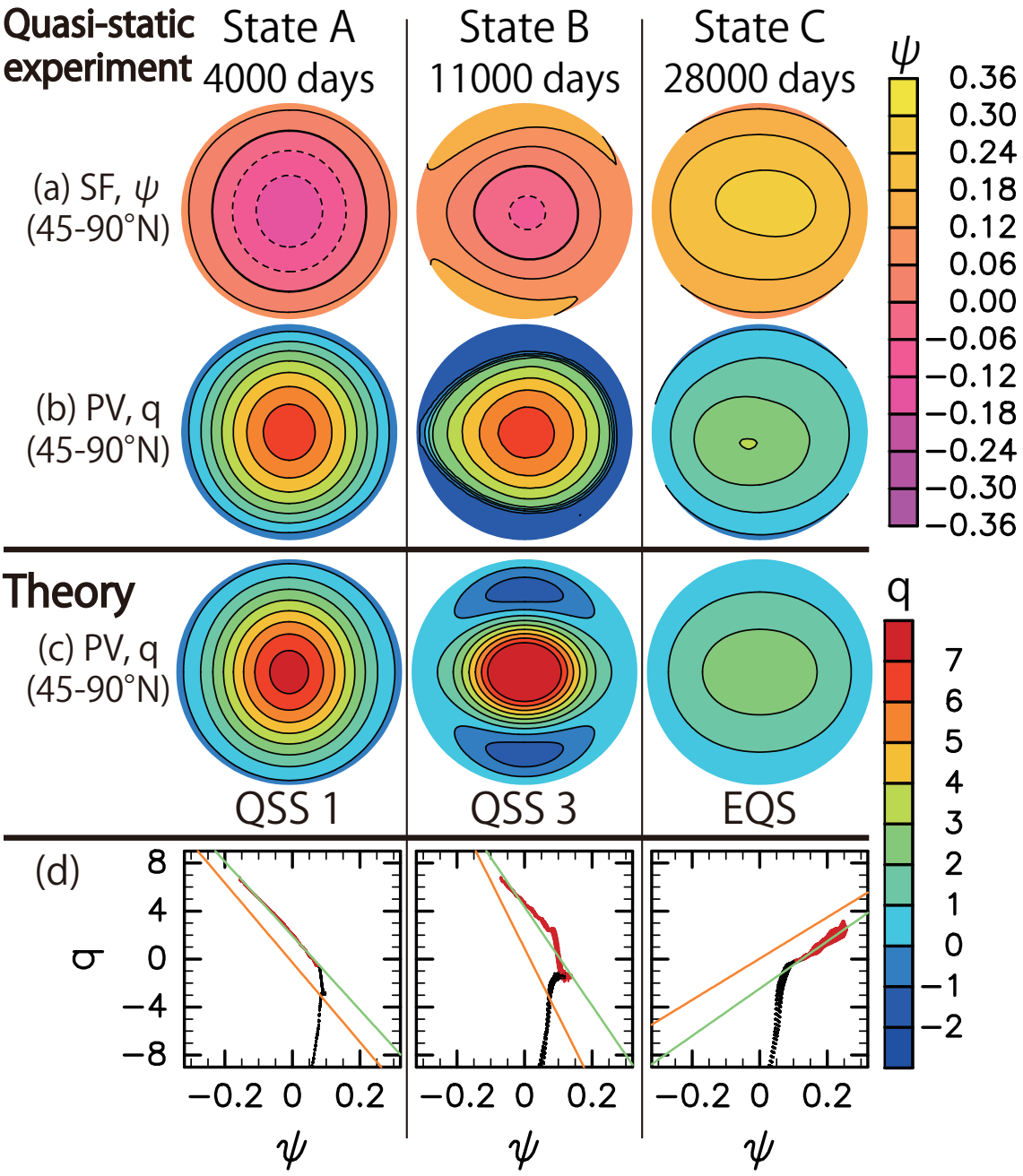

Figure 5.3: (a) PV fields and (b) stream functions (SFs) over 45 to 90°N obtained from the quasi-static experiment. As typical snapshots, the 4000th-, 11000th-, and 28000th-day fields are shown as State A, B, and C, respectively. (c) Theoretically calculated PV fields. Each field is obtained by giving the instantaneous parameters of (a, Γ, E) in the quasi-static experiment. (d) q-ψ scatter plots in the quasi-static experiment. The red dots represent the values from the grid points north of 45°N and the black ones represent those from the other points. The green line is given by the least squares fitting to the red dots. Each orange line represents the q-ψ relation (4.5) for the above theoretically calculated field.

over the North Pole and the linear fitting is valid as the first-order approximation. The QCVP gives the linear q-ψ relation, namely $q = b\psi - c$ in (4.5), which characterizes the equilibrium and quasi-stationary states. The theoretically calculated linear relations are also shown in Fig. 5.3d by the orange lines. The inclinations b given by the theory agree well with those of the quasi-static experiment, but there is a discrepancy in the offsets c. This discrepancy is likely because c is strongly dependent on the latitude at the polar-cap boundary. It would be possible to define the boundary of polar cap at each time such that a theoretical value of c is close to a value from the quasi-static experiment. However, such treatment is not necessary for the qualitative comparisons here.

Therefore, we have obtained the following expectation: The state changes observed in the quasi-static experiment are understood as

$$\text{QSS 1 (State A)} \rightarrow \text{ QSS 3 (State B)} \rightarrow \text{ Equilibrium state (State C).}$$

The polar vortex breaks down without splitting during the transition from B to C. By contrast with the quasi-static experiment, when the forcing amplitude is increased over one week (Section 3.3.2), State B does not appear and the polar vortex collapses while splitting into the two vortices during the transition from A to C.

5.3 Comparisons of timings of transitions

The discussions in the previous section are based on the instantaneous PV fields in the quasi-static experiment. In this section, using the time series of the total PV Γ and energy E in the quasi-static experiment, we demonstrate that the timings of the two transitions in the quasi-static experiment are consistent with the theoretical predictions. This result supports the above expectation of the state changes. We first show that a transition timing given by the theoretical calculations within 45 to 90°N is not consistent with that in the quasi-static experiment. This is

due to that transition timings given by the theory are sensitive to the choice of polar caps. We properly determine a polar cap on the basis of the position of the surf zone and compare the transition timings again.

In Section 4.4, we have discussed that a transition may occur when the parameters of (a, Γ, E) enter the domain without existence of a quasi-stationary state. Due to the sufficiently slow variation in the forcing h_{QSE}, the flow field is nearly steady and the QCVP is almost always applicable to the quasi-static experiment. Thus, the theory can be used to interpret timings of transition.

The transition from State A to B is first investigated. The minimum energy for existence of any quasi-stationary state can be theoretically calculated when the forcing amplitude a and the total PV Γ are given, as seen in Fig. 4.4. Note that the QCVP cannot predict the variation in Γ, which is externally given by solving the QG barotropic equations. Since we expect that the transition from A to B is considered as that from QSS 1 to 3, the minimum energy for QSS 1 is calculated at each time by giving the instantaneous values of a and Γ in the quasi-static experiment. Figure 5.4a compares the time series of the minimum energy for QSS 1 (orange) with those of the energy in the quasi-static experiment (black). The middle and bottom panels show the time series of Γ and S in the quasi-static experiment, respectively. Before reaching the entropy minimum, the energy in the experiment becomes lower than the minimum energy for QSS 1, which suggests that a transition occurs at about that time. In fact, associated with the decrease in the entropy, the flow field changes from State A to B: The PV field changes from a vertically to a laterally elongated shape, as seen in the time series of the major-axis angle of the equivalent ellipse (Fig. 3.6a). These results support that State A before the first transition is regarded as QSS 1.

There is another reason for focusing on the minimum of the entropy, that is, QSS 1 is virtu-

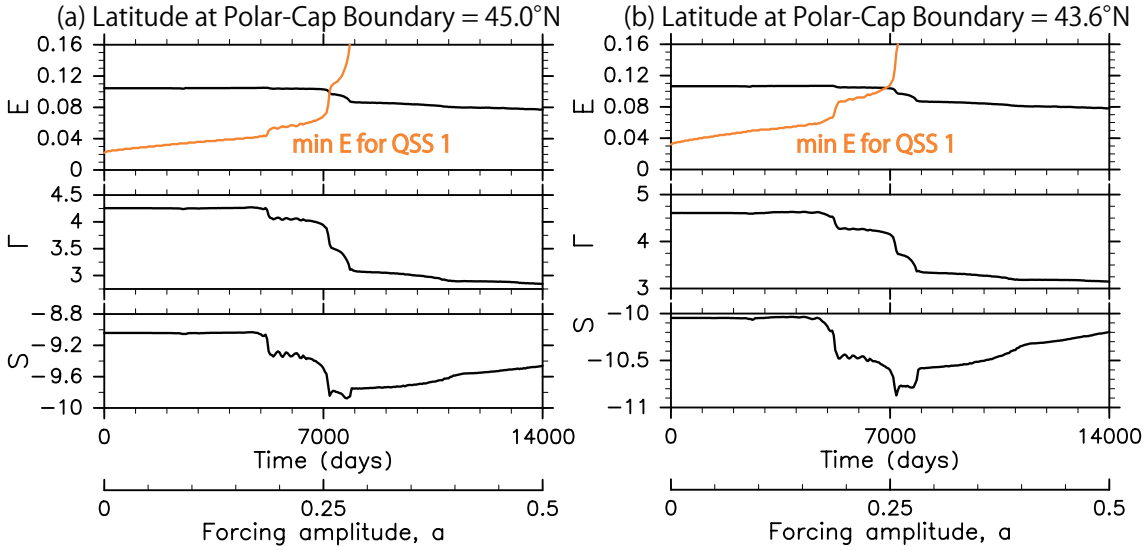

Figure 5.4: Time series obtained from the quasi-static experiment: (top) the total energy E, (middle) the total PV Γ, and (bottom) the entropy S. The orange curve in each top panel shows the minimum energy for QSS 1, which is theoretically calculated by giving the instantaneous values of a and Γ in the quasi-static experiment. The latitude at the polar-cap boundary is (a) 45.0°N and (b) 43.6°N.

ally a local maximum of the entropy (Section 4.3.2). The only way to increase the entropy of QSS 1 is to add a perturbation including the gravest wavenumber-1 modes. In the quasi-static experiment, the initial PV is axisymmetric (Section 3.3.1) and the bottom forcing h_{QSE} in (3.3) consists of only the wavenumber-2 component. This means that a wavenumber-1 perturbation is never produced in the QG barotropic model, except for a noise from numerical errors. Assuming that such a noise is not critical, we can regard QSS 1 as the unique local maximum of the entropy. In this case, the entropy is decreased in any transition from QSS 1 to another quasi-stationary state, and the minimum entropy implies that the transition is completed. Even when the initial PV includes wavenumber-1 components, similar results are obtained (Appendix B). Moreover, in the next section, we will investigate the dynamical stability of QSS 1 (State A) by directly adding a wavenumber-1 perturbation to its PV field and examining the time evolution of the perturbation. The results indicate that small- but finite-amplitude wavenumber-1 perturbations do not grow with time. These results suggest that the wavenumber-1 components do

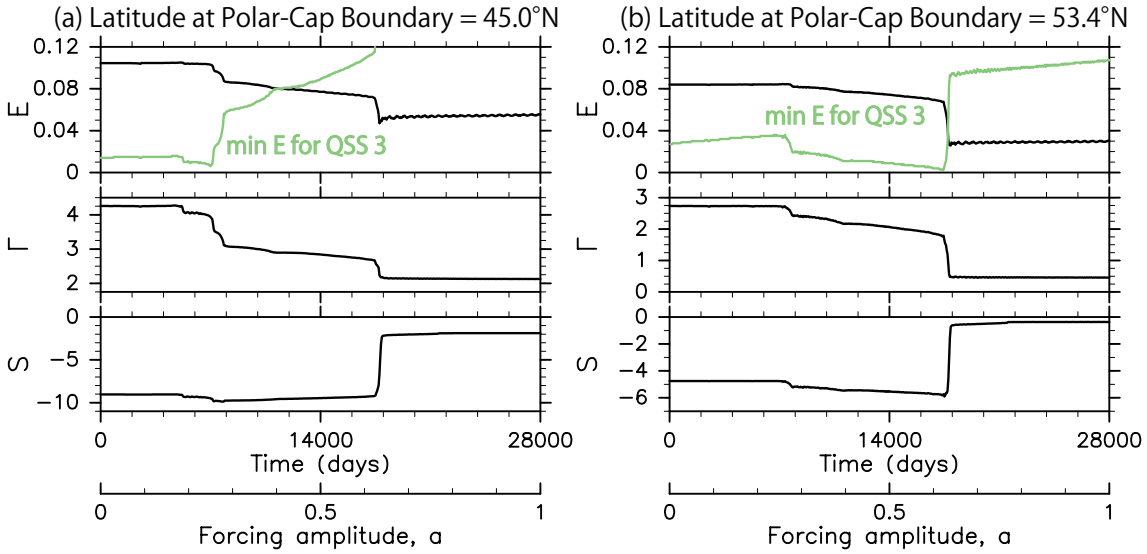

Figure 5.5: Time series obtained from the quasi-static experiment: (top) the total energy E, (middle) the total PV Γ, and (bottom) the entropy S. The green curve in each top panel shows the minimum energy for QSS 3, which is theoretically calculated by giving the instantaneous values of a and Γ in the quasi-static experiment. The latitude at the polar-cap boundary is (a) 45.0°N and (b) 53.4°N.

not have much effect on the emergence and persistence of QSS 1, even though the nonlinear stability of QSS 1 against these perturbations is not theoretically assured.

The transition from State B to C is examined in a similar way. Since we expect that this transition is considered as that from QSS 3 to the equilibrium state, the minimum energy for QSS 3 is theoretically calculated and is compared with the energy of the quasi-static experiment. Figure 5.5a shows the results, like Fig. 5.4a. The transition timing given by the theory is denoted by the intersection of the time series of the energy (black) with those of the minimum energy for QSS 3 (green). Obviously, the predicted timing is too early compared with that in the quasi-static experiment, which is characterized by the abrupt increase in the entropy S ($t \sim 18000$ days).

5.3.1 Comparisons under an appropriate choice of polar caps

We have so far focused on the polar cap of 45 to 90°N. The above comparisons of the transition timings are quantitative and dependent on the size of the polar cap. In this subsection, we properly determine a polar cap for the QCVP and then compare the transition timings again. We first discuss which latitude should be regarded as the polar-cap boundary.

The theoretical calculations are performed within the disk obtained by projecting the polar cap onto the plane. By contrast, the QG barotropic model on the sphere has been used to conduct the quasi-static experiment. Thus, a discrepancy between the theoretical calculations and the simulation results will be large, as the polar cap becomes larger, due to the difference between the flat and spherical geometries. This suggests that the polar cap should be as small as possible.

The theory describes a flow field having the linear q-ψ relation: $q = b\psi - c$ in (4.5). If q is nearly constant over some region, only $b = 0$ is possible (i.e., $q = c = \text{const}$) because ψ is generally not constant even in such a region. The region with nearly constant PV is well-known as the surf zone in the stratosphere (e.g., McIntyre and Palmer 1983, 1984). The dynamics of the surf zone can be described with a one-layer model (e.g., Polvani et al. 1995). Thus, we define the polar-cap boundary as the north edge of the surf zone.

To determine the surf-zone edges, we examine the zonal-mean PV $\overline{q}$ and its meridional derivative $\partial\overline{q}/\partial\varphi$. In the QG barotropic model, the region with nearly constant $\overline{q}$ appears at middle latitudes. The north and south edges of the surf zone are defined in the following two steps: (i) The latitude with the minimum $\partial\overline{q}/\partial\varphi$ is determined and denoted by $\varphi_{\min}$; (ii) The north (south) edge of the surf zone $\varphi_{\text{surf,N}}$ ($\varphi_{\text{surf,S}}$) is defined as the latitude north (south) of $\varphi_{\min}$ at which $\partial\overline{q}/\partial\varphi$ first exceeds 7.0. The value of 7.0 is arbitrary, but the following results are insensitive to this value. Figure 5.6a shows the time series of $\varphi_{\text{surf,N}}$, $\varphi_{\text{surf,S}}$, and major-axis

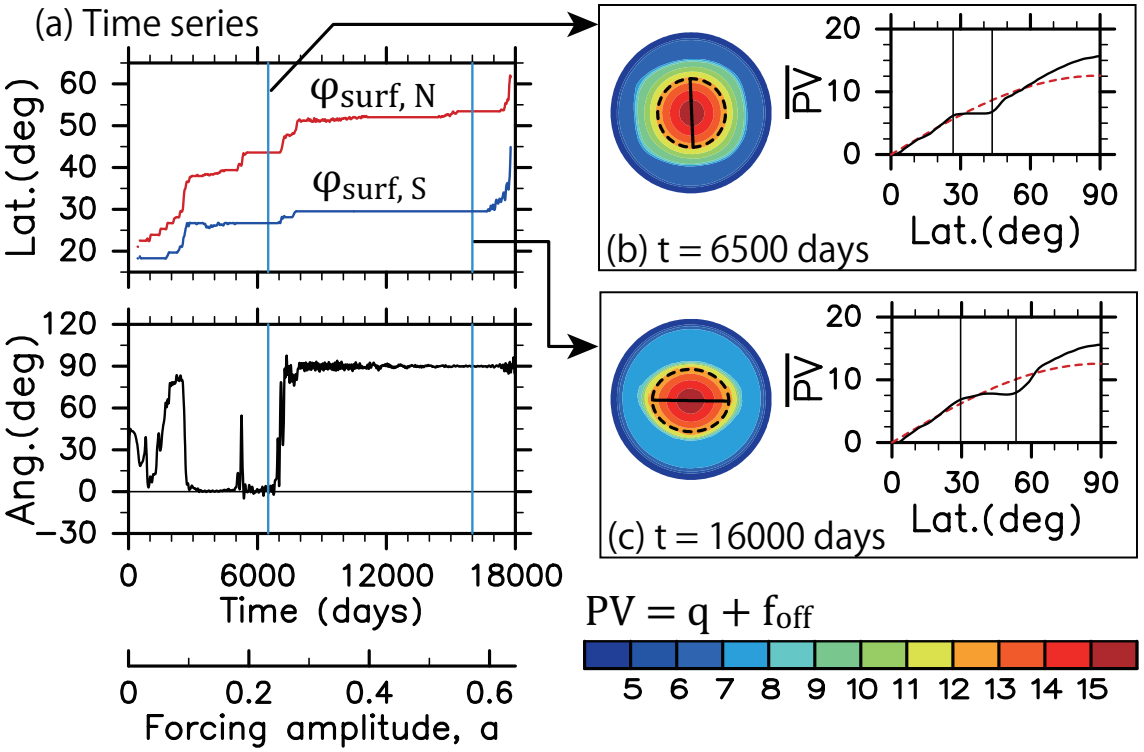

Figure 5.6: (a) Time series obtained from the quasi-static experiment: (top) the latitudes at the north and south edges of the surf zone, $\varphi_{\mathrm{surf,N}}$ and $\varphi_{\mathrm{surf,S}}$, respectively, and (bottom) the major-axis angle of the equivalent ellipse. See text for the definitions of $\varphi_{\mathrm{surf,N}}$ and $\varphi_{\mathrm{surf,S}}$. (b) and (c) PV fields over the Northern Hemisphere and plots of zonal-mean PV against latitude on (b) t = 6500 days and (c) 16000 days. The red dashed curves represent the Coriolis parameter $f(\varphi) \equiv 2\Omega \sin\varphi$. The vertical lines represent $\varphi_{\mathrm{surf,N}}$ and $\varphi_{\mathrm{surf,S}}$. In (b) and (c), the PV offset f_{off} in (3.2) is added to q: PV $\equiv q(\boldsymbol{x}) + f_{\mathrm{off}}$.

angle of the equivalent ellipse. These time series are ended at t = 18000 days because of the polar-vortex breakdown. Figures 5.6b and 5.6c show the PV fields and the distributions of zonal-mean PV, where the vertical lines represent $\varphi_{\mathrm{surf,N}}$ and $\varphi_{\mathrm{surf,S}}$. In both figures, the above definition of the surf-zone edges well captures the regions with nearly constant PV. The surf zone becomes wider, as the forcing amplitude a is increased (Fig. 5.6a). A similar result was reported by Polvani et al. (1995).

The first transition from State A to B occurs at about t = 7000, i.e., when the major-axis angle is changed from about 0 to 90° (Fig. 5.6a). The value of $\varphi_{\mathrm{surf,N}}$ gradually increases and is equal to about 43.6°N just before the transition. The same calculations as in Fig. 5.4a are

performed for the polar cap of 43.6 to 90°N. Figure 5.4b shows the obtained results. In these calculations, the surface integrals of E, Γ, and S are taken over 43.6 to 90°N, and the offset of PV [$f_{\rm off}$ in (3.2)] is given by the Coriolis parameter at 43.6 °N. The theoretically calculated timing of the transition is just before the entropy minimum, like in Fig. 5.4a.

The second transition from State B to C occurs at about $t = 18000$ days. Before the transition, $\varphi_{\rm surf,N}$ is nearly constant at 53.4°N. The same calculations as in Fig. 5.5a are performed for the polar cap of 53.4 to 90°N, and the obtained results are shown in Fig. 5.5b. In this case, the theory gives the transition timing which is nearly the same as that in the quasi-static experiment.

In summary, when the polar cap is determined by the north edge of the surf zone, the timings of the two transitions given by the QCVP are close to those in the quasi-static experiment. In the previous subsection, the theoretically calculated timing of the second transition was too early, compared with the actual timing in the quasi-static experiment. This discrepancy is likely due to that the size of the polar cap is too large and is not appropriate for the second transition.

5.4 Dynamical stability of QSS 1

The initial state A is considered as QSS 1, which may be destabilized by a zonal-wavenumber-1 perturbation (Section 4.3.2). We investigate here the dynamical stability of QSS 1 by adding a wavenumber-1 perturbation and examining its time evolution. The initial PV is made by running the QG barotropic model for 5000 days from the 3000th-day flow field, where the forcing amplitude $a(t)$ is fixed at 0.11. The obtained field is regarded as QSS 1, like the 4000th-day field in Fig. 3.6b, but its fluctuation is much smaller than that of 4000th-day field. Thus, this initial state is almost steady with high accuracy. The following PV perturba-

tion[1] is then added to the initial PV and the numerical integration is performed for 5000 days more:

$$\tilde{\delta}q \equiv \tilde{\alpha} \times q_{\max} \exp\left[-\frac{1}{2}\left(\frac{\varphi - 67.5^\circ\mathrm{N}}{7.5^\circ}\right)^2\right] \times \{\sin\lambda \text{ or } \cos\lambda\}, \tag{5.1}$$

where $q_{\max}$ is the PV maximum in the initial state (= 6.85) and the amplitude of $\tilde{\delta}q$ is specified by $\tilde{\alpha}$. This perturbation may be similar to the gravest zonal-wavenumber-1 Laplacian eigenmode within the polar cap of 45 to 90°N. We vary $\tilde{\alpha}$ from 0.01 to 0.1 in increments of 0.01 and perform the 20 experiments for both cases of sin and cos in (5.1).

The above small- but finite-amplitude perturbation obeys the nonlinear QG equations (3.1) and (3.2), and its magnitude is measured by the following two norms, which are common to nonlinear stability theories (e.g., Swaters 1999):

$$\| \tilde{\delta}q(t) \|_{\mathrm{E}}^{\ 2} \equiv \frac{1}{2}\int \{\boldsymbol{\nabla}[\psi(\boldsymbol{x},t) - \psi_0(\boldsymbol{x})]\}^2 \ \mathrm{d}A, \tag{5.2}$$

and

$$\| \tilde{\delta}q(t) \|_{\mathrm{S}}^{\ 2} \equiv \frac{1}{2}\int [q(\boldsymbol{x},t) - q_0(\boldsymbol{x})]^2 \ \mathrm{d}A, \tag{5.3}$$

where ψ_0 and q_0 are the initial stream function and PV without including the perturbation, $\| \tilde{\delta}q \|_{\mathrm{E}}$ is the energy norm, $\| \tilde{\delta}q \|_{\mathrm{S}}$ is the enstrophy norm, and the above integrations are taken over 45 to 90°N.

The perturbation does not grow with time in all the experiments. Figure 5.7 shows the result of the experiment with $\tilde{\alpha} = 0.1$, where $\sin\lambda$ is chosen in (5.1). In Fig. 5.7a, the label ALL means that all zonal-wave-number components are included in the norms, and the label WN1 means that only the wavenumber-1 components are included (i.e., ψ_0 and q_0 are zero). All norms rapidly decrease in about a hundred days, where $\| \tilde{\delta}q(0) \|_{\mathrm{E}}^{\ 2} = 3.5 \times 10^{-3}$ and $\| \tilde{\delta}q(0) \|_{\mathrm{S}}^{\ 2} = 6.8 \times 10^{-2}$ (≈ 0.07). Note that the norms composed only of the wavenumber-1

[1]We also examined the evolution of a slightly different perturbation, whose standard deviation was 11.25° instead of 7.5° in (5.1). This perturbation rapidly decreased and then oscillated, like in Fig. 5.7, when $\tilde{\alpha} = 0.1$.

components are the same as those including all components at $t = 0$. After the initial decay period, the perturbation is gradually decayed likely due to the numerical viscosity, while its norm fluctuates with time (Fig. 5.7a). The time scales of these fluctuations depend on the cutoff period of the low-pass filter, but similar time series were obtained when different cutoff periods were used. The PV field is always vertically elongated, like that of QSS 1 (Figs. 5.7a and 5.7b).

These results suggest that a state slightly deviated from QSS 1 returns or persists there for a long time, i.e., QSS 1 is nonlinearly stable in the sense of Lyapunov (Lyapunov stable), though the nonlinear stability of QSS 1 is not theoretically assured. A linear stability analysis will still be useful. Since QSS 1 is an exact steady solution on the disk (unlike on the sphere), its linear stability can be investigated by solving the eigenvalue equation, which is obtained from the linearized QG equation.

5.5 Summary

We have interpreted the results of the quasi-static experiment in terms of the statistical-mechanics theory (i.e., the QCVP), and demonstrated that State A is regarded as QSS 1, State B as QSS 3, and State C as the equilibrium state. Thus, the state changes observed in the quasi-static experiment are understood as QSS 1 (State A) $\rightarrow$ QSS 3 (State B) $\rightarrow$ Equilibrium state (State C).

In contrast to the quasi-static experiment, when the forcing time scale is one week, the polar vortex splits and breaks down during the transition from QSS 1 to the equilibrium state, in which State B does not appear (Section 3.3.2). Although the forcing time scale of one week is relevant to S-SSWs (Sjoberg and Birner 2012), the comparisons between the statistical-mechanics theory and the quasi-static experiment have revealed that the initial state is consid-

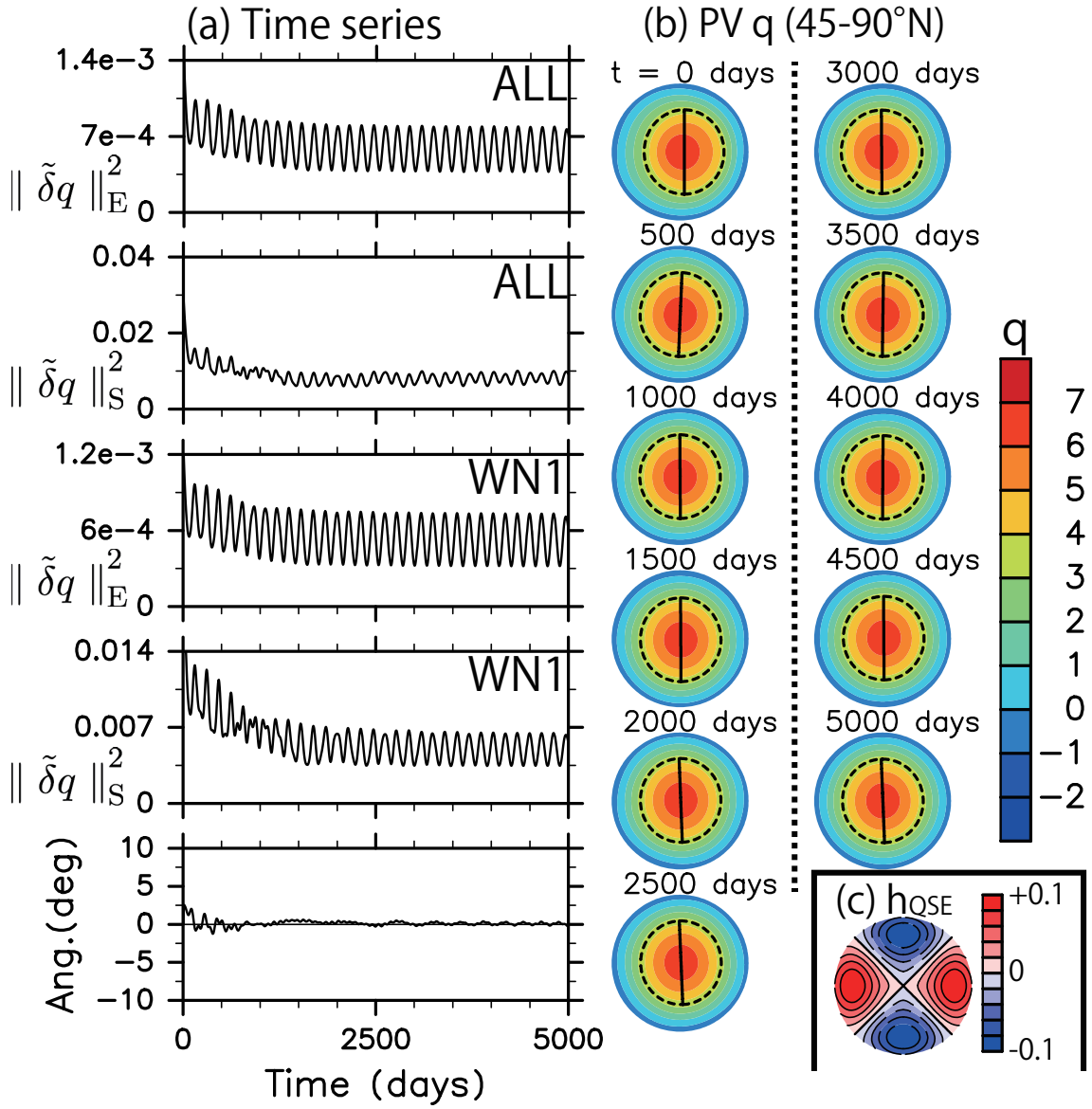

Figure 5.7: Results of the numerical experiment where the zonal-wavenumber-1 perturbation (5.1) with $\tilde{\alpha} = 0.1$ is added to the initial PV field regarded as QSS 1. (a) Time series of the norms of the perturbation and major-axis angle of the equivalent ellipse for PV, where $\| \tilde{\delta q} \|_{\mathrm{E}}$ is defined in (5.2) and $\| \tilde{\delta q} \|_{\mathrm{S}}$ in (5.3). Label ALL means that all zonal-wavenumber components are included in the norms, and WN1 means that only the wavenumber-1 components are included. A low-pass filter with a 100-day cutoff period was applied to all time series. (b) Evolution of the PV field over 45 to 90°N. The equivalent ellipses are drawn by the dashed curves and their major axes by the solid lines. (c) Effective bottom forcing h_{QSE} with $a = 0.11$ over 45 to 90°N.

ered as QSS 1, which is virtually a local maximum of the entropy (Section 4.3.2). Although the nonlinear stability of QSS 1 is not theoretically assured, the numerical experiments have suggested that QSS 1 is Lyapunov stable (i.e., a perturbation does not grow with time).

Therefore, we propose a new understanding of S-SSWs: The S-SSW can be qualitatively understood as the transition from QSS 1 in the direction of the equilibrium state (see Fig. 1.4). The state with the vortex splitting is observed during the transition, which is an unsteady non-equilibrium state. Without any external forcing such as radiative cooling, the anti-cyclonic equilibrium sate would be realized sufficiently after an S-SSW.

A typical phenomenon understood in a similar way is the transition from supercooled water to ice. Supercooled water suddenly changes into ice when some shock is given. The state of ice is the entropy maximum, but the state of supercooled water is a local maximum of the entropy. This kind of transition is occasionally called the zeroth-order phase transition. According to our interpretation, supercooled water corresponds to the state before an S-SSW (i.e., QSS 1), in which the cyclonic polar vortex exists over the North Pole; Some shock corresponds to the effects of a Rossby-wave amplification; Ice corresponds to the state sufficiently after an S-SSW, in which the flow over the North Pole is anti-cyclonic. The only difference is that QSS 1 is virtually a local maximum of the entropy, but supercooled water is exactly a local maximum. The concept of entropy connects the S-SSW to the transition from supercooled water to ice, and reveals the analogy between both phenomena.

Chapter 6

Discussions

The discussions so far do not take into account radiative cooling. The dynamics of SSWs has often been investigated with a mechanical model not including a radiative relaxation because of the time scale separation between the inertial and relaxation time scales. However, radiative cooling is vital for the re-formation of the polar vortex after an SSW (e.g., Rong and Waugh 2004; Scott and Polvani 2006), and cannot be ignored when we discuss the evolution over a long period [$\geq O(1$ month)]. An equilibrium state will appear after strong PV mixing, which may take a much longer time than a radiative relaxation time.

In Section 6.1, we discuss a transition in the QG barotropic model including a linear relaxation. The radiative-relaxation time scale in the stratosphere is 10 days (Andrews et al. 1987; Newman and Rosenfield 1997), whereas the transition time scale toward the equilibrium state is 100 days. This result implies that the (anti-cyclonic) equilibrium state is very unlikely to be observed in the stratosphere. However, the axisymmetric flow often becomes anti-cyclonic just after an S-SSW. We compare the evolution of the zonal-mean zonal winds in JRA-55 and the QG model, and discuss that the state of the stratosphere may temporarily approach the equilibrium state after an S-SSW.

In Section 6.2, our understanding of S-SSWs is compared with the previous studies, which also argue that SSWs, including S-SSWs, are interpreted as some transition. An important

feature of our understanding is a view of potential, which is given by the negative of the entropy. This view may extend our results to the non-equilibrium statistical mechanics. According to the view of potential, a transition (i.e., S-SSW) occurs when the system gets over a potential barrier. Associated with this view, we discuss the preconditioning of the polar vortex and the frequency of S-SSWs in the Northern and Southern Hemispheres.

6.1 Effects of radiative cooling

We first give a perspective on the effects of radiative cooling in the re-formation processes of the polar vortex. The polar vortex is quite weak after an S-SSW. The radiative cooling over the North Pole supplies energy and PV to the polar stratosphere, and re-forms the strong polar vortex. From a view point of the entropy, the radiative cooling has two effects: (i) the recovery of saddle points on the entropy surface and (ii) the gradual change toward a quasi-stationary state. The S-SSW makes the total PV Γ and energy E so small that some saddle points of the entropy (e.g., QSS 1) do not exist (see Fig. 4.4). The energy and PV supply by the radiative cooling recovers these saddle points.

The statistical mechanics suggests that there are many possible states at fixed Γ and E. For instance, not only the equilibrium state but also QSS 1 may be possible. The most probable state among all possible ones, including unsteady turbulent states, is the equilibrium state, which is steady and anti-cyclonic in the realistic parameter range (Section 4.2). However, such a state is not typical of the winter stratosphere. There are two reasons for that. The first reason is due to the radiative cooling. The strong radiative cooling over the North Pole makes the winter stratosphere a cyclonic state, even though the equilibrium state is anti-cyclonic. In addition, the spatial distribution of the radiative equilibrium temperature will select which quasi-stationary state is typical of the winter stratosphere. After an S-SSW, the radiative cooling will change

the state of the stratosphere to such a quasi-stationary state [the above point (ii)]. The strong candidate may be QSS 1 because of its largest spatial structure. The second reason is due to the existence of various time-dependent disturbances such as Rossby and inertia-gravity waves. These disturbances will fluctuate the state of the stratosphere among a few possible quasi-stationary states (e.g., QSS 1 and 3). This kind of fluctuation may be modeled as a Langevin system (Section 6.2.2).

A relation between the spatial structures of radiative equilibrium temperature and quasi-stationary state may be important to interpret the mean state of the stratosphere with equilibrium and non-equilibrium statistical mechanics. Recent studies suggest that a fluid system approaches the nearest saddle point (or local maximum) of the entropy and persists there for a long time, if the system is not affected by an external forcing such as radiative cooling (e.g., Majda and Wang 2006; Naso et al. 2010). Our results are consist with this dynamical description. The initial condition in the quasi-static experiment has been made from JRA-55 (Section 3.3.1), which is considered as a balanced state between the radiative forcing and the eddy diffusion. This initial state approaches QSS 1 when the linear relaxation is not included in the QG barotropic model (Sections 3.3.3, 5.4, and Appendix B). The spatial structure of the radiative equilibrium temperature is large (e.g., Andrews et al. 1987), which will make the initial balanced state close to QSS 1. Such a balanced (steady) state slightly deviated from QSS 1 may be theoretically analyzed with a linear response theory in non-equilibrium statistical mechanics (e.g., Kubo et al. 1998).

6.1.1 Numerical experiments including a linear relaxation

An influence of the radiative cooling on transitions is investigated by using the spherical QG barotropic model including a linear relaxation

$$\frac{\partial q}{\partial t} + \boldsymbol{v} \cdot \boldsymbol{\nabla} q = -\nu \Delta^{10} q - \left(\frac{q - q_{\mathrm{ini}}}{\tau_{\mathrm{rlx}}} \right), \tag{6.1}$$

and

$$q(\boldsymbol{x}, t) \equiv \Delta\psi(\boldsymbol{x}, t) + \underbrace{2\Omega \sin\varphi}_{f(\boldsymbol{x})} + 2\Omega \sin\varphi \; h(\boldsymbol{x}, t)/H - \underbrace{2\Omega \sin\varphi_{\mathrm{off}}}_{f_{\mathrm{off}}}, \tag{6.2}$$

where q_{ini} is the initial PV and (6.2) is the same as the definition of the PV q used so far. The linear relaxation in (6.1) corresponds to the Newtonian cooling, i.e., the first-order approximation of radiative cooling to temperature (e.g., Andrews et al. 1987). The relaxation time becomes shorter at a higher altitude, which is on average about 28 days at 100 hPa ($\sim$ 15 km) and 4 days at 1 hPa ($\sim$ 45 km) (Newman and Rosenfield 1997). We examine here the three cases of $\tau_{\mathrm{rlx}} = 10$, 20, and 30 days. The initial PV is given by the axisymmetric component of the barotropic, climatological, absolute vorticity $\Delta\psi + f$, as in all experiments of Section 3.3. Similar one-layer models have been employed by the previous studies on SSWs (e.g., Polvani and Waugh 2004; Scott 2016), where $\tau_{\mathrm{rlx}} = 10$ or 20 days is often used.

The bottom forcing is given by

$$h_{\mathrm{R}} \equiv a_{\mathrm{R}}(t) \times h_0 \; \cos[2(\lambda - \lambda_0)] \; \exp\left[-\frac{1}{2} \left(\frac{\varphi - \varphi_0}{\Delta\varphi} \right)^2 \right], \tag{6.3}$$

where

$$a_{\mathrm{R}}(t) \equiv \begin{cases} 0 & (t < 0), \\ a_{\max} \times \frac{t}{\Delta t_1} & (0 \le t < \Delta t_1), \\ a_{\max} & (\Delta t_1 \le t < \Delta t_1 + \Delta t_2), \\ a_{\max} + (a_{\max} - a_{\min}) \frac{\Delta t_1 + \Delta t_2 - t}{\Delta t_3} & (\Delta t_1 + \Delta t_2 \le t < \Delta t_1 + \Delta t_2 + \Delta t_3), \\ a_{\min} & (\Delta t_1 + \Delta t_2 + \Delta t_3 \le t). \end{cases} \tag{6.4}$$

All parameters, except for the four new parameters ($a_{\min}$, Δt_1, Δt_2, and Δt_3), are the same as those of h_{QSE} in Section 3.3.2 (see Fig. 3.3). The new parameters are given as $a_{\min} = 0.7$,

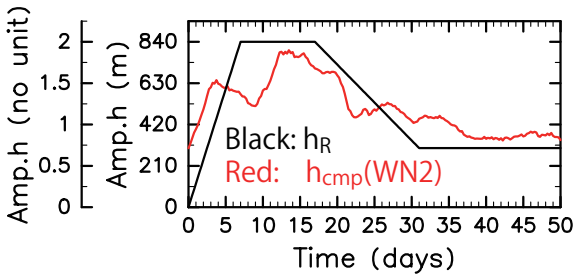

Figure 6.1: Time series of the forcing amplitudes: (black) the amplitude of h_R in (6.3) [i.e., a_R in (6.4)] and (red) the amplitude of the zonal-wavenumber-2 h_{cmp} made from JRA-55. Both time series are the same as those in Fig. 3.4a until $t = \Delta t_1 + \Delta t_2$ (= 17 days). For comparison, the onset time is shifted to t = 10 days, like in Fig. 3.4a.

Δt_1 = 7 days, Δt_2 = 10 days, and Δt_3 = 14 days. Figure 6.1 compares the time series of a_R with those of the amplitude of the wavenumber-2 component of h_{cmp}, which is made by the composite analysis of JRA-55. The simple form of a_R well approximates the variation in the amplitude of the wavenumber-2 h_{cmp}.

To estimate the transition time, we first conduct a simulation without the linear relaxation ($\tau_{rlx} = \infty$). The model configuration here is the same as that of the experiment in Section 3.3.2 until $t = \Delta t_1 + \Delta t_2$ (= 17 days), and the same vortex splitting is observed as in Fig. 3.4b. The evolution over a long period is shown in Fig. 6.2. Compared with Fig. 3.5, the entropy S becomes nearly constant and a quasi-steady (anti-cyclonic) flow appears at about t = 200 days. Thus, the system reaches the quasi-steady state much earlier than in the experiment of Section 3.3.2. This result is attributed to the difference in the forcing amplitude after the vortex splitting: a is fixed to a_{max} (= 2) in Section 3.3.2, but to a_{min} (= 0.7) here, which leads to a larger velocity and a more rapid evolution. The anti-cyclonic flow observed after t = 200 days is considered as the equilibrium state, and the transition time is estimated at about 200 days.

This transition time is one-order larger than the radiative relaxation time (~ 10 days), which suggests that the equilibrium state is not observed in the QG model. To confirm this, we conduct the three experiments including the linear relaxation (τ_{rlx} = 10, 20, and 30 days). In all cases,

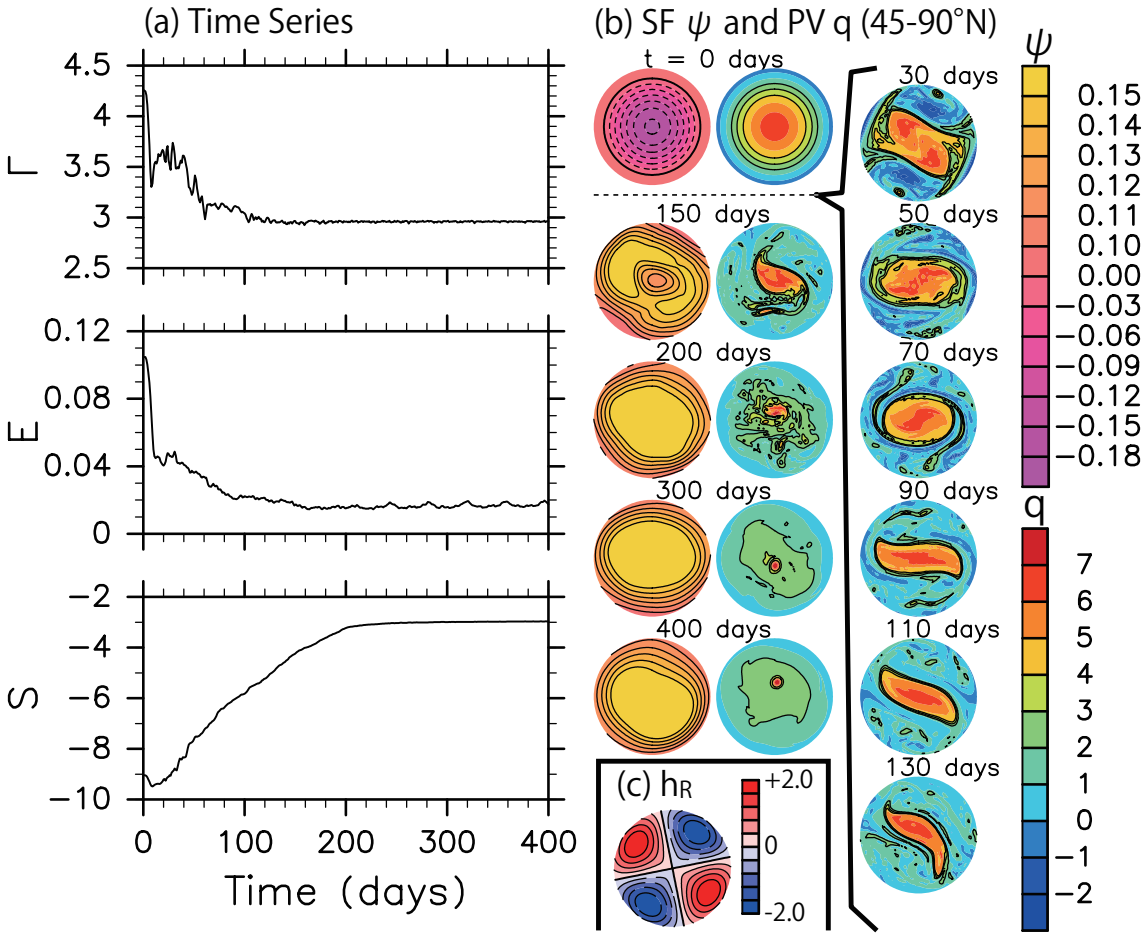

Figure 6.2: Results from the QG experiment with $\tau_{\mathrm{rlx}} = \infty$ (no relaxation): (a) time series of the total PV Γ, the total energy E, and the entropy S; (b) the evolution of stream function (SF) ψ and PV q over 45 to 90°N; and (c) effective bottom forcing h_{R} over 45 to 90°N defined by (6.3) and (6.4) at $t = \Delta t_1 + \Delta t_2$.

vortex splittings similar to that in Fig. 3.4b are observed, but quasi-steady anti-cyclonic flows are not. The polar vortex is re-formed before the system reaches the equilibrium state.

In the case of $\tau_{\mathrm{rlx}} = 10$ days, a quasi-steady *cyclonic* state appears after the vortex splitting, as shown in Fig. 6.3c, which likely results from the balance between the linear relaxation and the form stress due to the bottom forcing. In the cases of $\tau_{\mathrm{rlx}} = 20$ and 30 days, vacillating states appear after the vortex splittings. Figure 6.3 shows (a) the time series of Γ, E, and S and (b) the evolution of PV q, when $\tau_{\mathrm{rlx}} = 30$ days. The vacillation with $\tau_{\mathrm{rlx}} = 20$ days is similar, but its amplitude is smaller. The three time series in Fig. 6.3a suggest that the time scale of the vacillation is about 150 days. This vacillation may be interpreted as a fluctuation (or a limit cycle) around an unstable steady state that corresponds to the state in Fig. 6.3c.

6.1.2 Comparison of zonal-mean zonal winds

The QG experiments including the linear relaxation suggest that the equilibrium state, which is steady and anti-cyclonic, is very unlikely to be observed in the stratosphere. In the polar region, however, the axisymmetric flow temporarily becomes anti-cyclonic in a major SSW [1]. A reversal of the zonal-mean zonal wind $\overline{u}$ is also observed here. Figures 6.4a and 6.4b show the time series of the composite $\overline{u}$ in JRA-55 and the time-latitude section of $\overline{u}$ in the QG experiment with $\tau_{\mathrm{rlx}} = 10$ days, respectively. The simulated $\overline{u}$ changes from positive (westerly) to negative (easterly) at high latitudes, and the timing of the flow reversal well agrees with those in the composite $\overline{u}$. This result suggests that the state of the stratosphere temporarily becomes close to the anti-cyclonic equilibrium state, even though the state does not reach the equilibrium state. This is the reason why we argue that S-SSWs can be understood as the transition from QSS 1 *in the direction of* (not *to*) the equilibrium state.

[1] More precisely, a major SSW is defined by reversals of both the meridional temperature gradient and the zonal-mean zonal wind (Andrews et al. 1987; Butler et al. 2015). By contrast, in a minor SSW, the meridional temperature gradient is reversed, but the zonal-mean zonal wind remains westerly.

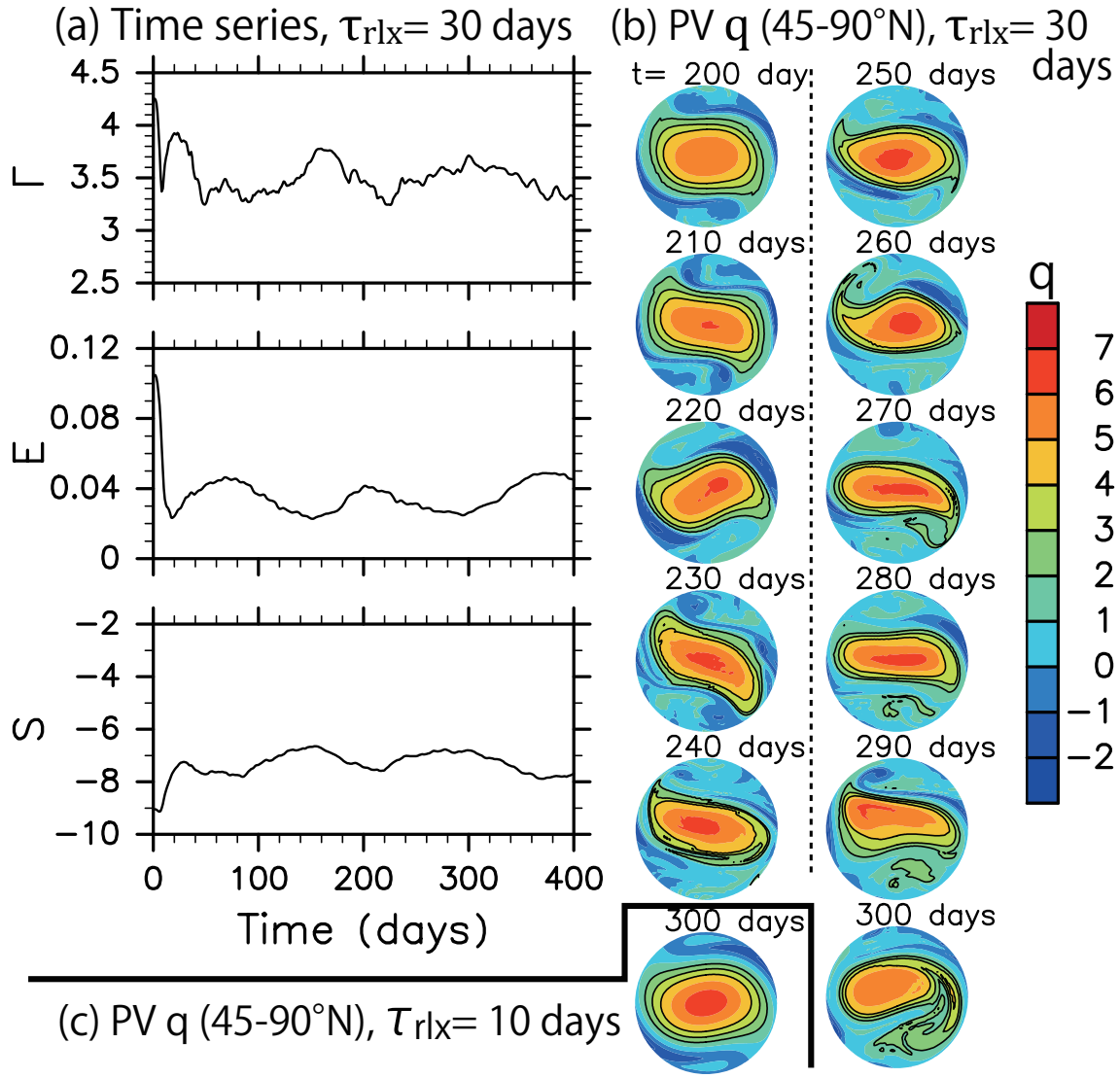

Figure 6.3: (a) and (b) Results from the QG experiment including the linear relaxation with $\tau_{\mathrm{rlx}} = 30$ days: (a) time series of the total PV Γ, the total energy E, and the entropy S; and (b) evolution of PV q over 45 to 90°N. (c) Quasi-steady PV field over 45 to 90°N in the QG experiment with $\tau_{\mathrm{rlx}} = 10$ days, which is observed at $t = 300$ days.

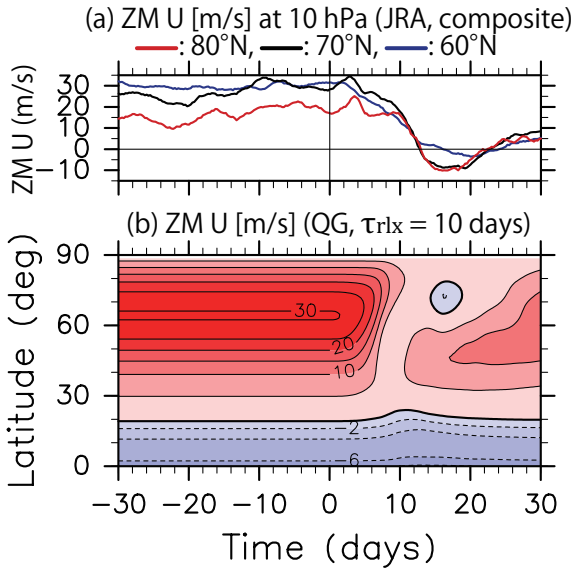

Figure 6.4: (a) Time series of the composite zonal-mean zonal winds $\overline{u}$ in JRA-55 at 60°N (blue), 70°N (black), and 80°N (red). (b) Time-latitude section of $\overline{u}$ in the QG experiment including the linear relaxation with $\tau_{\mathrm{rlx}} = 10$ days. In (a) and (b), $\overline{u}$ has the unit of m s^{-1}. For comparison, the onset time in (a) is shifted to $t = 10$ days, like in Figs. 3.4a and 6.1.

6.2 A view of potential

6.2.1 Comparisons with the previous studies on SSWs

Several studies have argued that SSWs are understood as some transition. Following Section 1.2, our understanding is compared with the interpretations given by the Holton-Mass model and by the resonance theory.

The most recent study employing the Holton-Mass model is Sjoberg and Birner (2014); however, their interpretation is essentially the same as that given by Chao (1985), who investigated the Holton-Mass model in terms of the catastrophe theory. According to Chao (1985), SSWs are interpreted as the transition from the steady state (close to the radiative equilibrium) to the vacillating state in the model. In other words, the Holton-Mass model has the two stable solutions at first (bistability), but one of them disappears when the bottom forcing is increased (Yoden 1987). This bistability relies on the Newtonian cooling. If the Newtonian cooling coefficient is zero, the bistability is not observed (Christiansen 2000), and the transition does not

occur. In our results, the bistability between the equilibrium state and QSS 1 is inherent in the fluid system itself (see Fig. 4.3), and the radiative cooling just selects QSS 1 among possible states.

The latest resonance theory was constructed by Matthewman and Esler (2011), who argued that the onset of S-SSWs is considered as the transition in the weakly nonlinear model describing the evolution of a barotropic Rossby wave. Their model has a potential form: $\ddot{X} = -\mathrm{d}\tilde{U}(X)/\mathrm{d}X$, where X is the wave amplitude and $\tilde{U}$ is a function of X. The transition in the model is understood with the potential $\tilde{U}$; however, the physical meaning of the potential $\tilde{U}$ is unclear. In our view, the entropy acts as a potential (see Fig. 1.4). The entropy S can be identified with the mixing (or Shannon) entropy (Bouchet 2008), which is equal to the number of possible (micro) states. The view of potential is further discussed in the next subsection.

On the other hand, our understanding cannot refer to the time evolution because equilibrium statistical mechanics is a static (not dynamical) theory. Both the Holton-Mass model and the resonance theory can describe the dynamics. The weakly nonlinear model of Matthewman and Esler (2011) gives a Rossby-wave evolution only in the onset period because the model is based on the small-amplitude assumption. Although the Holton-Mass model is a weakly nonlinear system as well, it describes a similar evolution of the zonal-mean flow over a long period ($\sim$ 100 days) to that in the atmosphere (e.g., Sjoberg and Birner 2014).

6.2.2 Potential given by the entropy

To clarify that the entropy acts as a potential, we first give a general form of the QG equation (Bouchet et al. 2014):

$$\frac{\partial q}{\partial t} + \boldsymbol{v} \cdot \boldsymbol{\nabla} q = -\int \mathcal{O}(\boldsymbol{x}, \boldsymbol{x}') \frac{\delta(-S)}{\delta q(\boldsymbol{x}')} \, \mathrm{d}\boldsymbol{x}' + \xi(\boldsymbol{x}, t), \tag{6.5}$$

where $O(\boldsymbol{x}, \boldsymbol{x}')$ is a linear operator and $\xi(\boldsymbol{x}, t)$ is an external force. Note that the functional derivative $\delta(-S)/\delta q(\boldsymbol{x}')$ is equal to $q(\boldsymbol{x}')$, where S is the entropy given by $-\int 1/2\, q^2\, \mathrm{d}\boldsymbol{x}$. For instance, if $O(\boldsymbol{x}, \boldsymbol{x}') = (\Delta^{10} + 1/\tau_{\mathrm{rlx}})\delta(\boldsymbol{x} - \boldsymbol{x}')$ and $\xi = q_{\mathrm{ini}}/\tau_{\mathrm{rlx}}$, where $\delta(\boldsymbol{x})$ is a Dirac delta function, (6.5) is identical to (6.1). The form of (6.5) is similar to that of Langevin equations[2] (e.g., Gardiner 2009; Sekimoto 2010). The only difference in the form is the nonlinear term on the left hand side in (6.5), but this term does not change the essence of the dynamics. The velocity component in the phase space attributed to the nonlinear term is along a contour of $-S$, whereas a motion perpendicular to the contour of $-S$ is driven only by the right hand side in (6.5). Figure 6.5a is a schematic picture of a velocity in the phase space. The analogy with the Langevin equations suggests that the negative of the entropy, $-S$, acts as a potential for the QG systems.

The only extremum of the potential $-S$ is at $q(\boldsymbol{x}) = 0$, which is trivial. If the motions are divided into a fast and a slow motion by using a perturbation expansion, the total PV Γ and energy E are constant in the fast motion, but the potential $-S$ decreases. In the slow motion, all Γ, E, and $-S$ gradually decrease, while the state of the system is always close to a quasi-stationary or the equilibrium state. This description of the dynamics is supported by the selective decay theories (e.g., Majda and Wang 2006). An effective potential for the fast motion will be the potential $-S$ constrained by constant Γ and E, which has been discussed so far. A transition in the fast motion is then discussed on the basis of the shape of the effective potential $-S$ (Fig. 6.5b). Theoretical methods for a transition in such a fast-slow system have been developed (e.g., Bouchet et al. 2016) and may be applicable to the general QG system

[2] A Langevin equation describes the evolution of a Brownian particle in a potential V:

$$\frac{\mathrm{d}x(t)}{\mathrm{d}t} = -\frac{\partial V}{\partial x} + \xi(t), \tag{6.6}$$

where x is a position of the particle and ξ is a white Gaussian noise. More precisely, this equation is an overdamped Langevin equation, where the acceleration is set to zero under the assumption of the sufficiently strong damping.

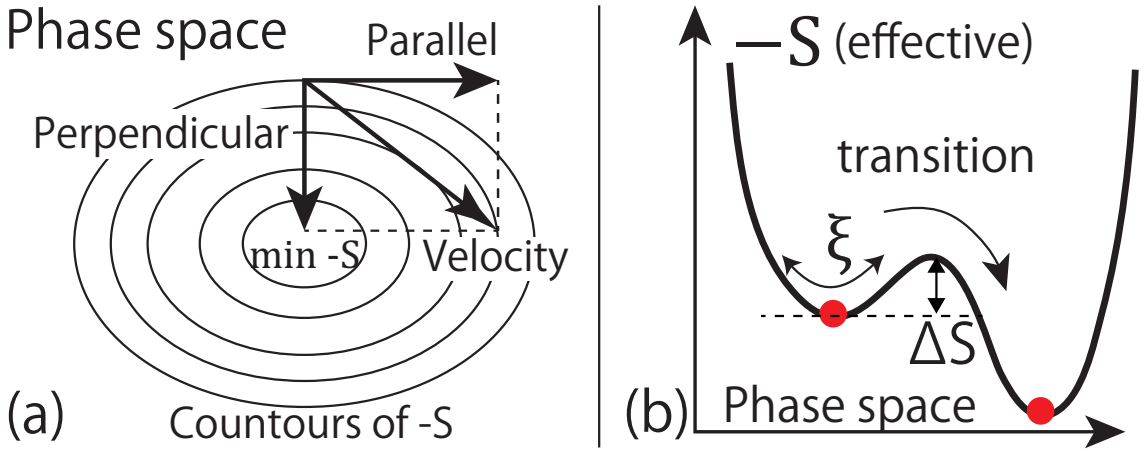

Figure 6.5: Schematic illustrations to explain a view of potential. (a) Decomposition of a velocity in the phase space. The component parallel to the $-S$ contour is attributed to the nonlinear term in (6.5). The perpendicular component is made only by the right hand side in (6.5). (b) Effective potential $-S$ for the fast motion in (6.5), which is constrained by constant total PV Γ and energy E. An external forcing ξ (for instance, a white noise) fluctuates the system around a local minimum of $-S$. When the system gets over the potential barrier ΔS, a transition occurs.

(6.5).

Recent studies have suggested that some transition observed in the atmosphere such as meridional shift of jet streams may be understood within the framework of Langevin models (e.g., Bouchet et al. 2014; Laurie and Bouchet 2015). The Langevin theory gives the most probable transition path and a transition rate from one state to another. In particular, the transition rate is expressed by the Arrhenius formula [$\sim \exp(-\Delta S/|\xi_{\mathrm{mean}}|)$], which is common in many chemical reactions. This formula means that a transition will occur more frequently, as the entropy barrier (ΔS) becomes lower and/or the mean amplitude of the external forcing ($|\xi_{\mathrm{mean}}|$) becomes larger. Figure 6.5b represents a transition in the effective potential $-S$.

Apart from the Langevin theory, the view of potential may be partially supported by the nonlinear stability theories (e.g., Holm et al. 1985; Swaters 1999). When entropy contours are closed around a basic state, all small-amplitude perturbations are bounded and cannot spontaneously grow; hence, a transition will be extremely rare (see Fig. 4.1). If the system got over

an entropy barrier due to adding a large-amplitude perturbation, the entropy contours might be open and the system could evolve into a completely different state.

6.2.3 Dependence of entropy barrier on the parameters

The view of potential implies that the magnitude of an entropy barrier gives the possibility of S-SSWs. The S-SSW will occur more frequently, as the magnitude of a barrier becomes smaller. As discussed in Section 4.3.2, QSS 1 is the only local maximum of the entropy (i.e., the local minimum of $-S$) when we ignore the gravest wavenumber-1 modes. Moreover, QSS 1 and QSS 2 annihilate at the same parameters (Fig. 4.5). Both results suggest that the entropy difference $\Delta S_{\mathrm{QSS1,2}}$ between QSS 1 and 2 gives an entropy barrier, which is determined by the total PV Γ, the total energy E, and the forcing amplitude a. Figure 6.6 shows the dependence of $\Delta S_{\mathrm{QSS1,2}}$ on (a) Γ and E at $a = 0.1$ and on (b) a and E at $\Gamma = 4.2$. Note that the zero contour of $\Delta S_{\mathrm{QSS1,2}}$ is identical to the domain boundaries of existence of QSS 1 and 2. The $\Delta S_{\mathrm{QSS1,2}}$ on the a-Γ plane is similar to that on the a-E plane in Fig. 6.6b (not shown). Clearly, $\Delta S_{\mathrm{QSS1,2}}$ is positive and a monotonic function of the parameters: $\Delta S_{\mathrm{QSS1,2}}$ becomes smaller, as E or Γ gets smaller or as a gets larger. We give brief discussions on the preconditioning of the polar vortex and the frequency of S-SSWs based on the view of the entropy potential.

Preconditioning of the polar vortex

The polar vortex is known to be preconditioned before an SSW by Rossby waves (e.g., McIntyre 1982). The polar vortex is displaced poleward and changed into a tighter and smaller shape due to these precursor waves, which will lead more Rossby waves to focus on the polar region. As a result, stronger wave forcings act on the (preconditioned) smaller polar vortex and an SSW finally occurs. These processes may be consistent with the view of the entropy potential. The smaller polar vortex will have smaller total PV Γ and energy E, which may lower

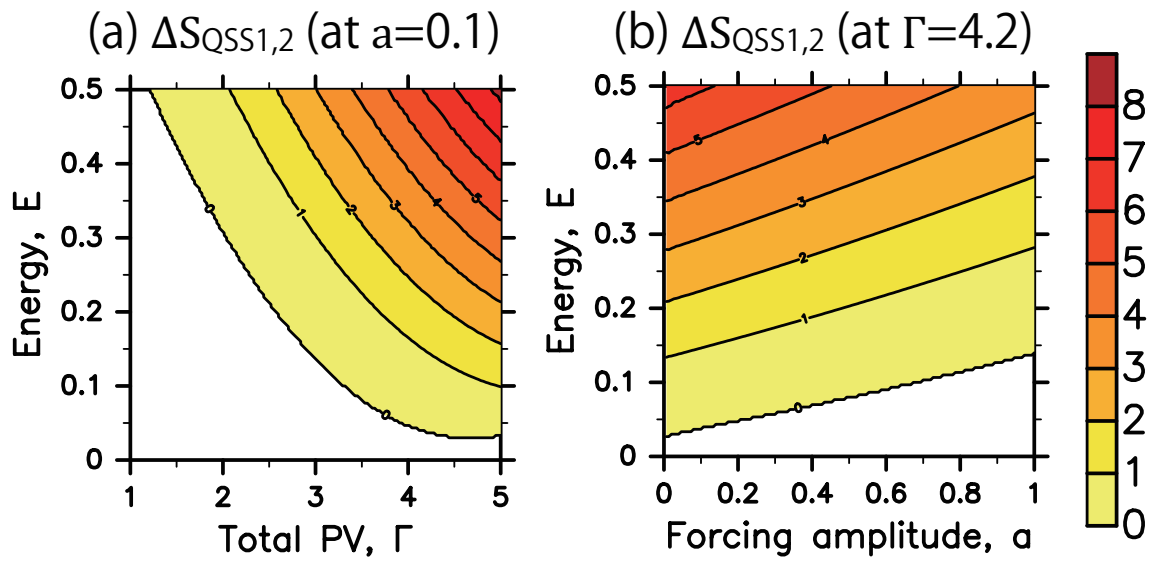

Figure 6.6: Entropy difference $\Delta S_{\mathrm{QSS1,2}}$ between QSS 1 and 2 on (a) the Γ-E plane at $a = 0.10$ and (b) the a-E plane at $\Gamma = 4.2$.

an entropy barrier as seen in Fig. 6.6a. This lowered barrier implies that an S-SSW occurs more easily.

Recent studies suggest that a preconditioning is caused mainly by baroclinic Rossby waves with zonal wavenumber 1 (e.g., Limpasuvan et al. 2004; Liberato et al. 2007; Charlton and Polvani 2007). The entropy potential around QSS 1 decreases only along the gravest wavenumber-1 modes in the phase space (Section 4.3.2), which implies that the state can escape from QSS 1 without getting over an entropy barrier. The results in Section 5.4 and Appendix B suggest that a wavenumber-1 Rossby wave having a sufficiently large amplitude is necessary to make the system escape from QSS 1 through such a path. Although our study is based on the barotropic model, these studies suggest an importance of wavenumber-1 Rossby waves in a preconditioning. An extension using the three-dimensional statistical mechanics (e.g., Venaille 2012) will clarify in more detail the effects of precursor baroclinic Rossby waves with wavenumber 1.

Frequency of S-SSWs in the Northern and Southern Hemispheres

We briefly discuss the frequency of S-SSWs in the Northern and Southern Hemispheres in terms of the dependence of $\Delta S_{\mathrm{QSS1,2}}$. All the above theoretical results are applied to a south polar cap if Γ is replaced with $-\Gamma$. In the Southern Hemisphere, the SSW in September 2002, which is vortex-split type, is the only SSW from the late 1950's to the present (Roscoe et al. 2005; Waugh and Polvani 2013). By contrast, SSWs occur in the Norther Hemisphere on average about once every two winters (e.g., Charlton and Polvani 2007). In JRA-55, we observe 30 SSWs (except for final warmings) between 1958 to 2014 (on average, 0.53 SSW per winter), where 18 events are S-SSWs, 6 are D-SSWs, and 6 are mixed-SSWs. The difference in the SSW frequency between both hemispheres is attributable to the topography (e.g., Haynes 2005). The undulation of the earth's surface and the land-sea heat contrast are stronger in the Northern Hemisphere, which leads to the strong Rossby-wave activity. Large-amplitude Rossby waves have two effects. First, they directly reduce $\Delta S_{\mathrm{QSS1,2}}$ through larger a. Second, these waves indirectly reduce $\Delta S_{\mathrm{QSS1,2}}$ through Γ and E, both of which are decreased by the strong PV mixing due to the wave breaking or by the form drag on the isentropic surface undulated by Rossby waves. Thus, $\Delta S_{\mathrm{QSS1,2}}$ will be smaller in the Northern Hemisphere. These discussions suggest that S-SSWs occur more frequently in the Northern Hemisphere, which is consistent with the previous studies and observations.

Chapter 7

General Conclusions

7.1 Summary of this thesis

Stratospheric sudden warming (SSW) is an extreme event in the stratosphere, which is categorized into vortex-displacement type (D-SSW) and vortex-split type (S-SSW) (Charlton and Polvani 2007). In a D-SSW, the polar vortex is displaced equatorward and broken down; in an S-SSW, the polar vortex collapses while splitting into the two daughter vortices. The dynamical mechanism for SSWs is basically understood with wave-mean interaction theories (Matsuno 1971). Following Matsuno, several researchers have theoretically studied SSWs in terms of wave-mean interactions to develop a better understanding (e.g., Chao 1985; Matthewman and Esler 2011). They have employed weakly nonlinear theories based on the assumption of small-amplitude perturbations. This assumption may be not necessarily satisfied well for strongly nonlinear phenomena such as SSWs.

Equilibrium statistical mechanics is a strongly nonlinear theory and has made great progress over the last two decades (e.g., Salmon 1998; Majda and Wang 2006; Bouchet and Venaille 2012). The statistical mechanics gives a variational problem such as an entropy maximization problem. We can obtain a large-scale coherent structure realized after strong PV (potential vorticity) mixing, by solving the variational problem without calculating a complicated flow evolution. Through these calculations, we can understand the effects of varying control pa-

rameters such as total energy. On the other hand, the statistical mechanics does not give any information on the time evolution and is applicable only to an isolated system without external forcing nor dissipation.

The present study has investigated S-SSWs by using a reanalysis dataset (JRA-55), a quasi-geostrophic (QG) barotropic model, and a statistical-mechanics theory, and has proposed a new understanding of S-SSWs: The S-SSW can be qualitatively understood as a transition from a cyclonic quasi-stationary state in the direction of the anti-cyclonic equilibrium state. A quasi-stationary state is defined as a saddle point of the entropy, and an equilibrium state as the entropy maximum. The transient state with the splitted two vortices is a non-equilibrium state that appears during the transition in the direction of the equilibrium. Without radiative cooling, the anti-cyclonic equilibrium state would be realized at a later time [O(100 days)] after an S-SSW. In the stratosphere, however, the radiative cooling [relaxation time = O(10 days)] will re-form the cyclonic polar vortex, before the anti-cyclonic equilibrium state is organized. In a major S-SSW, zonal-mean zonal winds change from westerly to easterly, which implies that the state of the stratosphere temporarily approaches the anti-cyclonic equilibrium state. The details of the results are as follows.

Chapter 2

The Japanese 55-year Reanalysis (JRA-55) has been analyzed, and the equivalent-barotropic nature of the composite S-SSW has been confirmed in the altitude range of about 20 to 40 km, as found by Matthewman et al. (2009). The composite S-SSW has been constructed with the method of Seviour et al. (2013), and its three-dimensional structure has been examined by using the modified PV (Lait 1994). During the composite S-SSW, disturbances with zonal wavenumber 2 are dominant, whose vertical scale is roughly estimated at 85 km. These results suggest that the dominant equivalent-

barotropic motions in S-SSWs can be described with a barotropic model.

Chapter 3

The spherical QG barotropic model has been constructed, and its validity has been confirmed through the direct comparison with the composite PV evolution obtained from JRA-55. The effective bottom forcing in the QG model is given by the composite height field of the 550-K isentropic surface ($\sim$ 20 km). The wavenumber-2 component of the bottom forcing is the most essential to the vortex splitting. To reveal a transition of the polar vortex, a quasi-static experiment has been conducted, where the amplitude of the wavenumber-2 forcing is increased linearly and sufficiently slowly with time. The flow field over the North Pole is nearly steady, except around the two transitions.

Chapter 4

The theory of statistical mechanics named the quadratic Casimir variational problem (QCVP, Chavanis and Sommeria 1996; Venaille and Bouchet 2009, 2011b; Naso et al. 2010) has been applied to the polar cap north of 45°N. In the QCVP, the entropy, which is the negative of potential enstrophy, is maximized with the constraints of constant total PV and energy. The equilibrium state is anti-cyclonic, but the quasi-stationary states are cyclonic, in the parameter range relevant to the winter stratosphere. The quasi-stationary state having the largest structure (QSS 1) can be a local maximum of the entropy (i.e., metastable) in a general domain not having the rotational symmetry. This unique property of QSS 1 comes from the fact that QSS 1 becomes an equilibrium state, as the total PV is increased. By contrast, in the disk domain, QSS 1 may be destabilized by a perturbation with zonal wavenumber 1, but it is dynamically stable against any small-amplitude perturbations with the other wavenumbers.

Chapter 5

The results of the quasi-static experiment have been interpreted by using the QCVP. The theory well explains the structures of the PV fields simulated by the QG model. Moreover, the timings of the two transitions given by the QCVP are consistent with those in the quasi-static experiment. The initial state in the quasi-static experiment is regarded as QSS 1, and the final state as the equilibrium state. To examine the nonlinear stability of QSS 1, the evolution of the wavenumber-1 perturbations have been examined by adding these perturbations to the flow field regarded as QSS 1 and performing the numerical integrations. In all cases, the small- but finite-amplitude perturbations do not grow with time, which implies that QSS 1 is Lyapunov stable. In a realistic experiment where the forcing amplitude is increased over one week (not sufficient slow), the polar vortex splits during the transition from QSS 1 to the equilibrium state. This result supports our understanding of S-SSWs.

Chapter 6

The effects of radiative cooling have been discussed by performing the QG experiments including the linear relaxation. The relaxation time is O(10 days), but the transition time toward the equilibrium state is about 200 days. As a result, the anti-cyclonic equilibrium state has not been observed in the QG experiments including the linear relaxation. The view of potential has also been discussed, which is given by the negative of the entropy. This view may extend our results to the Langevin dynamics, i.e., a theory of non-equilibrium statistical mechanics. The view of the entropy potential has given the consistent discussions with the previous studies to the preconditioning of the polar vortex and the frequency of S-SSWs in the Northern and Southern Hemispheres.

7.2 Future work

There are at least two important future themes. The first one is on vortex-displacement SSWs (D-SSWs). It is interesting whether D-SSWs can be considered as a transition in terms of equilibrium statistical mechanics. Since a baroclinic structure is essential for D-SSWs (Matthewman et al. 2009; Esler and Matthewman 2011), a continuously stratified QG model is necessary to investigate them. The three-dimensional version of the QCVP has already been developed and applied to geophysical fluid problems (e.g., Merryfield 1998; Venaille 2012). It will be a first step to analyze D-SSWs by using the three-dimensional QCVP.

Stratospheric final warming (SFW) is also an interesting phenomenon. In the onset of spring, the polar vortex rapidly becomes weak, while the zonal-mean zonal winds become easterly and do not return to westerly. This SFW event occurs once every year, and most of them are vortex-displacement type (Black and McDaniel 2007). The SFW (i.e., the change from winter to spring) may be regarded as a transition from a quasi-stationary *to* the equilibrium state; then, the equilibrium state will be observed as a summer state.

We have focused on the north polar cap, which is not a closed domain. When a stratified QG model covers an altitude range from the ground to the stratosphere, the fact that the polar cap is not closed will be essential to interpret D-SSWs and also S-SSWs. In this case, the bottom forcing is the earth's topography, which is time-invariant. The shape of the entropy surface is then changed by influx/efflux of energy and PV across the boundary of the polar cap. Our results suggest that S-SSWs will occur more easily, as the total PV or energy within the polar cap is decreased, i.e., as the polar vortex is weakened (Sections 4.4 and 6.2). This description may be directly related to an understanding of preconditionings.

The second important theme is extensions to non-equilibrium statistical mechanics. The radiative relaxation is important for actual transitions in the stratosphere (Section 6.1). The

time-mean state of the polar vortex is formed as a result of the balance between the forcing (i.e., radiative cooling) and the dissipation (i.e., eddy diffusion). Such a steady state is often observed in forced-dissipative systems and has been studied within the framework of non-equilibrium steady states (e.g., Bouchet and Venaille 2012). It is a challenging topic to understand S-SSWs with a theory of non-equilibrium steady states.

For another direction of development, the Langevin dynamics may be proposed (Section 6.2). The transience of Rossby waves may be incorporated into a system as a white noise. This system will be theoretically investigated with large-deviation techniques, which have been recently developed (e.g., Bouchet et al. 2014; Laurie and Bouchet 2015; Bouchet et al. 2016). It is challenging and interesting to examine time variations in the stratosphere by using large-deviation theories.

Appendix A

Vortex-Moment Diagnostics

The vortex-moment diagnostics has been originally developed by Waugh (1997) and later applied to the polar vortices (Waugh and Randel 1999) and to the classification of SSWs (Matthewman et al. 2009; Seviour et al. 2013). Following the latter two studies, we describe here this method.

The vortex-moment diagnostics is applicable to any two-dimensional field such as Ertel's PV, but geopotential height G at 10 hPa is used to explain the method. First, a geopotential-height field G over the Northern Hemisphere is projected onto the plane (x, y) with Lambert's map (4.6). Then, G is modified as

$$\hat{G} \equiv \begin{cases} \left| G - G_{\text{mean}} \right| & \text{for } G \leq G_{\text{mean}}, \\ 0 & \text{otherwise,} \end{cases} \tag{A.1}$$

where G_{mean} is the time- and zonal-mean of G at 60°N over all winters (December to March). Note that the inequality in (A.1) becomes opposite for (Ertel's) PV.

The equivalent ellipse is uniquely determined by its centroid $(x_{\text{cnt}}, y_{\text{cnt}})$, its aspect ratio η, its orientation χ, and its area $\mathcal{A}$. To obtain these quantities, the absolute moment is defined as

$$M_{kl} \equiv \int \hat{G} x^k y^l \, \mathrm{d}x \, \mathrm{d}y, \tag{A.2}$$

where k and l are arbitrary positive integers or zero. The centroid is then given by

$$(x_{\text{cnt}}, y_{\text{cnt}}) = \frac{1}{M_{00}} (M_{10}, M_{01}) . \tag{A.3}$$

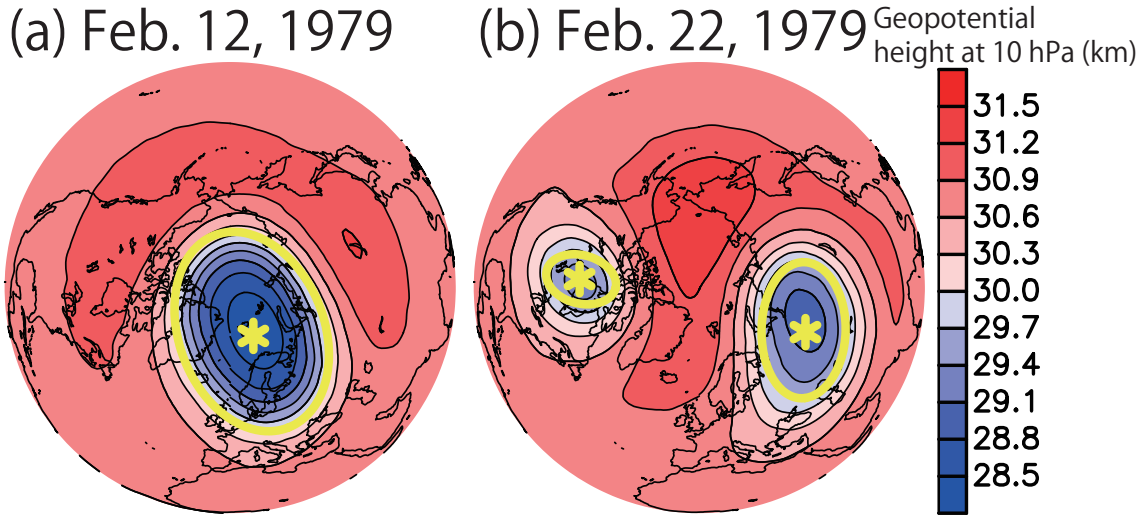

Figure A.1: Examples of the equivalent ellipse for geopotential height at 10 hPa in JRA-55. (a) Before the 1979 S-SSW. (b) After the 1979 S-SSW. Each yellow curve represents the equivalent ellipse and the asterisk its centroid.

By using the centroid, the relative moment is defined as

$$m_{kl} \equiv \int \hat{G}(x - x_{\mathrm{cnt}})^k (y - y_{\mathrm{cnt}})^l \, \mathrm{d}x \, \mathrm{d}y. \tag{A.4}$$

Finally, the aspect ratio η, orientation χ, and area $\mathcal{A}$ are given by

$$\eta = \left| \frac{m_{20} + m_{02} + \sqrt{4{m_{11}}^2 + (m_{20} - m_{02})^2}}{m_{20} + m_{02} - \sqrt{4{m_{11}}^2 + (m_{20} - m_{02})^2}} \right|^{1/2}, \tag{A.5}$$

$$\chi = \frac{1}{2} \tan^{-1}\left(\frac{2m_{11}}{m_{20} - m_{02}}\right), \tag{A.6}$$

and

$$\mathcal{A} = \frac{M_{00}}{G_{\mathrm{nrm}}}. \tag{A.7}$$

The orientation χ defines the angle between the x axis and the major axis of the equivalent ellipse. The normalization constant G_{nrm} in (A.7) is set to 10^3 m for geopotential height and 3.14 for barotropic PV q in (3.2). Figure A.1a shows an example of the equivalent ellipse (yellow) for the geopotential height at 10 hPa in JRA-55. The ellipse well represents the shape of the polar vortex.

In Section 2.1, S-SSWs have been identified with the method of Seviour et al. (2013), in which only the aspect ratio is necessary. Subsequently, we have extracted the 10 S-SSWs in which the two equivalent ellipses made by the vortex splitting are sufficiently separated from each other. The two equivalent ellipses are determined in the following four steps (Matthewman et al. 2009): (i) The centroid and orientation of the (single) equivalent ellipse are calculated as above; (ii) The projected domain is divided into two parts, $\mathcal{R}_1$ and $\mathcal{R}_2$, by the straight line $y - y_{\mathrm{cnt}} = -(x - x_{\mathrm{cnt}}) \cot\chi$, which is perpendicular to the major axis of the ellipse and is through its centroid; (iii) Two modified fields of geopotential height are defined as

$$\hat{G}^{(1)} \equiv \begin{cases} \hat{G} & \text{in } \mathcal{R}_1, \\ 0 & \text{in } \mathcal{R}_2, \end{cases} \quad \text{and} \quad \hat{G}^{(2)} \equiv \begin{cases} \hat{G} & \text{in } \mathcal{R}_2, \\ 0 & \text{in } \mathcal{R}_1; \end{cases} \tag{A.8}$$

(iv) The method described above is applied separately to $\hat{G}^{(1)}$ and $\hat{G}^{(2)}$, which gives the two equivalent ellipses. Figure A.1b shows an example of the two equivalent ellipses (yellow) after the February 1979 S-SSW. Each ellipse well represents the shape of the daughter vortex.

Appendix B

Quasi-static experiment using an initial state including all zonal-wavenumber components

We show here the results of a quasi-static experiment where the initial state includes all the zonal-wavenumber components. Similar results to those in Section 3.3.3 and Chapter 5 are obtained, and we basically emphasize the differences. These results suggest that the zonal-wavenumber-1 components are not critical to the emergence and persistence of QSS 1, even though its nonlinear stability against a wavenumber-1 perturbation is not theoretically assured.

The model configuration is the same as that described in Sections 3.3.1 and Section 3.3.3, except for the initial condition. The initial PV is given by the barotropic, climatological, absolute vorticity $\Delta\psi + f$ (not axisymmetric), which is made in the following two steps (Section 3.3.1): (i) The three-dimensional, climatological, absolute vorticity is obtained by simply averaging the absolute vorticity over the 55 midwinters (December to February) in JRA-55, except for the periods of SSWs; (ii) Its barotropic component is defined by vertically averaging the obtained absolute vorticity with a weight of density over $\theta = 550$ to 1300 K (about 22 to 39 km). The dominant zonal-wavenumber components are wavenumber 1, which is consistent with the climatology of the Arctic polar vortex (e.g., Waugh and Randel 1999).

Figure B.1 shows the results of the quasi-static experiment, like Fig. 3.6. The initial PV and

stream function are not axisymmetric, but similar results to those in Fig. 3.6 are obtained. There are three differences from Fig. 3.6: (i) QSS 1 persists until about $t = 4500$ days, but $t = 7000$ days in Fig. 3.6; (ii) The temporary increase in the major-axis angle of the equivalent ellipse at about $t = 5000$ days in Fig. 3.6a is not observed here; (iii) The major-axis angle reduces to about 0° just after the polar-vortex breakdown, but it remains near 90° in Fig. 3.6a. The first and second points may be related to each other. In Fig. 3.6, the state would change from State A (QSS 1) to B (QSS 3) at about $t = 5000$ days, if some noise were added. In this experiment, however, the initial state is axisymmetric and such a noise may be quite small; hence, only the major-axis angle may be sensitively changed at about $t = 5000$ days. By contrast, in the quasi-static experiment including all wavenumber components, these components may act as a noise, and the transition from State A (QSS 1) to B (QSS 3) occurs earlier due to this noise. The third difference is not important. The major-axis angle just after the polar-vortex collapse depends on the size of the small PV patch left after the collapse, which is also sensitive to the truncation wavenumber.

Figure B.2 compares the flow structures in the quasi-static experiment with those of the equilibrium and quasi-stationary states, like Fig. 5.3. There is apparently no qualitative difference from Fig. 5.3.

Figure B.3 shows the time series of the surf zone edges and the two PV fields before the two transitions, like Fig. 5.6. This figure is the preparation for comparing the transition timings.

Figure B.4 compares the transition timings given by the theory with those in the quasi-static experiment, like Figs. 5.4 and 5.5. Before the first transition, the north edge of the surf zone $\varphi_{\mathrm{surf,N}}$ is at about 39.4°N (Figs. B.3a and B.3b). The entropy minimum associated with the first transition was obscure when the calculations were performed within 39.4 to 90°N; hence, Fig. B.4a shows the results calculated over 40.8 to 90°N. Before the second transition, the north

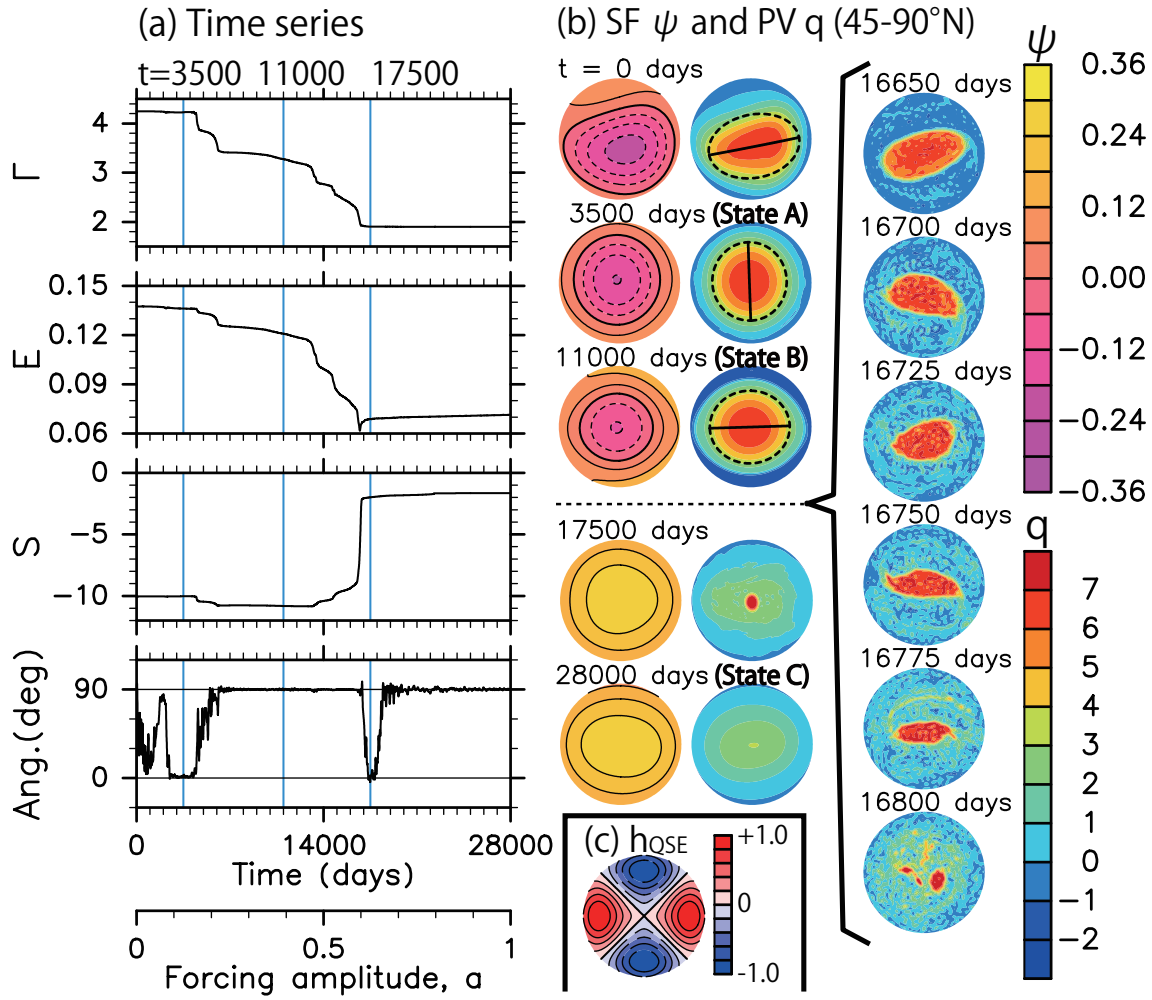

Figure B.1: As Fig. 3.6, but for the initial state including all the zonal-wavenumber components (not axisymmetric).

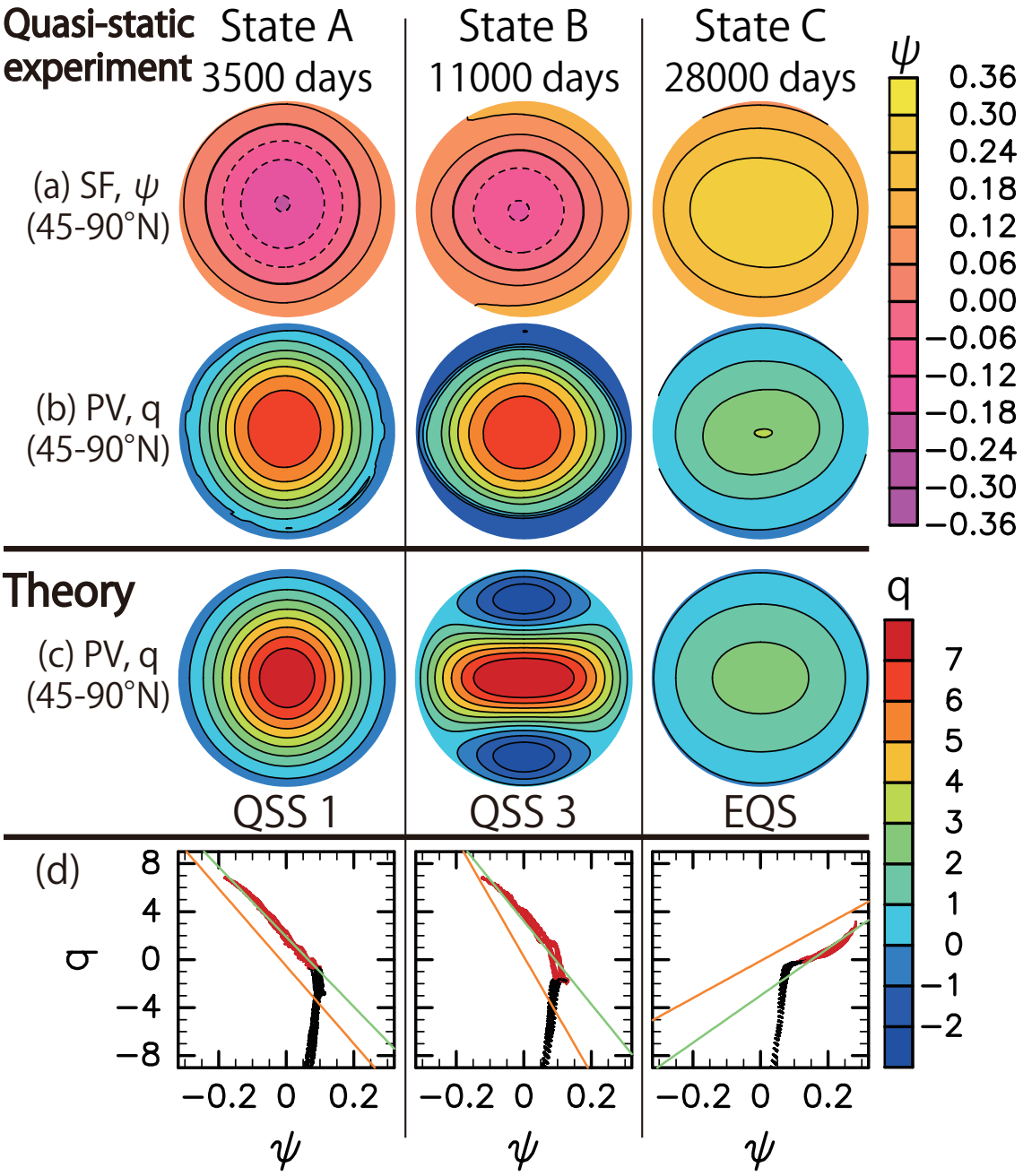

Figure B.2: As Fig. 5.3, but for the initial state including all the zonal-wavenumber components (not axisymmetric).

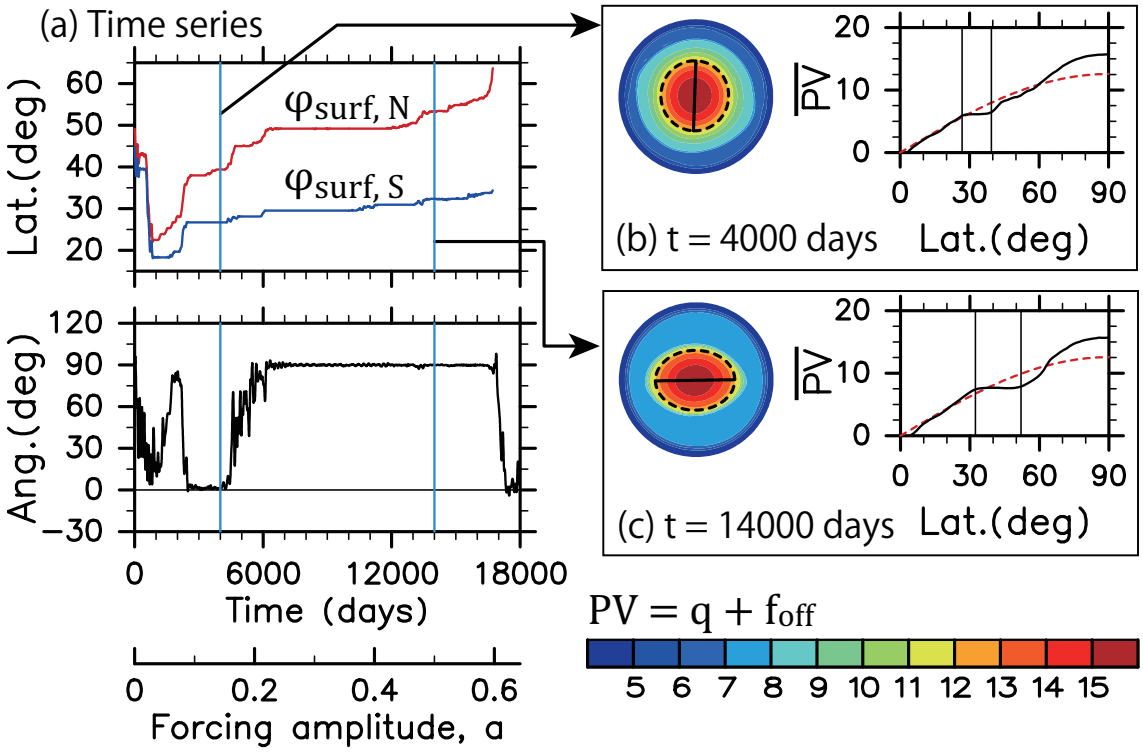

Figure B.3: As Fig. 5.6, but for the initial state including all the zonal-wavenumber components (not axisymmetric).

edge of the surf zone $\varphi_{\mathrm{surf,N}}$ is near 52.0°N (Figs. B.3a and B.3c). Figure B.4b shows the results obtained by the calculations within 52.0 to 90°N, which are not highly sensitive to the size of the polar cap. Obviously, the transition timings given by the theory are consistent with those in the quasi-static experiment, as in Section 5.3.

All the above results are similar to those discussed in Section 3.3.3 and Chapter 5. Thus, we can conclude that the zonal-wavenumber-1 components are not critical to the emergence and persistence of QSS 1 and our understanding of S-SSWs may be not strongly affected by the presence of zonal-wavenumber-1 disturbances.

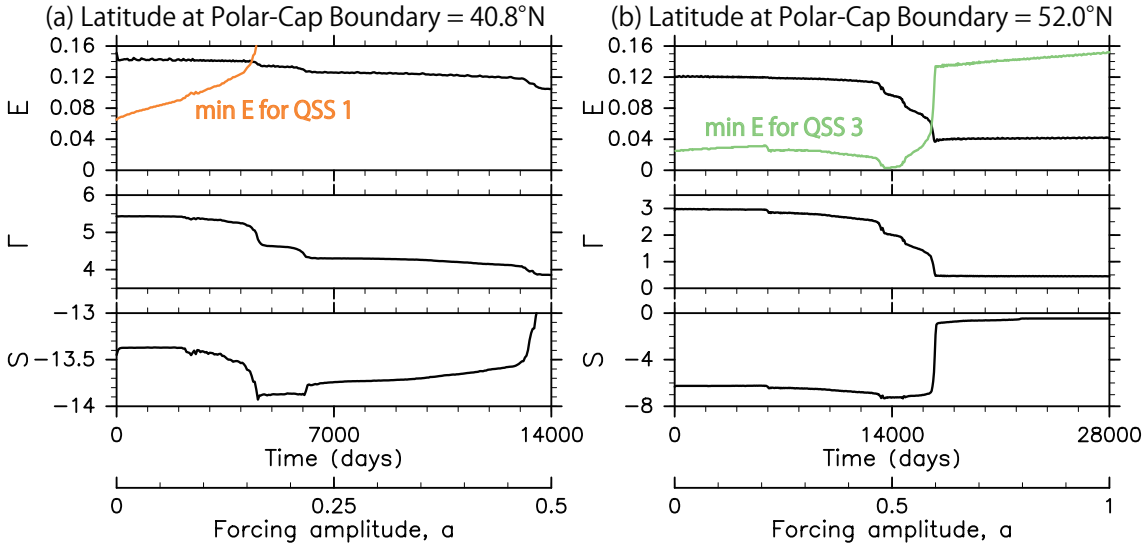

Figure B.4: As Figs. 5.4 and 5.5, but for the initial state including all the zonal-wavenumber components (not axisymmetric).

Appendix C

Details of Calculations to Obtain Equilibrium and Quasi-Stationary States

We describe here the method to obtain the equilibrium and quasi-stationary states for the QCVP (4.1). The discussions below basically follow the results of Venaille and Bouchet (2011b). We first introduce the complete, orthonormal basis $\{e_i\}_{i\in\mathbb{N}}$ of Laplacian eigenmodes on a simply connected domain such as a disk domain: $\Delta e_i = -\mu_i e_i$, where an eigenvalue μ_i is positive. Two subspaces are further introduced: one is composed of the Laplacian eigenmodes having zero mean values ($\langle e_i' \rangle = 0$) and the other is composed of the eigenmodes having non-zero mean values ($\langle e_i'' \rangle \neq 0$), where $\langle\ \rangle$ denotes spatial integral over the domain, and $'$ and $''$ emphasize the difference between the two subspaces. In each subspace, the eigenvalues are in ascending order. Appendix D gives the Laplacian eigenmodes and eigenvalues in a disk and a rectangular domain.

All quantities are expressed in terms of the coordinates $\{q_i\}$ [i.e., the coefficients of PV q ($\equiv \sum_i q_i e_i$)]:

$$\psi_i = -\frac{q_i - h_{\mathrm{tot}i}}{\mu_i}, \tag{C.1}$$

$$\Gamma = \sum_i q_i \langle e_i \rangle, \tag{C.2}$$

$$E = \frac{1}{2} \sum_i \frac{(q_i - h_{\mathrm{tot}i})^2}{\mu_i}, \tag{C.3}$$

and

$$S = -\frac{1}{2}\sum_i q_i^2, \tag{C.4}$$

where $h_{\rm tot}$ ($\equiv \sum_i h_{{\rm tot}i}e_i$) is the sum of $f - f_{\rm off}$ and fh/H in (4.4), and ψ_i is a coefficient of the stream function ψ ($\equiv \sum_i \psi_i e_i$). Note that (C.1) represents the PV inversion (4.4) given by $q \equiv \Delta\psi + f - f_{\rm off} + fh/H \equiv \Delta\psi + h_{\rm tot}$. When both $'$ and $''$ are not attached to variables in a summation, the summation is taken over all indices of both subspaces. The expression of PV at a stationary point for the QCVP is obtained by expanding the linear q-ψ relation (4.5) by the Laplacian eigenmodes:

$$q_i = \frac{bh_{{\rm tot}i} - c\mu_i\langle e_i\rangle}{\mu_i + b}. \tag{C.5}$$

The expressions of Γ and E at a stationary point are obtained by substituting (C.5) into (C.2) and (C.3), respectively:

$$\Gamma = -cF(b) + b\sum_i \frac{h_{{\rm tot}i}\langle e_i\rangle}{\mu_i + b}, \tag{C.6}$$

and

$$E = \left(\sum_i \frac{\mu_i h_{{\rm tot}i}^2}{2(\mu_i + b)^2}\right) + c\left(\sum_i \frac{\mu_i h_{{\rm tot}i}\langle e_i\rangle}{(\mu_i + b)^2}\right) + c^2\left(\sum_i \frac{\mu_i\langle e_i\rangle^2}{2(\mu_i + b)^2}\right), \tag{C.7}$$

where

$$F(b) \equiv \sum_i \frac{\mu_i\langle e_i\rangle^2}{\mu_i + b}. \tag{C.8}$$

Any stationary point given by (C.5) with $b > -\mu_1{}'$ and $-\mu^*$ is a solution of the QCVP, namely the equilibrium state, where $\mu_1{}'$ is the smallest Laplacian eigenvalue for the zero-mean eigenmodes and $-\mu^*$ is the largest zero of $F(b)$ [i.e., $F(-\mu^*) = 0$]. In the parameter range considered in the present study, b of the equilibrium states is always larger than $-\mu_1{}'$ and $-\mu^*$. See Venaille and Bouchet (2011b) for the method to calculate the equilibrium state with $b = -\mu_1{}'$ or $-\mu^*$. Note that equilibrium states with $b < -\mu_1{}'$ or $-\mu^*$ do not exist.

An equilibrium or a quasi-stationary state is obtained in the following four steps: (i) The Lagrange multiplier c [i.e., the offset of the q-ψ relation in (4.5)] is analytically obtained by

solving (C.6) with a given Γ; (ii) The equation $E = E(b)$ is derived by substituting the obtained c into (C.7) with a given E; (iii) The Lagrange multiplier b [i.e., the inclination of the q-ψ relation in (4.5)] satisfying $E = E(b)$ is numerically calculated; (iv) q_i is computed by substituting the obtained b and c into (C.5). When $b > -\mu_1'$ and $-\mu^*$, the obtained q is the only equilibrium state for the given Γ and E. In the other cases, the obtained q is a quasi-stationary state, and an appropriate b needs to be selected at the third step (iii).

We further explain how to determine an appropriate b. Figure C.1 gives two examples of the energy curve $E(b)$ for a disk domain. The shape of the energy curve is uniquely determined by the total PV Γ and the forcing amplitude a. The E curve is divergent at $b = -\mu^*$, $-\mu_2'$, and $-\mu^{**}$, because some denominators in the equation of $E = E(b)$ are zero (not shown), where μ_2' is the second smallest Laplacian eigenvalue for the zero-mean eigenmodes and $-\mu^{**}$ is the second largest zero of $F(b)$. The E curve has infinitely many branches, which means that there are infinitely many quasi-stationary states (Chavanis and Sommeria 1996). In the range of $-\mu^* < b$, the intersection of the E curve (black) with a given E (i.e., a lateral line) is uniquely determined and it gives b for the equilibrium state. In the range of $b < -\mu^*$, the intersection of the first branch (light green) gives b for QSS 1. Other b for QSS n are determined in the same way. In Fig. C.1a, all the shown branches have the intersections with the lateral line of $E = 0.12$, but in Fig. C.1b, the first (light green) and second (dark blue) branches do not have intersections. In the case (b), QSS 1 and 2 do not exist, but another QSS such as QSS 3 exists. In making Fig. 4.4, we numerically calculated an energy curve at each parameter point of (a, Γ) and examined whether an appropriate b existed. Thus, a domain with existence of a quasi-stationary state is a parameter set over which the corresponding branch of the energy curve has the intersection with the given E. Furthermore, the shape of the energy curve indicates that QSS n and QSS $n + 1$ (n is odd) annihilate at the same parameter point of (a, Γ, E).

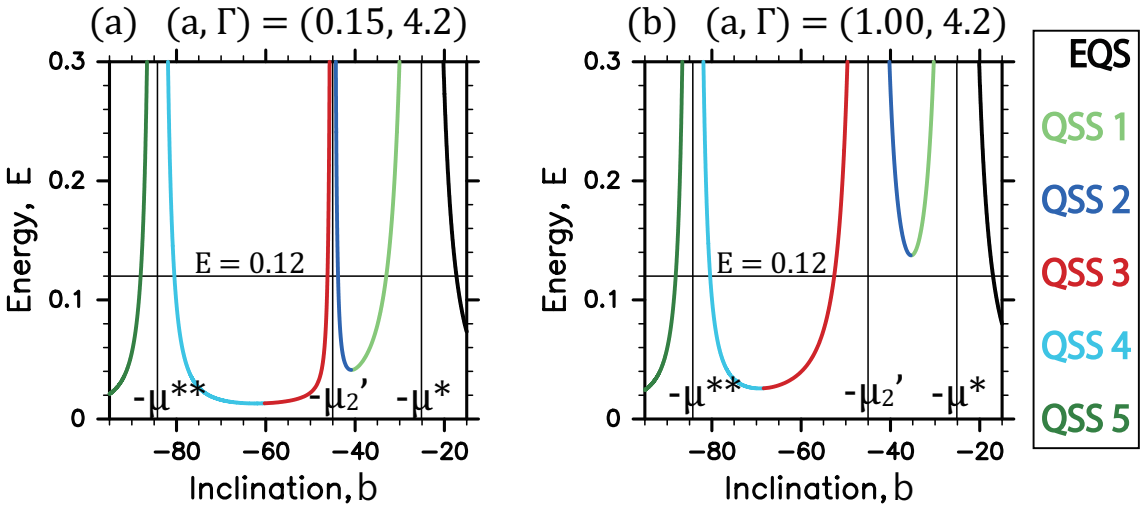

Figure C.1: Examples of the energy curve $E(b)$ at (a) $(a, \Gamma) = (0.15, 4.2)$ and (b) $(a, \Gamma) = (1.00, 4.2)$. The label EQS stands for equilibrium state. See text for details.

Appendix D

Laplacian Eigenvalues and Eigenmodes

D.1 Disk domain

We give the Laplacian eigenmodes and eigenvalues in a disk domain ($0 \leq r \leq r_{\max}$ and $0 \leq \lambda < 2\pi$). A position in the domain is specified by a radius r and an azimuthal angle[1] λ, where the maximum of r is designated as $r_{\max}$. The Laplacian eigenmodes are given by Bessel functions of the first kind J_n and trigonometric functions, when the Dirichlet boundary condition is imposed (i.e., $e_i = 0$ at $r = r_{\max}$):

$$\{e_i{}'\}_{i\in\mathbb{N}} = \left\{ C_{n,m}\, J_n\left(\frac{\alpha_{n,m}}{r_{\max}} r\right)\sin(n\lambda),\ \ C_{n,m}\, J_n\left(\frac{\alpha_{n,m}}{r_{\max}} r\right)\cos(n\lambda) \right\}_{n,m\in\mathbb{N}}, \tag{D.1}$$

$$\{e_i{}''\}_{i\in\mathbb{N}} = \left\{ C_{0,i}\, J_0\left(\frac{\alpha_{0,i}}{r_{\max}} r\right) \right\}_{i\in\mathbb{N}}, \tag{D.2}$$

and

$$\langle e_i{}''\rangle = \frac{2\sqrt{\pi} r_{\max}}{\alpha_{0,i}} \mathrm{sgn}\left(J_1\left(\alpha_{0,i}\right)\right), \tag{D.3}$$

where $C_{n,m}$ is a normalization constant [$\langle (e_i)^2 \rangle = 1$] and $\alpha_{n,m}$ is the m-th zero of J_n. The corresponding eigenvalue is given by

$$\mu = (\alpha_{n,m}/r_{\max})^2. \tag{D.4}$$

[1] Azimuthal angle is identical to longitude λ when a disk domain is obtained with Lambert's map (4.6).

D.2 Rectangular domain

We give the Laplacian eigenmodes and eigenvalues in a rectangular domain with sides of L_x and L_y. A position in the domain is specified by x and y, where $0 \leq x \leq L_x$ and $0 \leq y \leq L_y$. The Laplacian eigenmodes are given by sine functions, when the Dirichlet boundary condition is imposed:

$$\{e_i\}_{i\in\mathbb{N}} = \left\{\tilde{C}_{m,n} \ \sin\left(\frac{m\pi x}{L_x}\right)\sin\left(\frac{n\pi y}{L_y}\right)\right\}_{m,n\in\mathbb{N}}, \tag{D.5}$$

where $\tilde{C}_{m,n}$ is a normalization constant [$\langle(e_i)^2\rangle = 1$]. An eigenmode with m or n even gives $e_i{}'$, and an eigenmode with both m and n odd gives $e_i{}''$, where

$$\langle e_i{}''\rangle = \frac{8\sqrt{L_x L_y}}{mn\pi^2}. \tag{D.6}$$

The corresponding eigenvalue is given by

$$\mu = \pi^2\left(\frac{m^2}{{L_x}^2} + \frac{n^2}{{L_y}^2}\right). \tag{D.7}$$

Appendix E

Quadratic Form Expressing the Entropy Surface around a Stationary Point

According to the Lagrangian multiplier theory (e.g., Gelfand and Fomin 2000), the necessary and sufficient condition that a stationary point for the QCVP (4.1) is a local maximum of the entropy is given by the following second-order variation, where a perturbation δq satisfies the two first-order constraints:

$$0 < -\delta^2 S + b\delta^2 E = \frac{1}{2}\sum_i \left(1 + \frac{b}{\mu_i}\right)(\delta q_i)^2 \quad \text{s.t.} \quad \delta\Gamma = 0 \quad \text{and} \quad \delta E = 0. \tag{E.1}$$

The first-order constraints are expressed in terms of $\{\delta q_i\}$ (i.e., the coefficients of δq by Laplacian eigenmodes):

$$0 = \delta\Gamma = \sum_i \langle e_i \rangle \delta q_i = \sum_i \langle e_i{}'' \rangle \delta q_i{}'', \text{ and} \tag{E.2}$$

$$0 = \delta E = \sum_i \psi_i \delta q_i. \tag{E.3}$$

The value of ψ_i is given by substituting (C.5) into (C.1).

The necessary and sufficient condition (E.1) is not quite easy to handle because of the two first-order constraints. We solve these two linear constraints, (E.2) and (E.3), for $\delta q_1{}''$ and $\delta q_2{}''$:

$$\begin{aligned}\delta q_1{}'' &= \sum_{i\geq 3}\left[-\frac{\langle e_i{}'' \rangle}{\langle e_1{}'' \rangle} + \frac{\langle e_2{}'' \rangle}{\langle e_1{}'' \rangle}\left(\frac{\psi_i{}'' - \psi_1{}''\langle e_i{}'' \rangle/\langle e_1{}'' \rangle}{\psi_2{}'' - \psi_1{}''\langle e_2{}'' \rangle/\langle e_1{}'' \rangle}\right)\right]\delta q_i{}'' + \sum_{i\geq 1}\frac{\langle e_2{}'' \rangle}{\langle e_1{}'' \rangle}\left(\frac{\psi_i{}'}{\psi_2{}'' - \psi_1{}''\langle e_2{}'' \rangle/\langle e_1{}'' \rangle}\right)\delta q_i{}' \\ &\equiv \sum_i A_i \delta q_i,\end{aligned} \tag{E.4}$$

and

$$\begin{aligned}\delta {q_2}'' &= -\sum_{i\geq 3}\left(\frac{{\psi_i}'' - {\psi_1}''\langle {e_i}''\rangle/\langle {e_1}''\rangle}{{\psi_2}'' - {\psi_1}''\langle {e_2}''\rangle/\langle {e_1}''\rangle}\right)\delta {q_i}'' - \sum_{i\geq 1}\left(\frac{{\psi_i}'}{{\psi_2}'' - {\psi_1}''\langle {e_2}''\rangle/\langle {e_1}''\rangle}\right)\delta {q_i}' \\ &\equiv \sum_i B_i \delta q_i. \end{aligned} \tag{E.5}$$

Substituting $\delta {q_1}''$ and $\delta {q_2}''$ into (E.1), we obtain the quadratic form expressing the second-order variation (E.1), in which the two first-order constraints are incorporated:

$$\begin{aligned}&2\left(-\delta^2 S + b\delta^2 E\right) = \\ &\sum_{\text{other } i'}\left(1+\frac{b}{{\mu_i}'}\right)\delta {q_i}'^2 + \sum_{i,j}\underbrace{\left[\delta_{ij}\left(1+\frac{b}{\mu_i}\right) + A_i A_j\left(1+\frac{b}{{\mu_1}''}\right) + B_i B_j\left(1+\frac{b}{{\mu_2}''}\right)\right]}_{Q_{ij}}\delta q_i \delta q_j,\end{aligned} \tag{E.6}$$

where δ_{ij} is a Kronecker delta and *other* i' means all indices of the zero-mean eigenmodes whose ${\psi_i}'$ are zero (i.e., whose A_i and B_i are zero). The quadratic form (E.6) is decomposed into the first sum consisting of the diagonal matrix and the second sum consisting of the symmetric matrix Q. The quadratic form (E.6) expresses the entropy surface around a stationary point in the phase space. When (E.6) is positive definite, the condition (E.1) is satisfied and the stationary point is a local maximum of the entropy (i.e., dynamically and nonlinearly stable).

The definiteness of the quadratic form (E.6) is examined in the following three steps: (i) The definiteness of Q is checked by numerically computing the eigenvalues of Q; The matrix Q is positive definite, if and only if all eigenvalues are positive; (ii) The value of b is compared with the eigenvalues ${\mu_i}'$; The first sum in (E.6) is positive for any δq, if and only if $-{\mu_1}' < b$, where ${\mu_1}'$ is the smallest Laplacian eigenvalue for the zero-mean eigenmodes; (iii) If Q is positive definite and if $-{\mu_1}' < b$, the quadratic form (E.6) is positive definite and the stationary point is a local maximum of the entropy. Clearly, any stationary point with $b < -{\mu_1}'$ does not satisfy this condition; hence, it is a saddle point of the entropy. Naso et al. (2010) showed the same result through a different method: They found a specific first-order perturbation, substituted it into $-\delta^2 S + b\delta^2 E$, and showed that the condition (E.1) is not satisfied for a stationary point with

$b < -\mu_1{}'$.

The uniqueness of QSS 1 comes from the positive definiteness of the symmetric matrix Q. This means that QSS 1 is a local maximum of the entropy if $-\mu_1{}' < b$. In other words, the structure of the entropy surface around QSS 1 is determined only by the inequality of b and $-\mu_1{}'$. Furthermore, the value of $\mu_1{}'$ is determined only by the shape of a domain.

In a disk domain, $\mu_1{}'$ is given by the gravest wavenumber-1 mode[1] and satisfies $-\mu^* < -\mu_1{}'$. The range of b for QSS 1 is analytically obtained as $-\mu_2{}' < b < -\mu^*$, where $\mu_2{}'$ is the second smallest Laplacian eigenvalue for the zero-mean eigenmodes[2]. These facts mean that any b of QSS 1 is smaller than $-\mu_1{}'$ and QSS 1 is always a saddle point of the entropy[3]. In the quadratic form (E.6), the gravest wavenumber-1 components of a perturbation, $\delta q_1{}'$, are included only in the first sum. If a perturbation δq does not have these components, the quadratic form (E.6) is positive. Only in this case, QSS 1 becomes a local maximum of the entropy.

In a square domain, $-\mu_1{}' < -\mu^*$ holds and any b of QSS 1 is smaller than $-\mu^*$, which suggests that $-\mu_1{}' < b$ can be satisfied, depending on the parameters of a, Γ, and E. In other words, QSS 1 can be a local maximum of the entropy (i.e., metastable) and dynamically stable against *any* small-amplitude perturbation. See Appendix F for details.

[1]Note that $\mu_1{}' = (\alpha_{1,1}/r_{\max})^2$ and $-\mu^*$ is the largest zero of $F(b)$ in (C.8) [i.e., $F(-\mu^*) = 0$].
[2]The value of $\mu_2{}'$ is given by the gravest wavenumber-2 mode: $\mu_2{}' = (\alpha_{2,1}/r_{\max})^2$.
[3]All other quasi-stationary states are saddle points as well because QSS 1 has the largest b.

Appendix F

Theoretical Calculations in a Square Domain

In Chapter 4, for simplicity, the theoretical calculations have been performed in the disk domain, which has the rotational symmetry. An infinitely small perturbation to the domain boundary can break the rotational symmetry. This fact indicates that if an effective boundary for the polar stratosphere is accurately determined, the domain will not have such a special symmetry. In this chapter, we investigate the properties of QSS 1 in a square domain, which has no continuous symmetry. The obtained results here would be representative of those in a domain having a complex boundary.

The square domain has the same side length as the diameter of the disk obtained by the projection of the polar cap (45 – 90°N) with Lambert's map (4.6). As in the disk (Chapter 4), the Coriolis parameter and bottom forcing are projected and the same calculation methods are employed. The form of Laplacian eigenmodes and eigenvalues in a square domain is given in Appendix D.2. Note that similar results to the following are obtained in a rectangular domain with its aspect ratio smaller than about 1.12.

First, the energy curve $E(b)$ is investigated. Figure F.1 shows the E curve at the total PV $\Gamma = 6.1$ and the forcing amplitude $a = 0.01$, together with the four PV fields. The black curve is the equilibrium branch and the green is the QSS-2 branch (see also Appendix C). The QSS-1

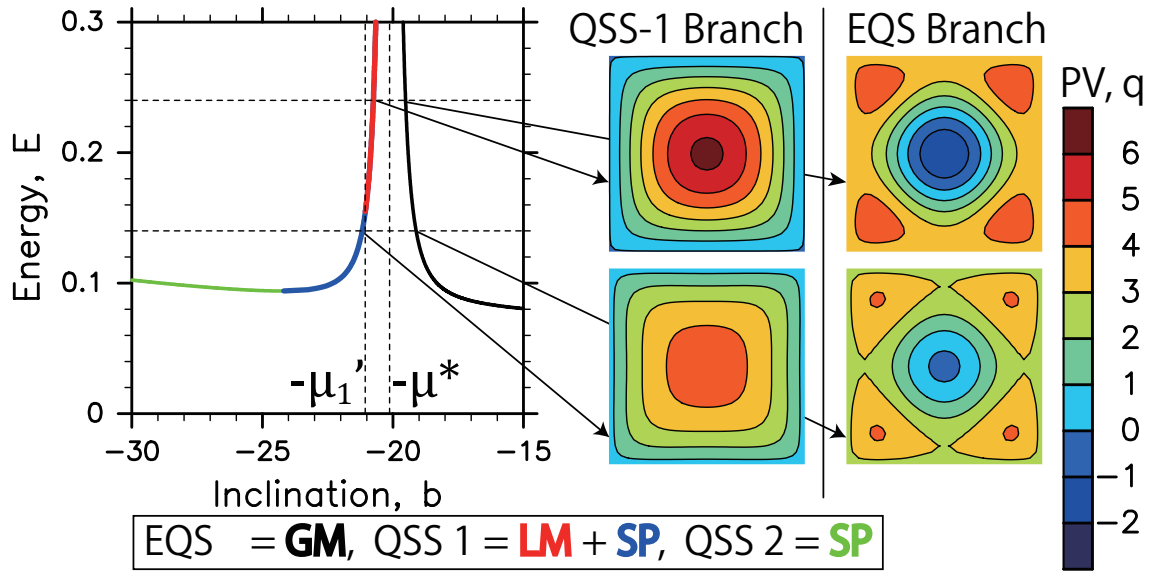

Figure F.1: Energy curve $E(b)$ in the square domain at the total PV $\Gamma = 6.1$ and the forcing amplitude $a = 0.01$. The black curve represents the equilibrium branch (EQS), which is the global maximum (GM) of the entropy. The green curve represents the QSS-2 branch, which is a saddle point (SP) of the entropy. The QSS-1 branch is composed of the red curve, which is the metastable branch (i.e., local maximum, LM, of the entropy), and the blue curve, which is the quasi-stationary branch (i.e., saddle point, SP, of the entropy). The PV fields at the intersections of the E curves with the lateral lines $E = 0.12$ and 0.24 are also shown.

branch is composed of the red and blue curves, which are referred to as the metastable and quasi-stationary branches, respectively. In the QSS-1 branch, any state with $-\mu_1{}' < b$ (red) is a local maximum (LM) of the entropy, namely metastable, and any other state (blue) is a saddle point (SP), namely quasi-stationary, as discussed in Appendix E. At the point of $b = -\mu_1{}'$, nothing happens. In fact, the metastable PV (top left) has a similar cyclonic structure to that of the quasi-stationary PV (bottom left). For comparison, the equilibrium PV are shown, which are anti-cyclonic. Similar results are observed at another point of (a, Γ).

The uniqueness of QSS 1 has been briefly explained in Section 4.3.2. We discuss here it more deeply. Figure F.2b shows the 3D plot of the equilibrium entropy S_{EQ} in the Γ-E space at $a = 0.01$:

$$S_{\mathrm{EQ}}(E, \Gamma) \equiv \max_{q} \left\{ S \equiv -\frac{1}{2} \int q^2 \, \mathrm{d}A \;\middle|\; E, \Gamma \right\}. \tag{F.1}$$

The S_{EQ} surface has the two peaks with the cusp (red line) given by $\Gamma = \Gamma^*$, where

$$\Gamma^* \equiv -\mu^* \sum_i \frac{h_{\mathrm{tot}i}\langle e_i \rangle}{\mu_i - \mu^*}. \tag{F.2}$$

The red line is called the first-order phase transition line because the first derivative of $\partial S_{\mathrm{EQ}}/\partial\Gamma$ is discontinuous on it (Venaille and Bouchet 2011b). Figure F.2c shows the corresponding phase diagram. The end point of the first-order phase transition line (red) is given by the minimum energy for all equilibrium states with $b = -\mu^*$.

Venaille and Bouchet (2009, 2011b) showed that the equilibrium states are switched between the cyclonic and anti-cyclonic branches at the first-order phase transition line, which makes the cusp of the S_{EQ} surface. In addition, Naso et al. (2010) demonstrated that the cyclonic branch becomes metastable on the side where the anti-cyclonic branch is equilibrium. To further develop an understanding on the entropy surface, the parameter domains with existence of the metastable state and QSS 1 are calculated with the methods of Appendices C and E. The metastable branch is a part of the QSS-1 branch; hence, in Fig. F.2c, the domain of QSS 1 (orange) contains the domain of metastability (blue). The domain of metastability is quite narrow, and the state of the winter stratosphere is unlikely to be considered as a metastable state. The cyclonic and anti-clonic branches do not end at the domain boundary of metastability, but they extend to the domain of existence of QSS 1. Figure F.2a is a schematic illustration for the structure of the entropy surface, where the two black curves represent S_{EQ}. At the domain boundary of QSS 1, both branches disappear because any solution for $E = E(b)$ does not exist (see Appendix C). Similar results are obtained at another forcing amplitude a, but the domain of metastability as well as the domain of QSS 1 becomes narrow and shifts to a region with higher energies, as a becomes larger. These results give the foundation for the brief discussions in Section 4.3.2.

The equilibrium entropy S_{EQ} is not globally concave. The boundary of non-globally-

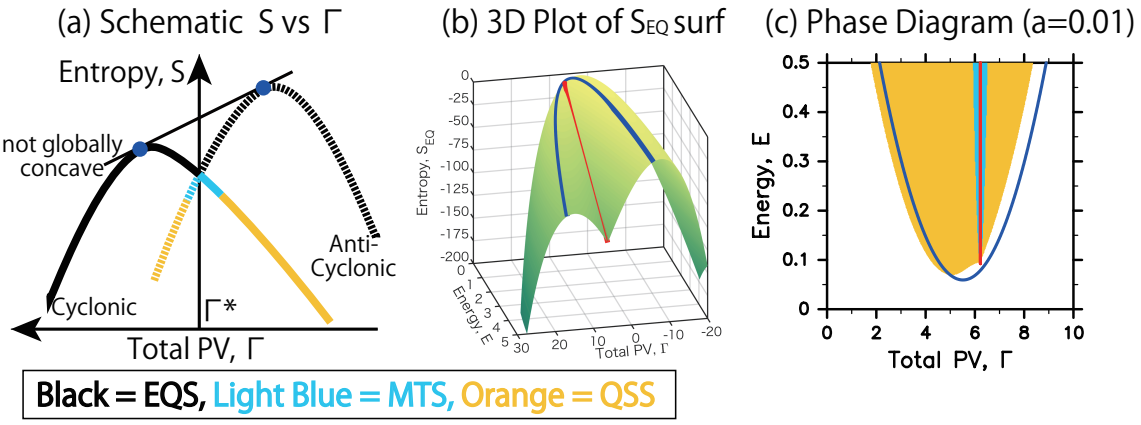

Figure F.2: (a) Schematic illustration of the entropy curve at a constant energy. (b) 3D plot of the equilibrium entropy S_{EQ} surface in the Γ-E space with $a = 0.01$. (c) Phase diagram in the Γ-E space with $a = 0.01$. The red line represents the first-order phase transition line $\Gamma = \Gamma^*$ given by (F.2). The blue curve shows the boundary for the non-globally-concave domain of S_{EQ} given by the energy curve with $b = -\mu_1''$. Two blue dots in (a) correspond to the blue curves in (b) and (c). The light-blue area in (c) represents the domain of metastability, which corresponds to the light-blue curves in (a). The orange area in (c) shows the domain with existence of QSS 1, which corresponds to the orange curves in (a). The label EQS stands for equilibrium state, MTS metastable state, and QSS quasi-stationary state.

concave domain is shown by the blue curve in Fig. F.2b or F.2c, which is given by the energy curve[1] $E = E(\Gamma, b)$ with $b = -\mu_1''$ (Venaille and Bouchet 2011b). In Figure F.2a, the non-globally-concave domain is emphasized by the two blue dots with the auxiliary line. In usual short-rage interacting systems such as a cup of water, the entropy is always globally concave. However, in long-rage interacting systems such as geophysical fluids and self-gravitating systems, the entropy may be not globally concave, which leads to several strange behaviors (e.g., Campa et al. 2014). For instance, such a system may have a *negative* heat capacity. In our case, a negative heat capacity is not observed, but an ensemble inequivalence occurs (Venaille and Bouchet 2009, 2011b), which is typical of long-rage interacting systems. More precisely, the canonical ensemble is not equivalent to the microcanonical one in the non-globally-concave area. The microcanonical ensemble has been always employed in our calculations.

[1]The expression of $E(\Gamma, b)$ is obtained in the following two steps: (i) The Lagrangian multiplier c is obtained by solving (C.6) with a given Γ; (ii) The obtained $c(\Gamma, b)$ is substituted into (C.7), which gives $E(\Gamma, b)$.

Acknowledgments

The author is most grateful to the supervisor, Prof. Hiroshi Niino, for his many helpful suggestions in writing the present thesis.

He deeply acknowledges the members of this dissertation committee, Profs. Hisashi Nakamura, Keiichi Ishioka, Keita Iga, and Tomoki Tozuka, for a lot of important advice and constructive suggestions.

Special thanks are given to Prof. Freddy Bouchet and Dr. Antoine Venaille for a lot of important advice and constructive discussions while author's stay at ENS de Lyon in France and after author's return to Japan.

He is deeply grateful to Prof. Kaoru Sato, Dr. Masashi Kohma, Mr. Arata Amemiya, and Mr. Soichiro Hirano for discussing how to analyze JRA-55 and to make figures. He is really thankful to Prof. Keiichi Ishioka and Dr. Izumi Saito for their comments on how to modify the model codes and run the model. He is grateful to Ms. Tamaki Suematsu for her advice on expressions in English. He is appreciative of several comments by Prof. Masahide Kimoto.

He greatly appreciates Mr. Yohei Onuki advising on the presentation of the present study and having a lot of theoretical and interesting discussions. He would like to express his gratitude to members and ex-members of the Atmospheric and Oceanic Science Group for their discussions and encouragement: Dr. Takashi Ijichi, Mr. Masahiro Nomoto, Dr. Chikara Tsuchiya, Dr. Takenari Kinoshita, Dr. Kunihiro Aoki, Mr. Yuya Ozawa, Mr. Ryosuke Yasui, Mr. Hirokazu Sugiyama, Mr. Shun Nakajima, Mr. Shun Ohishi, Mr. Ryosuke Shibuya, Mr. Yuuki

Hayashi, Mr. Yuichi Minamihara, Mr. Atsushi Yoshida, and Mr. Katsutoshi Fukuzawa.

He appreciates the great help of his family, especially his parents. They have supported him financially for a long time.

The present study was supported by Grant-in-Aid for Research Fellow (25·8466) of the JSPS and by the Leading Graduate School Program for Frontiers of Mathematical Sciences and Physics (FMSP). The GFD-DENNOU library was used to make most figures.

References

Andrews, D. G., J. R. Holton, and C. B. Leovy, 1987: *Middle Atmosphere Dynamics*. Academic Press, 489 pp.

Andrews, D. G., and M. E. McIntyre, 1976: Planetary waves in horizontal and vertical shear: Generalized Eliassen-Palm relation and mean zonal acceleration. *J. Atmos. Sci.*, **33**, 2031–2048, doi:10.1175/1520-0469(1976)033⟨2031:PWIHAV⟩2.0.CO;2.

Andrews, D. G., and M. E. McIntyre, 1978: Generalized Eliassen-Palm and Charney-Drazin theorems for waves on axisymmetric mean flows in compressible atmospheres. *J. Atmos. Sci.*, **35**, 175–185, doi:10.1175/1520-0469(1978)035⟨0175:GEPACD⟩2.0.CO;2.

Arnold, V., 1965: Conditions for nonlinear stability of stationary plane curvilinear flows of an ideal fluid. *Dokl. Mat. Nauk*, **162**, 975–978.

Baldwin, M. P., and T. J. Dunkerton, 2001: Stratospheric harbingers of anomalous weather regimes. *Science*, **294**, 581–584, doi:10.1126/science.1063315.

Birner, T., and P. D. Williams, 2008: Sudden stratospheric warmings as noise-induced transitions. *J. Atmos. Sci.*, **65**, 3337–3343, doi:10.1175/2008JAS2770.1.

Black, R. X., and B. A. McDaniel, 2007: The dynamics of Northern Hemisphere stratospheric final warming events. *J. Atmos. Sci.*, **64**, 2932–2946, doi:10.1175/JAS3981.1.

Boucher, C., R. S. Ellis, and B. Turkington, 2000: Derivation of maximum entropy principles

in two-dimensional turbulence via large deviations. *J. Stat. Phys.*, **98**, 1235–1278, doi:10.1023/A:1018671813486.

Bouchet, F., 2008: Simpler variational problems for statistical equilibria of the 2D Euler equation and other systems with long range interactions. *Physica D*, **237**, 1976–1981, doi:10.1016/j.physd.2008.02.029.

Bouchet, F., T. Grafke, T. Tangarife, and E. Vanden-Eijnden, 2016: Large deviations in fast–slow systems. *J. Stat. Phys.*, **162**, 793–812, doi:10.1007/s10955-016-1449-4.

Bouchet, F., J. Laurie, and O. Zaboronski, 2014: Langevin dynamics, large deviations and instantons for the quasi-geostrophic model and two-dimensional Euler equations. *J. Stat. Phys.*, **156**, 1066–1092, doi:10.1007/s10955-014-1052-5.

Bouchet, F., and J. Sommeria, 2002: Emergence of intense jets and Jupiter's great red spot as maximum-entropy structures. *J. Fluid Mech.*, **464**, 165–207, doi:10.1017/S0022112002008789.

Bouchet, F., and A. Venaille, 2012: Statistical mechanics of two-dimensional and geophysical flows. *Phys. Rep.*, **515**, 227–295, doi:10.1016/j.physrep.2012.02.001.

Bretherton, F., and D. Haidvogel, 1976: Two-dimensional turbulence above topography. *J. Fluid Mech.*, **78**, 129–154, doi:10.1017/S002211207600236X.

Butler, A. H., D. J. Seidel, S. C. Hardiman, N. Butchart, T. Birner, and A. Match, 2015: Defining sudden stratospheric warmings. *Bull. Amer. Meteor. Soc.*, **96**, 1913–1928, doi:10.1175/BAMS-D-13-00173.1.

Campa, A., T. Dauxois, D. Fanelli, and S. Ruffo, 2014: *Physics of Long-Range Interacting Systems*. Oxford University Press, 410 pp.

Carnevale, G., and J. Frederiksen, 1987: Nonlinear stability and statistical mechanics of flow over topography. *J. Fluid Mech.*, **175**, 157–181, doi:10.1017/S002211208700034X.

Chao, W. C., 1985: Sudden stratospheric warmings as catastrophes. *J. Atmos. Sci.*, **42**, 1631–1646, doi:10.1175/1520-0469(1985)042⟨1631:SSWAC⟩2.0.CO;2.

Charlton, A. J., and L. M. Polvani, 2007: A new look at stratospheric sudden warmings. part I: Climatology and modelling benchmarks. *J. Climate*, **20**, 449–469, doi:10.1175/JCLI3996.1.

Chavanis, P. H., and J. Sommeria, 1996: Classification of self-organized vortices in two-dimensional turbulence: the case of a bounded domain. *J. Fluid Mech.*, **314**, 267–297, doi:10.1017/S0022112096000316.

Christiansen, B., 2000: Chaos, quasiperiodicity, and interannual variability: Studies of a stratospheric vacillation model. *J. Atmos. Sci.*, **57**, 3161–3173, doi:10.1175/1520-0469(2000)057⟨3161:CQAIVS⟩2.0.CO;2.

Dijkstra, H. A., 2013: *Nonlinear Climate Dynamics*. Cambridge University Press, 367 pp.

Dritschel, D. G., 1985: The stability and energetics of corotating uniform vortices. *J. Fluid Mech.*, **157**, 95–134, doi:10.1017/S0022112085002324.

Dritschel, D. G., 1986: The nonlinear evolution of rotating configurations of uniform vorticity. *J. Fluid Mech.*, **172**, 157–182, doi:10.1017/S0022112086001696.

Edmon, H. J., B. J. Hoskins, and M. E. McIntyre, 1980: Eliassen-Palm cross-sections for the troposphere. *J. Atmos. Sci.*, **37**, 2600–2616, doi:10.1175/1520-0469(1980)037⟨2600:EPCSFT⟩2.0.CO;2.

Ellis, R. S., K. Haven, and B. Turkington, 2000: Large deviation principles and complete

equivalence and nonequivalence results for pure and mixed ensembles. *J. Stat. Phys.*, **101**, 999–1064, doi:10.1023/A:1026446225804.

Ellis, R. S., K. Haven, and B. Turkington, 2002: Nonequivalent statistical equilibrium ensembles and refined stability theorems for most probable flows. *Nonlinearity*, **15**, 239–255, doi:10.1088/0951-7715/15/2/302.

Esler, J. G., 2008: The turbulent equilibration of an unstable baroclinic jet. *J. Fluid Mech.*, **599**, 241–268, doi:10.1017/S0022112008000153.

Esler, J. G., and N. J. Matthewman, 2011: Stratospheric sudden warmings as self-tuning resonances. part II: Vortex displacement events. *J. Atmos. Sci.*, **68**, 2505–2523, doi:10.1175/JAS-D-11-08.1.

Esler, J. G., and R. K. Scott, 2005: Excitation of transient rossby waves on the stratospheric polar vortex and the barotropic sudden warming. *J. Atmos. Sci.*, **62**, 3661–3682, doi:10.1175/JAS3557.1.

Foias, C., and J. Saut, 1984: Asymptotic behavior, as $t \to \infty$ of solutions of Navier-Stokes equations and nonlinear spectral manifolds. *Indiana Univ. Math. J.*, **33**, 459–477, doi:10.1512/iumj.1984.33.33025.

Gardiner, C., 2009: *Stochastic Methods: A Handbook for the Natural and Social Sciences*. Springer, 447 pp.

Gelfand, I. M., and S. V. Fomin, 2000: *Calculus of Variations*. Dover Publications, 240 pp.

Guo, Y., C. Hallstrom, and D. Spirn, 2004: Dynamics near an unstable Kirchhoff ellipse. *Comm. Math. Phys.*, **245**, 297–354, doi:10.1007/s00220-003-1017-z.

Haynes, P., 2005: Stratospheric dynamics. *Annu. Rev. Fluid Mech.*, **37**, 263–293, doi:10.1146/annurev.fluid.37.061903.175710.

Holm, D. D., J. E. Marsden, T. Ratiu, and A. J. Weinstein, 1985: Nonlinear stability of fluid and plasma equilibria. *Phys. Rep.*, **123**, 1–116, doi:10.1016/0370-1573(85)90028-6.

Holton, J. R., and C. Mass, 1976: Stratospheric vacillation cycles. *J. Atmos. Sci.*, **33**, 2218–2225, doi:10.1175/1520-0469(1976)033⟨2218:SVC⟩2.0.CO;2.

Ishioka, K., 2013: ispack-1.0.2. GFD Dennou Club, URL http://www.gfd-dennou.org/arch/ispack/index.htm.en.

Kidston, J., A. A. Scaife, S. C. Hardiman, D. M. Mitchell, N. Butchart, M. P. Baldwin, and L. J. Gray, 2015: Stratospheric influence on tropospheric jet streams, storm tracks and surface weather. *Nature Geosci.*, **8**, 433–440, doi:10.1038/NGEO2424.

Kobayashi, S., and Coauthors, 2015: The JRA-55 Reanalysis: General specifications and basic characteristics. *J. Meteor. Soc. Japan*, **93**, 5–48, doi:10.2151/jmsj.2015-001.

Kraichnan, R. H., and D. Montgomery, 1980: Two-dimensional turbulence. *Rep. Prog. Phys.*, **43**, 547–619, doi:10.1088/0034-4885/43/5/001.

Kubo, R., M. Today, and N. Hashitsume, 1998: *Statistical Physics II: Nonequilibrium Statistical Mechanics*. Springer, 300 pp.

Lait, L. R., 1994: An alternative for potential vorticity. *J. Atmos. Sci.*, **51**, 1754–1759, doi:10.1175/1520-0469(1994)051⟨1754:AAFFPV⟩2.0.CO;2.

Laurie, J., and F. Bouchet, 2015: Computation of rare transitions in the barotropic quasi-geostrophic equations. *New J. Phys.*, **17**, 015 009, doi:10.1088/1367-2630/17/1/015009.

Liberato, M. L. R., J. M. Castanheira, L. de la Torre, C. C. DaCamara, and L. Gimeno, 2007: Wave energy associated with the variability of the stratospheric polar vortex. *J. Atmos. Sci.*, **64**, 2683–2694., doi:10.1175/JAS3978.1.

Limpasuvan, V., D. W. J. Thompson, and D. L. Hartmann, 2004: The life cycle of the Northern Hemisphere sudden stratospheric warmings. *J. Climate*, **17**, 2584–2596, doi:10.1175/1520-0442(2004)017⟨2584:TLCOTN⟩2.0.CO;2.

Liu, Y. S., and R. K. Scott, 2015: The onset of the barotropic sudden warming in a global model. *Quart. J. Roy. Meteor. Soc.*, doi:10.1002/qj.2580.

Love, A. E. H., 1893: On the stability of certain vortex motions. *Proc. London Math. Soc.*, **25**, 18–43, doi:10.1112/plms/s1-25.1.18.

Majda, A., S. Shim, and X. Wang, 2000: Selective decay for geophysical flows. *Meth. Appl. Anal.*, **7**, 511–554, doi:10.4310/MAA.2000.v7.n3.a8.

Majda, A., and X. Wang, 2006: *Nonlinear Dynamics and Statistical Theories for Basic Geophysical Flows*. Cambridge University Press, 564 pp.

Matsuno, T., 1970: Vertical propagation of stationary planetary waves in the winter Northern Hemisphere. *J. Atmos. Sci.*, **27**, 871–883, doi:10.1175/1520-0469(1970)027⟨0871:VPOSPW⟩2.0.CO;2.

Matsuno, T., 1971: A dynamical model of the stratospheric sudden warming. *J. Atmos. Sci.*, **28**, 1479–1494, doi:10.1175/1520-0469(1971)028⟨1479:ADMOTS⟩2.0.CO;2.

Matthewman, N. J., A. J. Charlton, and L. M. Polvani, 2009: A new look at stratospheric sudden warmings. Part III: Polar vortex evolution and vertical structure. *J. Climate*, **22**, 1566–1585, doi:10.1175/2008JCLI2365.1.

Matthewman, N. J., and J. G. Esler, 2011: Stratospheric sudden warmings as self-tuning resonances. part I: Vortex splitting events. *J. Atmos. Sci.*, **68**, 2481–2504, doi:10.1175/JAS-D-11-07.1.

McIntyre, M. E., 1982: How well do we understand the dynamics of stratospheric warmings? *J. Meteor. Soc. Japan*, **60**, 37–65.

McIntyre, M. E., and T. N. Palmer, 1983: Breaking planetary waves in the stratosphere. *Nature*, **305**, 593–600, doi:10.1038/305593a0.

McIntyre, M. E., and T. N. Palmer, 1984: The "surf zone" in the stratosphere. *J. Atmos. Terr. Phys.*, **46**, 825–849, doi:10.1016/0021-9169(84)90063-1.

Merryfield, W. J., 1998: Effects of stratification on quasi-geostrophic inviscid equilibria. *J. Fluid Mech.*, **354**, 345–356, doi:10.1017/S0022112097007684.

Michel, J., and R. Robert, 1994: Large deviations for Young measures and statistical mechanics of infinite-dimensional dynamical systems with conservation law. *Comm. Math. Phys.*, **159**, 195–215, doi:10.1007/BF02100491.

Miller, J., 1990: Statistical mechanics of Euler equations in two dimensions. *Phys. Rev. Lett.*, **65**, 2137–2140, doi:10.1103/PhysRevLett.65.2137.

MirRokni, S. M., A. R. Mohebalhojeh, and D. G. Dritschel, 2011: Revisiting vacillations in shallow-water models of the stratosphere using potential-vorticity-based numerical algorithms. *J. Atmos. Sci.*, **68**, 1007–1022, doi:10.1175/2011JAS3622.1.

Mitchell, D. M., L. J. Gray, J. Anstey, M. P. Baldwin, and A. J. Charlton, 2013: The influence of stratospheric vortex displacements and splits on surface climate. *J. Climate*, **26**, 2668–2682, doi:10.1175/JCLI-D-12-00030.1.

Mitchell, T. B., and L. F. Rossi, 2008: The evolution of Kirchhoff elliptic vortices. *Phys. Fluids*, **20**, doi:10.1063/1.2912991.

Mukougawa, H., and T. Hirooka, 2004: Predictability of stratospheric sudden warming: A case study for 1998/99 winter. *Mon. Wea. Rev.*, **132**, 1764–1776, doi:10.1175/1520-0493(2004)132⟨1764:POSSWA⟩2.0.CO;2.

Nakagawa, K. I., and K. Yamazaki, 2006: What kind of stratospheric sudden warming propagates to the troposphere? *Geophys. Res. Lett.*, **33**, L04801, doi:10.1029/2005GL024784.

Naso, A., P. H. Chavanis, and B. Dubrulle, 2010: Statistical mechanics of two-dimensional Euler flows and minimum enstrophy states. *Eur. Phys. J. B*, **77**, 187–212, doi:10.1140/epjb/e2010-00269-0.

Newman, P. A., and J. E. Rosenfield, 1997: Stratospheric thermal damping times. *Geophys. Res. Lett.*, **24**, 433–436, doi:10.1029/96GL03720.

Onsager, L., 1949: Statistical hydrodynamics. *Nuovo Cimento*, **6**, 249–286.

Palmer, T. N., 1981: Diagnostic study of a wavenumber-2 stratospheric sudden warming in a transformed Eulerian mean formalism. *J. Atmos. Sci.*, **38**, 844–855, doi:10.1175/1520-0469(1981)038⟨0844:DSOAWS⟩2.0.CO;2.

Plumb, R. A., 1981a: Forced waves in a baroclinic shear flow. part 2: Damped and undamped response to weak near-resonant forcing. *J. Atmos. Sci.*, **38**, 1856–1869, doi:10.1175/1520-0469(1981)038⟨1856:FWIABS⟩2.0.CO;2.

Plumb, R. A., 1981b: Instability of the distorted polar night vortex: A theory of stratospheric warmings. *J. Atmos. Sci.*, **38**, 2514–2531, doi:10.1175/1520-0469(1981)038⟨2514:IOTDPN⟩2.0.CO;2.

Polvani, L. M., and D. W. Waugh, 2004: Upward wave activity flux as a precursor to extreme stratospheric events and subsequent anomalous surface weather regimes. *J. Climate*, **17**, 3548–3554, doi:10.1175/1520-0442(2004)017⟨3548:UWAFAA⟩2.0.CO;2.

Polvani, L. M., D. W. Waugh, and R. A. Plumb, 1995: On the subtropical edge of the stratospheric surf zone. *J. Atmos. Sci.*, **52**, 1288–1309, doi:10.1175/1520-0469(1995)052⟨1288:OTSEOT⟩2.0.CO;2.

Prieto, R., J. P. Kossin, and W. H. Schubert, 2001: Symmetrization of lopsided vorticity monopoles and offset hurricane eyes. *Quart. J. Roy. Meteor. Soc.*, **127**, 2307–2327, doi:10.1002/qj.49712757706.

Prieto, R., and W. H. Schubert, 2001: Analytical predictions for zonally symmetric equilibrium states of the stratospheric polar vortex. *J. Atmos. Sci.*, **58**, 2709–2728, doi:10.1175/1520-0469(2001)058⟨2709:APFZSE⟩2.0.CO;2.

Robert, R., 1991: A maximum-entropy principle for two-dimensional perfect fluid dynamics. *J. Stat. Phys.*, **65**, 531–553, doi:10.1007/BF01053743.

Robert, R., and J. Sommeria, 1991: Statistical equilibrium states for two-dimensional flows. *J. Fluid Mech.*, **229**, 291–310, doi:10.1017/S0022112091003038.

Rong, P.-P., and D. W. Waugh, 2004: Vacillations in a shallow-water model of the stratosphere. *J. Atmos. Sci.*, **61**, 1174–1185, doi:10.1175/1520-0469(2004)061⟨1174:VIASMO⟩2.0.CO;2.

Roscoe, H. K., J. D. Shanklin, and S. R. Colwell, 2005: Has the Antarctic vortex split before 2002? *J. Atmos. Sci.*, **62**, 581–588, doi:10.1175/JAS-3331.1.

Ruzmaikin, A., J. Lawrence, and C. Cadavid, 2003: A simple model of stratospheric dynamics including solar variability. *J. Climate*, **16**, 1593–1600, doi:10.1175/1520-0442-16.10.1593.

Salmon, R., 1998: *Lectures on Geophysical Fluid Dynamics*. Oxford University Press, 378 pp.

Salmon, R., G. Holloway, and M. Hendershott, 1976: The equilibrium statistical mechanics of simple quasi-geostrophic models. *J. Fluid Mech.*, **75**, 691–703, doi:10.1017/S0022112076000463.

Scott, R. K., 2016: A new class of vacillations of the stratospheric polar vortex. *Quart. J. Roy. Meteor. Soc.*, **142**, 1948–1957, doi:10.1002/qj.2788.

Scott, R. K., and L. M. Polvani, 2006: Internal variability of the winter stratosphere. part I: Time-independent forcing. *J. Atmos. Sci.*, **63**, 2758–2776, doi:10.1175/JAS3797.1.

Sekimoto, K., 2010: *Stochastic Energetics*. Springer, 300 pp.

Seviour, W. J. M., D. M. Mitchell, and L. J. Gray, 2013: A practical method to identify displaced and split stratospheric polar vortex events. *Geophys. Res. Lett.*, **40**, 5268–5273, doi:10.1002/grl.50927.

Seydel, R., 2009: *Practical Bifurcation and Stability Analysis*. Springer, 477 pp.

Sjoberg, J. P., and T. Birner, 2012: Transient tropospheric forcing of sudden stratospheric warmings. *J. Atmos. Sci.*, **69**, 3420–3432, doi:10.1175/JAS-D-11-0195.1.

Sjoberg, J. P., and T. Birner, 2014: Stratospheric wave-mean flow feedbacks and sudden stratospheric warmings in a simple model forced by upward wave activity flux. *J. Atmos. Sci.*, **71**, 4055–471, doi:10.1175/JAS-D-14-0113.1.

Swaters, G. E., 1999: *Introduction to Hamiltonian Fluid Dynamics and Stability Theory*. CRC Press, 288 pp.

Tang, Y., 1987: Nonlinear stability of vortex patches. *Trans. Amer. Math. Soc.*, **304**, 617–638, doi:10.1090/S0002-9947-1987-0911087-X.

Touchette, H., 2009: The large deviation approach to statistical mechanics. *Phys. Rep.*, **478**, 1–69, doi:10.1016/j.physrep.2009.05.002.

Tripathi, O. P., and Coauthors, 2015: The predictability of the extratropical stratosphere on monthly time-scales and its impact on the skill of tropospheric forecasts. *Quart. J. Roy. Meteor. Soc.*, **141**, 987–1003, doi:10.1002/qj.2432.

Tung, K. K., and R. S. Lindzen, 1979a: A theory of stationary long waves. part I: A simple theory of blocking. *Mon. Wea. Rev.*, **107**, 714–734, doi:10.1175/1520-0493(1979)107⟨0714:ATOSLW⟩2.0.CO;2.

Tung, K. K., and R. S. Lindzen, 1979b: A theory of stationary long waves. part II: Resonant rossby waves in the presence of realistic vertical shears. *Mon. Wea. Rev.*, **107**, 735–750, doi:10.1175/1520-0493(1979)107⟨0735:ATOSLW⟩2.0.CO;2.

Vallis, G. K., 2006: *Atmospheric and Oceanic Fluid Dynamics: Fundamentals and Large-Scale Circulation*. Cambridge University Press, 745 pp.

Venaille, A., 2012: Bottom-trapped currents as statistical equilibrium states above topographic anomalies. *J. Fluid Mech.*, **699**, 500–510, doi:10.1017/jfm.2012.146.

Venaille, A., and F. Bouchet, 2009: Statistical ensemble inequivalence and bicritical points for two-dimensional flows and geophysical flows. *Phys. Rev. Lett.*, **102**, 104 501, doi:10.1103/PhysRevLett.102.104501.

Venaille, A., and F. Bouchet, 2011a: Ocean rings and jets as statistical equilibrium states. *J. Phys. Oceanogr.*, **10**, 1860–1873, doi:10.1175/2011JPO4583.1.

Venaille, A., and F. Bouchet, 2011b: Solvable phase diagrams and ensemble inequivalence for

two-dimensional and geophysical turbulent flows. *J. Stat. Phys.*, **143**, 346–380, doi:10.1007/s10955-011-0168-0.

Wan, Y. H., 1986: The stability of rotating vortex patches. *Comm. Math. Phys.*, **107**, 1–20, doi:10.1007/BF01206950.

Waugh, D. N. W., 1997: Elliptical diagnostics of stratospheric polar vortices. *Quart. J. Roy. Meteor. Soc.*, **123**, 1725–1748, doi:10.1002/qj.49712354213.

Waugh, D. W., and L. M. Polvani, 2013: *Stratospheric Polar Vortices*, 43–57. American Geophysical Union, doi:10.1002/9781118666630.ch3.

Waugh, D. W., and W. J. Randel, 1999: Climatology of Arctic and Antarctic polar vortices using elliptical diagnostics. *J. Atmos. Sci.*, **56**, 1594–1613, doi:10.1175/1520-0469(1999)056⟨1594:COAAAP⟩2.0.CO;2.

Yoden, S., 1987: Bifurcation properties of a stratospheric vacillation model. *J. Atmos. Sci.*, **44**, 1723–1733, doi:10.1175/1520-0469(1987)044⟨1723:BPOASV⟩2.0.CO;2.